Abstract

Craft, Michael Jacob. Design Optimization of MagneShock™ Magnetorheological Shock Absorbers and Development of Fuzzy Logic Control Algorithms for Semi-Active Vehicle Suspensions. (Under the direction of Dr. Gregory D. Buckner)

Automotive ride quality and handling performance remain challenging design tradeoffs for modern, passive automobile suspension systems. Despite extensive published research outlining the benefits of active vehicle suspensions in addressing this tradeoff, the cost and complexity of these systems prohibit widespread commercial adoption. Semi-active suspensions offer reduced performance benefits over passive suspensions without the cost and complexity associated with fully active systems. This paper outlines the benefits of implementing real-time, fuzzy logic control (FLC) to a vehicle suspension equipped with commercially available magnetorheological (MR) shock absorbers, Carrera MagneShocks™.

MagneShocks™ utilize controllable electromagnets to change the MR fluid viscosity and vary the damping characteristics of the shock. The application of FLC to these components, based on the expertise of experienced engineers from the racing industry, was first tested and refined in simulation, then applied experimentally, resulting in the significant improvement of vehicle performance. Results include 25% reductions in sprung-mass absorbed power (U.S. Army 6 Watt Absorbed Power Criterion) as compared with typical original equipment (OE) shock absorbers over urban terrains in both simulation and experimentation. RMS sprung-mass accelerations were also reduced by as much as 9%, but usually with an increase in total suspension travel over the passive systems. Nominal degradations in RMS tire normal forces were documented through computer simulations. When compared to fixed-current MagneShocks™, FLC resulted in 2-9% reductions in RMS sprung-mass accelerations and comparable absorbed powers. Possible means for improving the performance of this semi-active suspension include reducing the suspension spring stiffness and increasing the dynamic damping range of the MagneShock™.

Design Optimization of MagneShock™ Magnetorheological Shock Absorbers and Development of Fuzzy Logic Control Algorithms for Semi-Active Vehicle Suspensions

by

MICHAEL JACOB CRAFT

A thesis submitted to the Graduate Faculty of
North Carolina State University
in partial fulfillment of the
requirements for the Degree of
Master of Science

MECHANICAL AND AEROSPACE ENGINEERING

Raleigh

March 25, 2003

APPROVED BY:

_____

_____

_____

Chairman of Advisory Committee

Dedication

I dedicate this work to my family and friends. Without their constant support, none of this would have been possible.

Biography

A native of North Carolina, some of Michael Craft's early interests included those related to automobiles, which lead him to the study of mechanical engineering. In May 2001, he graduated from North Carolina State University with a Bachelor of Science degree in Mechanical Engineering and a minor in Materials Science Engineering. While an undergraduate, Michael served as an engineering co-op with GKN Automotive, Inc. and was very active in the Society of Automotive Engineers (SAE) collegiate design competitions. After graduating, Michael stayed on at NCSU to pursue his Master of Science degree in Mechanical Engineering under the direction of Dr. Greg Buckner. His graduate work focused on the design and implementation of semi-active suspension control systems for automobiles. Michael plans to pursue a career in the field of mechanical engineering as applied to the field of magnetorheological-based control systems.

Acknowledgements

This work was supported by Carrera Shocks Inc, of Atlanta, Georgia. I would like to thank Dick Anderson for his help and enthusiasm over the course of this research, as none of this would have been possible without him. I would also like to thank Mike Lutz, Jim Larson, and all the employees at Carrera for their help with this ongoing development.

Table of Contents

List of Tables

List of Figures

1. Introduction

Automotive vehicle performance has been a major focus of industrial research and development for nearly a century. While vehicle performance can be quantified in many ways, ride quality and handling are two aspects of performance directly related to the vehicle suspension system. Generally speaking, vehicles exhibiting good ride quality are characterized by suspensions with low spring rates, low damping rates, resulting in large suspension travel. Vehicles exhibiting good handling generally incorporate suspensions with high spring and damping rates, resulting in small suspension deflections [50]. While the refinement of passive suspension systems [28] for modern automobiles has resulted in acceptable levels of both handling and ride quality under common road conditions, these systems are not typically optimized for any particular type of terrain. Passive suspension performance characteristics still represent a major compromise between ride quality, handling, suspension travel, and controlling body motion.

Research focused on reducing this vehicle performance tradeoff has lead to the development of active suspension systems. Active control is achieved through the application of control forces (compressive and tensile) usually applied between the sprung and unsprung masses of each wheel assembly. These forces can be supplied by a number of hydraulic or electromechanical actuators and motors. While active control schemes cannot simultaneously maximize the performance benefits in each of the suspension performance categories (ride quality, road holding, body motion, and suspension travel requirements), it does provide the best possible means for improving overall vehicle performance [12,16,17,18,19,22,26,51,38,45,50,52].

Control systems for active suspensions have been the focus of extensive research since Karnopp et al. first proposed the "skyhook damping" approach in the early 1970s [27]. While

theoretically important, "skyhook" damping can only be mimicked in practical applications, leading to a variety of alternate control strategies developed to achieve similar results [2,3,6,16,18,19,22,14,27,51,38,45,50]. These algorithms frequently exhibit significant improvements in vehicle ride quality (often quantified in terms of the RMS sprung-mass acceleration) and handling performance (often quantified as reduced fluctuations in tire-road contact forces). Although "skyhook" damping considers only the vertical (bump) vehicle response, additional rigid body responses (pitch and roll) and suspension travel requirements have been studied in significant detail [6,49]. Modern control approaches, including linear quadratic regulators [2,22,45,51] and pole placement algorithms [18], along with intelligent control techniques [6] have been extensively researched for active suspension applications.

Despite the abundance of simulated results indicating the potential benefits of active control systems [16,18,19,21,26,43,50,51,52], few researchers have implemented and experimentally validated these benefits [6,12,17,21,38,47]. Buckner et al. [6] demonstrated effective control of an electromechanical suspension system for an off-road vehicle, a military HMMWV. Venhovens et al. demonstrated significant improvements in roll control [47]. Many authors have pointed out the inherent disadvantages of these active systems [12,17,18,21,43,47,48,51,50], which frequently relate to increased costs and complexity. Hellebrecht et al. discovered that the cost requirements for active suspension systems far outweighed the performance benefits [21]. Similarly, Goran et al. at Ford Motor Company demonstrated a prototype active suspension vehicle on the Thunderbird in the early nineties, but the cost and complexity of the system far exceeded the performance gains [17].

As early as 1974, Karnopp [27] realized the potential disadvantages associated with active control implementations: cost, complexity, power consumption, and response time [6,16,20]. For this reason, he began research on a semi-active damper in which the damping force was

controllable. While semi-active control cannot offer the full benefits of active control [16,21,50], it does offer substantially better performance than passive systems.

The advantages of semi-active suspensions were first demonstrated by Karnopp et al. in conjunction with Lord Corporation in 1974, as he attempted to emulate his "skyhook" damping approach using a hydraulically adjustable damper [27]. Since that time, he and numerous other authors [7,14,24,43,47,51,52] have focused on the development of practical semi-active suspensions and control algorithms. Miller [38], Gillespie [16], and Barak [2] each published findings on the tuning of passive, semi-active, and active suspensions, and all authors clearly show the practical advantages of semi-active systems.

Many early semi-active control techniques were based on two-state or multi-state damper settings [20,27,28,39,43]. Because of their inherent simplicity, these discrete-state control schemes were readily implemented by researchers who demonstrated significant improvements in ride quality [20,28,39]. Later on, semi-active dampers incorporated mechanical valving mechanisms to alter damping characteristics [7,14,27,28,39,43,50,51]. These systems were often bulky and required strict manufacturing tolerances to function effectively, and were expensive to manufacture and maintain. Nevertheless, these systems were commercially produced in limited numbers, but usually with only driver-selectable damping rates [12,17].

Recent developments in electro-rheological (ER) and magneto-rheological (MR) fluids have allowed for more feasible means of implementing semi-active vehicle control. The wide viscosity ranges associated with ER and MR fluids, combined with their high bandwidths, make them excellent choices for use in semi-active devices [10,36,37,50]. However, because ER fluids require high control voltages, cannot produce high shear forces, and are susceptible to contaminants [25], they are not ideally suited for automotive applications. MR fluids

produce large shear forces in the presence of magnetic fields (Figure 1). MR fluids also require lower excitation power and are easily adopted for use in automotive components. Typically, embedded electromagnets offer a simple means to alter the magnetic field in these damping devices [9,34]. And because MR dampers have no moving parts inside the shock [8,9,25], they are simpler, cheaper, and more durable than other types of semi-active devices and their passive counterparts.

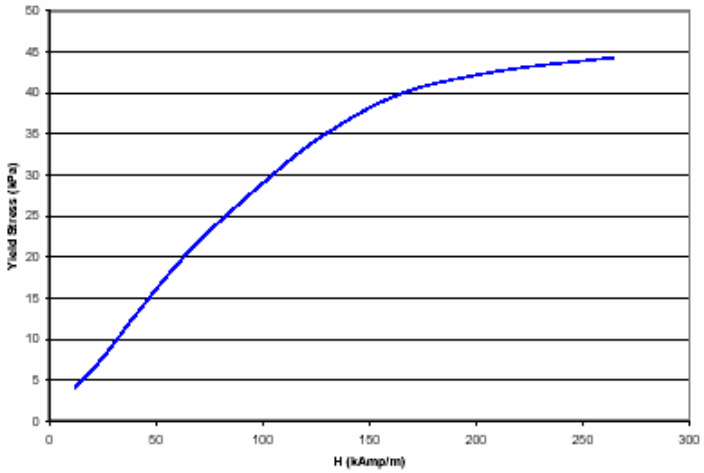

Figure 1. Shear stress versus magnetic field excitation for a commercial MR fluid (Lord MRF 132) [35]

Despite their many advantages, MR dampers require careful design optimization to operate effectively and efficiently [32,33,34]. Most MR dampers utilize internal electromagnets in which coil currents are varied to achieve the desired magnetic field. The magnetic flux follows a path created by the ferromagnetic materials within the shock, and typically passes through the MR fluid only in the region of greatest hydraulic restriction (usually an annular gap). In order to maximize the efficiency of the shock and produce the most damping (maximize the MR fluid shear stress), the shock should be designed so that none of the ferromagnetic components reach magnetic saturation, which dramatically limits damper performance and efficiency. Magnetic circuit analysis and finite element analysis can be used to predict the behavior of damper components and make necessary design changes.

Control schemes for semi-active suspensions, like their active counterparts, are frequently based on the "skyhook" damping approach [27]. Despite the large number of publications related to control of semi-active suspensions, most do not account for the nonlinear characteristics of vehicle suspensions and MR fluid dynamics. Techniques that do address nonlinearities include sliding mode control [13,43] and the application of neural networks [6,43]. However, these approaches typically require more accurate system modeling and development time than is suitable for commercial adoption. For these reasons, the application of fuzzy logic control (FLC) has become very popular for semi-active suspensions, as it is very intuitive for the user, easily implemented, and can account for system nonlinearities [1,24,39,40,43].

This paper outlines the benefits of implementing real-time, fuzzy logic control (FLC) to a vehicle suspension equipped with commercial magneto-rheological (MR) shock absorbers (Carrera MagneShocks™). The MagneShock's™ electromagnetic characteristics were first modeled, analyzed, and subsequently redesigned for improved efficiency. The development of a fuzzy logic control algorithm was based on the expertise of a design engineer with 30 years of experience in the racing shock industry. Following extensive computer simulations, this semi-active suspension system was implemented on an instrumented vehicle for road testing and performance evaluations. Computer and experimental test results reveal significant improvements in ride quality and handling performance.

2. Magnetic Field Modeling and Component Optimization Using Ansoft Maxwell 3D Software

Carrera introduced a "first-generation" MagneShock™ for commercial sale in 2000 as a manually adjustable automotive shock absorber for racing applications (Figure 2). While this shock offered a broad, adjustable range of damping force for given suspension velocities (Figure 3), magnetic saturation occurred at relatively low coil current levels, limiting efficiency and performance.

Figure 2. Carrera's 1st Generation MagneShock™ Shown with Control Box

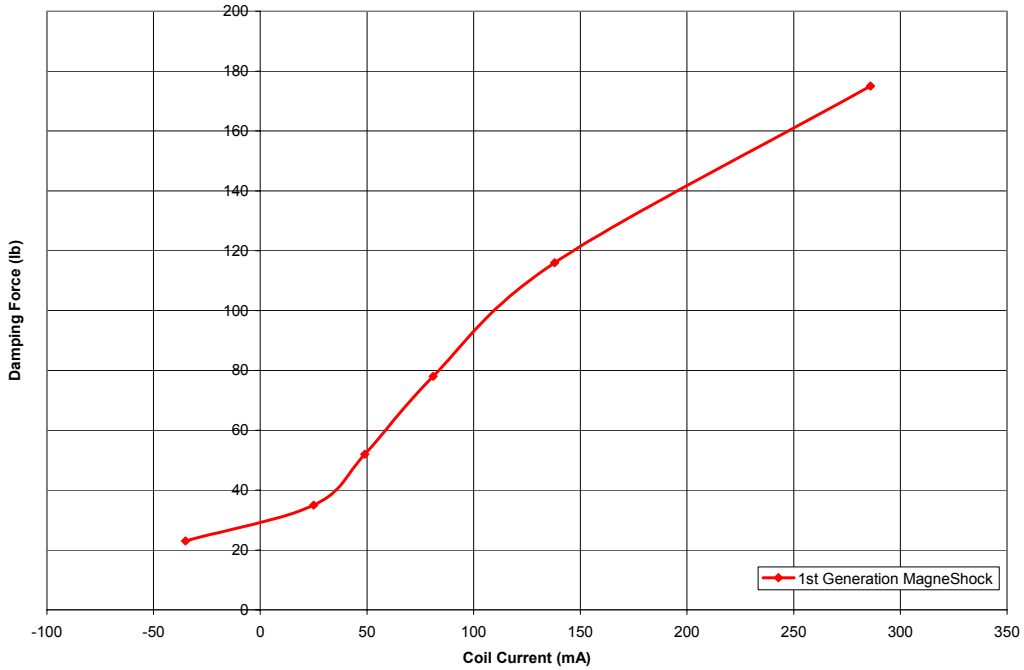

Figure 3. First Generation MagneShock™ damping force at 1 in/s velocity

This first-generation MagneShock™ incorporated off-the-shelf components used in a similar product, Lord Corporation's Motion Master™ truck seat shock absorber. The Motion Master™ was designed to control vertical seat vibrations in truck cabs. The Motion Master™ contains an electromagnet coil winding which was acquired by Carrera for MagneShock™ prototypes. To reduce power requirements, the Motion Master™ 12 ohm coil was rewound with a smaller diameter wire, resulting in a 27 ohm, 525 turn coil (Figure 5). The overall dimensions of this coil remained unchanged, making it slightly undersized for use in a semi-active vehicle shock absorber. For this reason, the original MagneShock™ suffered from magnetic saturation [5,47], greatly reducing its efficiency and performance capabilities.

Figure 4. Motion Master™ seat damping system from Lord Corporation

Figure 5. Electromagnet coil used in both MagneShock™ and Motion Master™

To eliminate magnetic saturation in this first-generation MagneShock™, extensive electromagnetic design optimizations were conducted. Three-dimensional finite element analysis (FEA) software was used to correlate electromagnetic characteristics to experimental damping measurements and indicate design changes that would increase efficiency and performance.

2.1. Background

Analysis of the Carrera MagneShock™ was performed using a three-dimensional FEA package for electromechanical systems, Maxwell 3D, from Ansoft Corporation. Like other FEA packages, Maxwell 3D reduces complex geometries into large numbers of small tetrahedral elements [11]. Electromechanical analysis is reduced to an energy balance on large numbers

of these elements. Magnetic and electric field data are computed at the element nodes, and results are interpolated over each element. By iteratively computing and comparing the energy balance to previous results, values of magnetic field intensity H and magnetic flux density B can be calculated for the entire assembly. However, if the energy balance fails to converge towards an acceptable value, then the tetrahedral mesh is refined (manually or automatically) and the process is repeated. This procedure continues until the percent error for the energy of the entire system falls below a user-specified value (2% for these analyses).

2.2. Electromagnetic Design Optimization

Although ferromagnetic materials (i.e. carbon steels) are excellent conductors of magnetic flux (have a low magnetic permeability), they become magnetically saturated at specific field intensities, dramatically limiting the magnetic flux densities in the device (Figure 6). One means of eliminating magnetic flux saturation is to increase the cross-sectional area of ferromagnetic materials in critical areas.

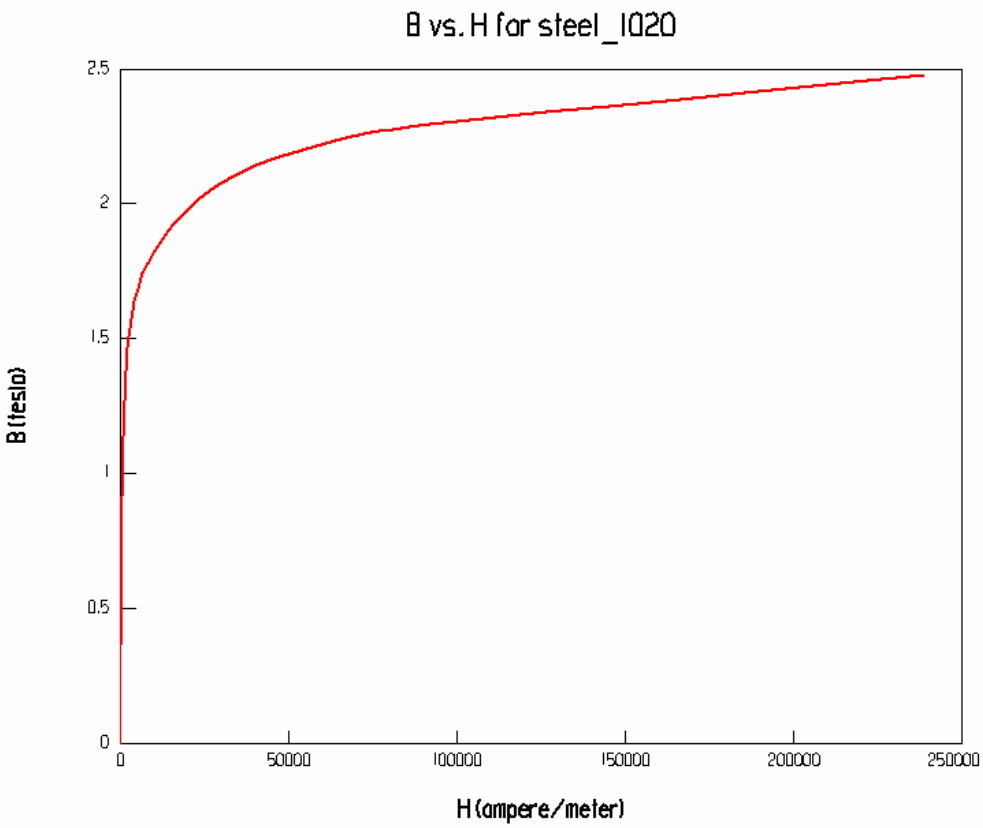

Figure 6. BH Magnetization curve for 1020 steel

The MagneShock™ piston assembly is machined from two pieces of 1020 steel (the piston and piston nut), one stainless steel rod (excluded in some of the analyses) and one electromagnet coil (Figure 8). All of these components are immersed in MR fluid during normal shock operation. The annular gap is where the magnetic field intensity H should be maximized for a given coil current (300 mA maximum for this device) [32,33,34] to maximize circuit efficiency. The use of FEA is critical to accurately predict magnetic fields and flux densities in MR devices, as it is difficult or impossible to make experimental measurements in MR fluid-immersed environments. Experimental measurements made in air-immersed environments may be several orders of magnitude in error, and may not accurately reflect the nonlinearities present in the MR fluid.

2.3. Component Modeling

For the initial simulation, the dimensions of the MagneShock™ components were specified in Maxwell 3D along with the material properties specified in Table 1.

Table 1. Magnetic Circuit Modeling Material Types

Component Material Types	
Electromagnet coil windings	Copper
Coil body	Epoxy
Piston nut, piston	1020 Steel
Rod	304 Stainless Steel
MR Fluid	Lord Corp. MRF132LD

Figure 7 shows the complete three-dimensional solid model used for FEA analysis. The coil (shown separately Figure 8) was specified to have a current of 300mA, which equates to a magnetic field excitation of 157.5 amp-turns (525 turns of wire in the coil). This model was validated by comparing the simulated flux density in the annular gap with those found experimentally (see Appendix 9.1). Subsequent changes made to optimize the components (piston, piston nut, and coil) were guided by manufacturing restrictions and simulation results.

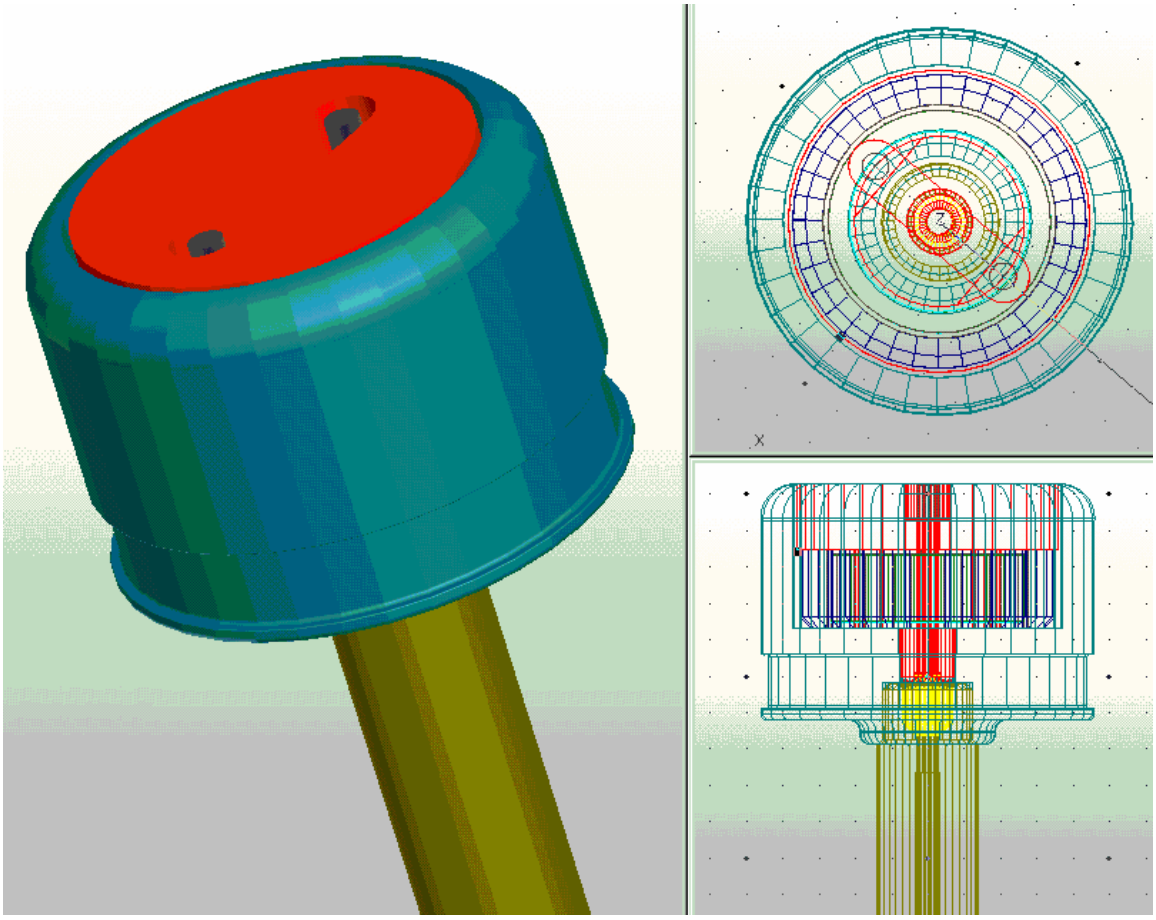

Figure 7. Three-dimensional solid model of the first-generation MagneShock™

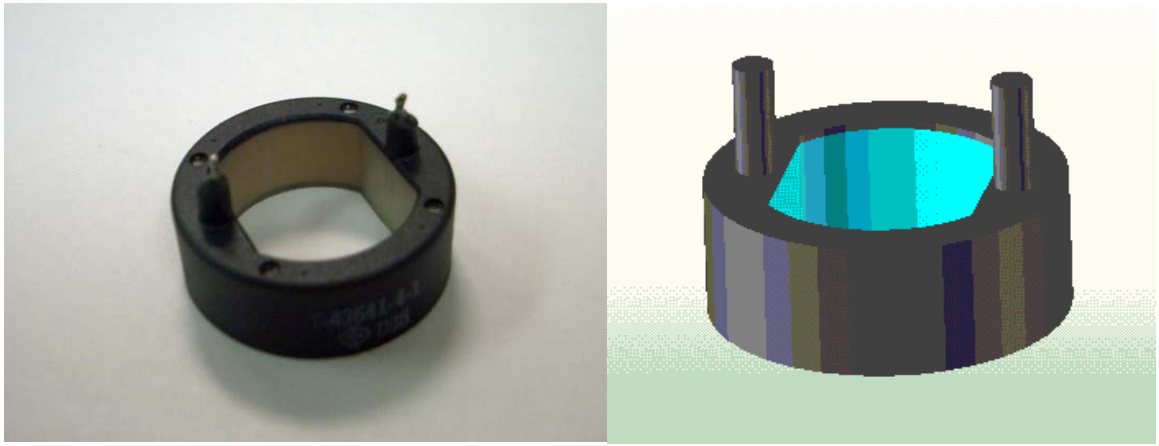

Figure 8. MagneShock™ electromagnet coil: three-dimensional solid model (right) and actual (left).

2.3.1. Element Meshing

The solid model components were meshed using Maxwell's default algorithm. The software iteratively refined the mesh until the energy balance error fell below 2%. Modeled components were simplified to reduce the computational demands of the overall problem, specifically complexities associated with component geometries. Fillets and component chamfers that were located in areas of low flux density were excluded from the component model.

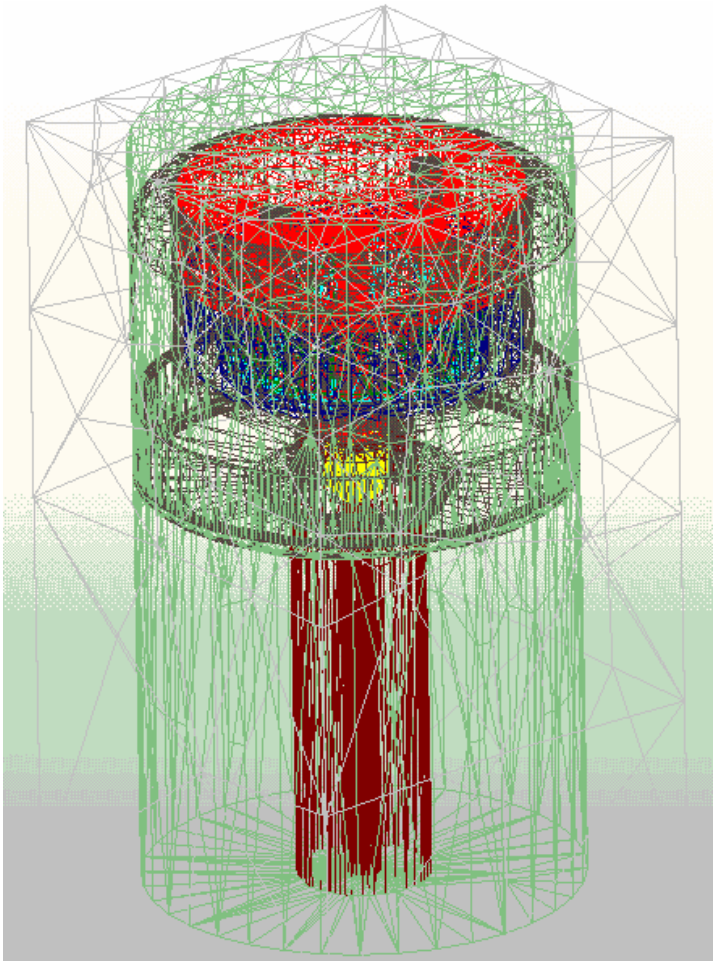

Figure 9. Meshed shock model

2.4. FEA Results

The results presented below were determined using post-processor features. Cross-sectional cuts were made at critical locations and the magnetic flux density (B) was estimated in the coil core (the center of the electromagnet) and the annular gap. Additionally, the magnetic field intensity (H) was determined in the annular gap and this value was related to the MR fluid shear stress (relates to damping) to determine the shock damping. Results obtained from the "first generation" MagneShock™ were used to optimize the "second generation" design for efficiency and performance.

2.4.1. First generation MagneShock™

As previously mentioned, the first-generation MR shock was developed completely using off-the-shelf components and without magnetic circuit analysis or the aid of FEA. As shown in the FEA results of Figure 10 and Figure 11, the annular gap (controlled damping region) has a very low magnetic flux density (0.36 T) due to saturation of the electromagnetic core (saturated well below a coil current of 300mA).

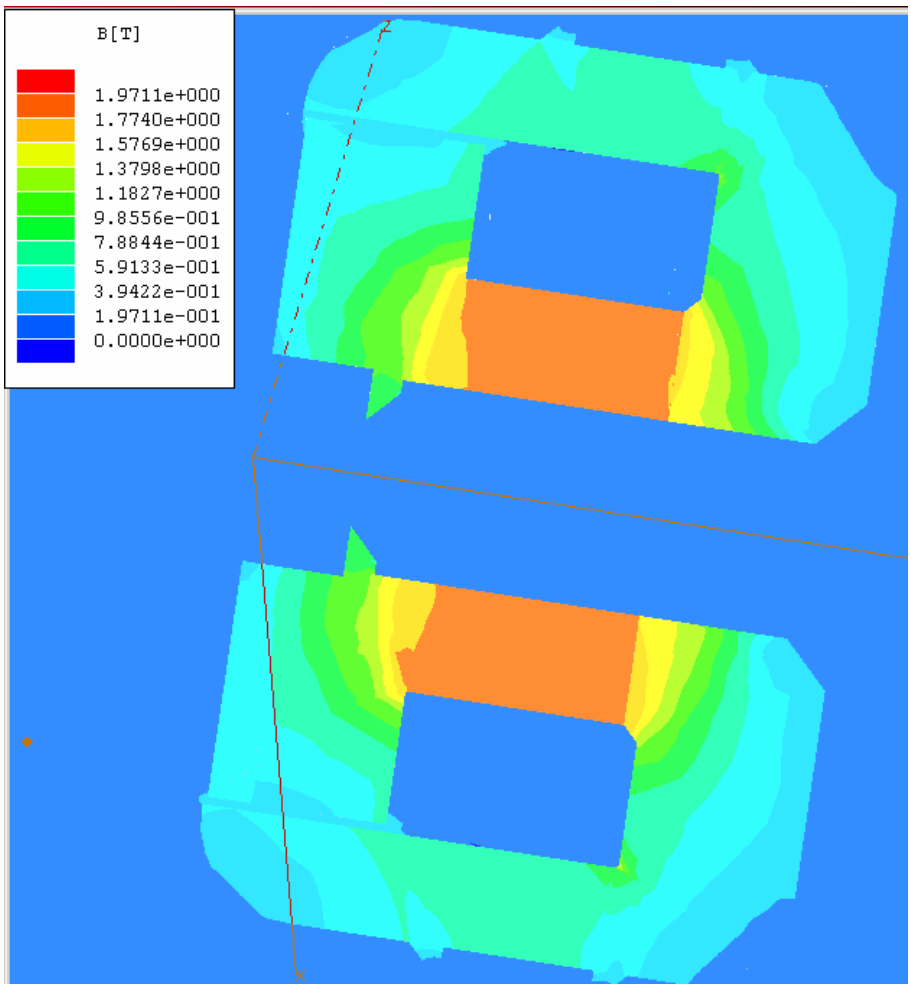

Figure 10. FEA results for first-generation MagneShock™: magnetic flux density

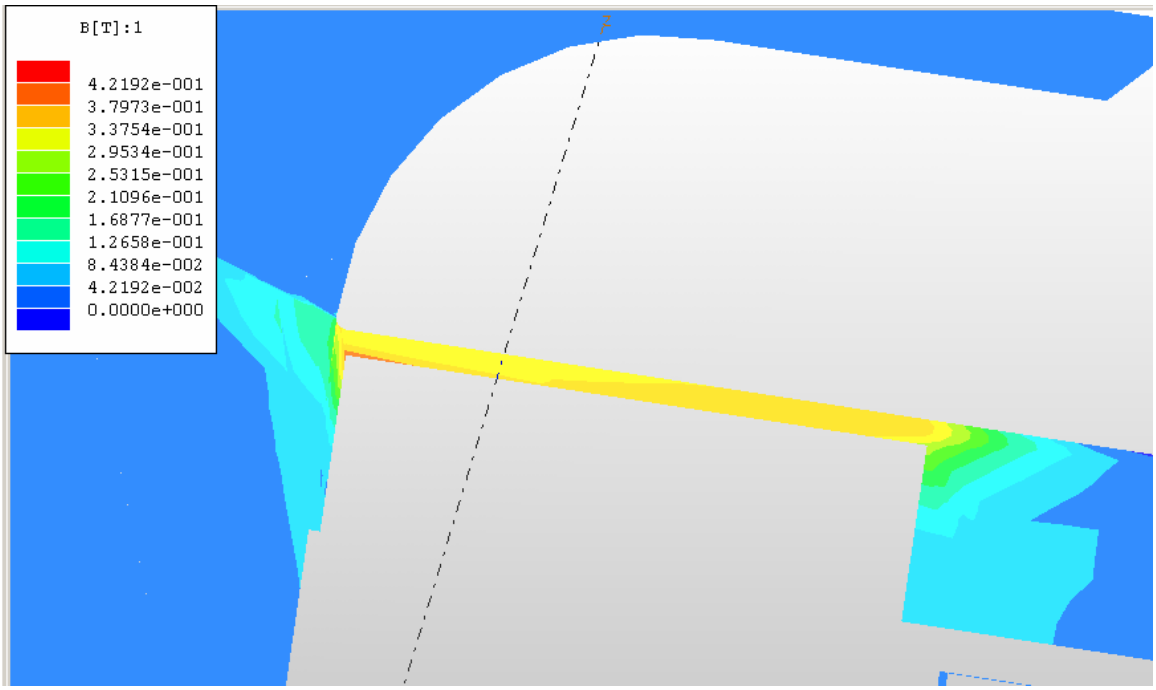

Figure 11. FEA results for first-generation MagneShock™: close-up showing magnetic flux density in annular gap

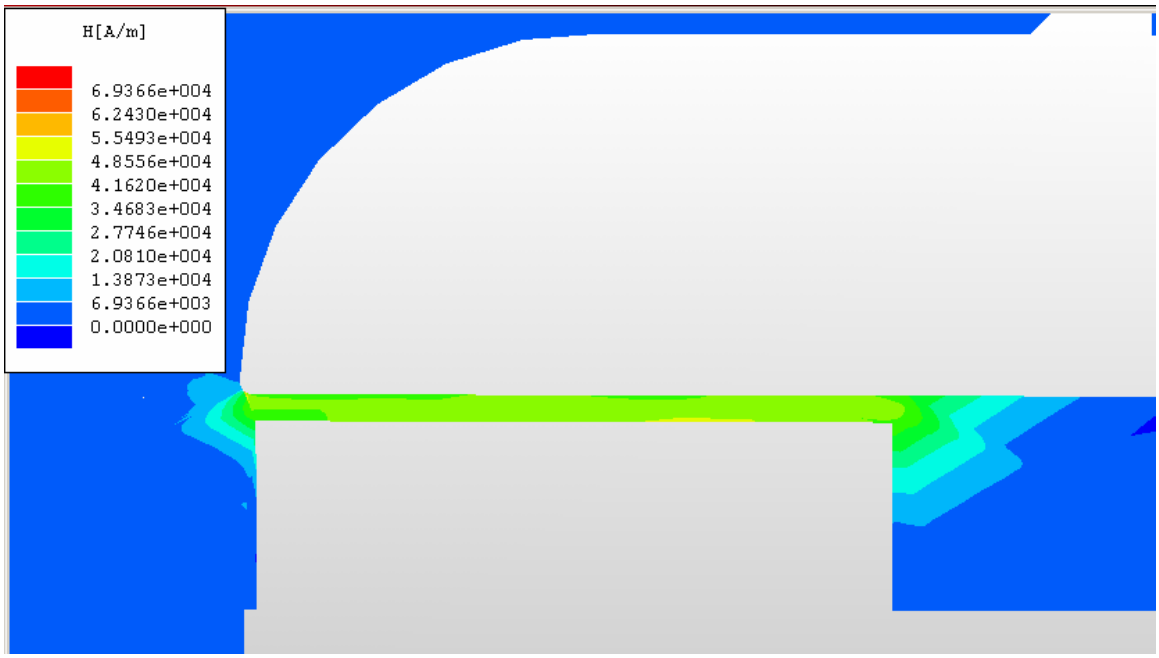

Figure 12. FEA results for first-generation MagneShock™: close-up showing magnetic field intensity in annular gap

Because of magnetic saturation in the electromagnet core, the magnetic flux density in the annular gap was severely limited. To improve the electromagnetic efficiency, design changes

were needed to increase the cross-sectional area of the core (where saturation was occurring) while keeping the components manufacturable.

2.4.2. Design optimization: "second generation" MagneShock™

The most significant changes made to the first-generation MagneShock™ design involved the addition of ferromagnetic material (1020 steel) within the electromagnet core. This enhancement was achieved by changing the piston design so that the stainless steel rod (non ferro-magnetic) no longer threaded into the core of the piston nut. This change allowed for a much larger volume of steel in the core. One critical design constraint was imposed: the second-generation design must utilize the same off-the-shelf electromagnet coil (525 turns, 27 ohms) as the previous design. Figure 13 shows the solid model for the updated (second-generation) MagneShock™ design.

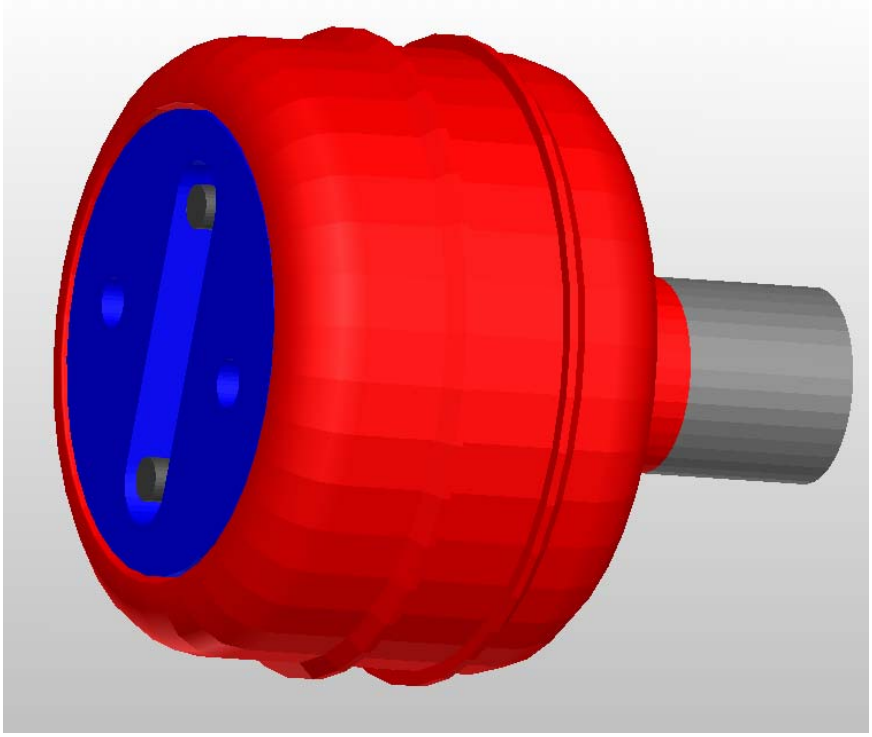

Figure 13. Updated MagneShock™ Design

The FEA results shown in Figure 14 and Figure 15 reveal that flux densities in the annular gap (controlled damping region) increased to 0.45 T from 0.36, a gain of 25%. Although the design modifications did not completely eliminate saturation in the core, it did allow for significantly higher annular gap flux densities and increased efficiencies. From these results, prototype MagneShocks™ were manufactured, and demonstrated improved performance. As seen from the figure, the redesigned shock developed an increased damping force of 26% for 1 in/s shock velocity and 288 mA coil current.

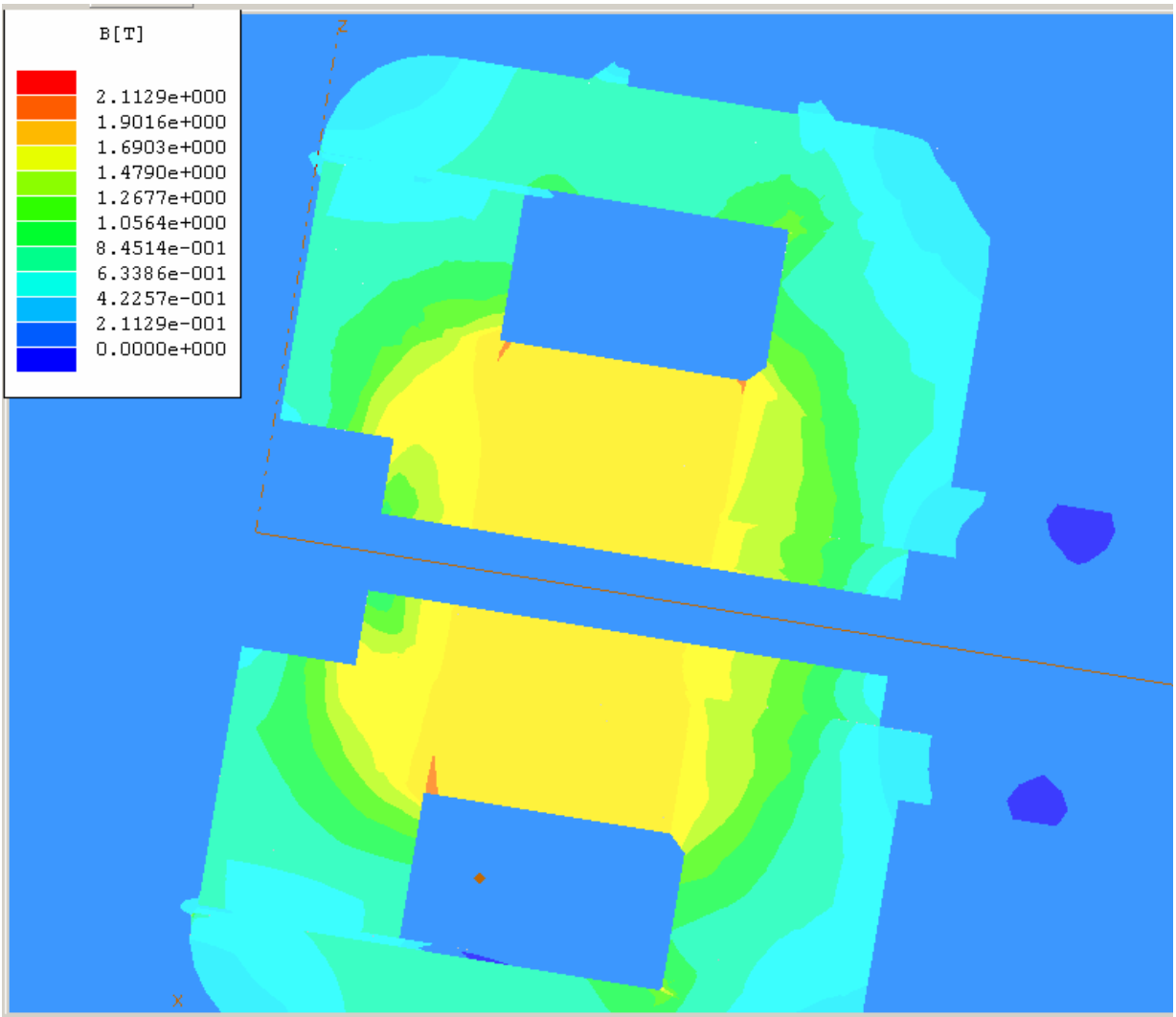

Figure 14. FEA results for second-generation MagneShock™: magnetic flux density

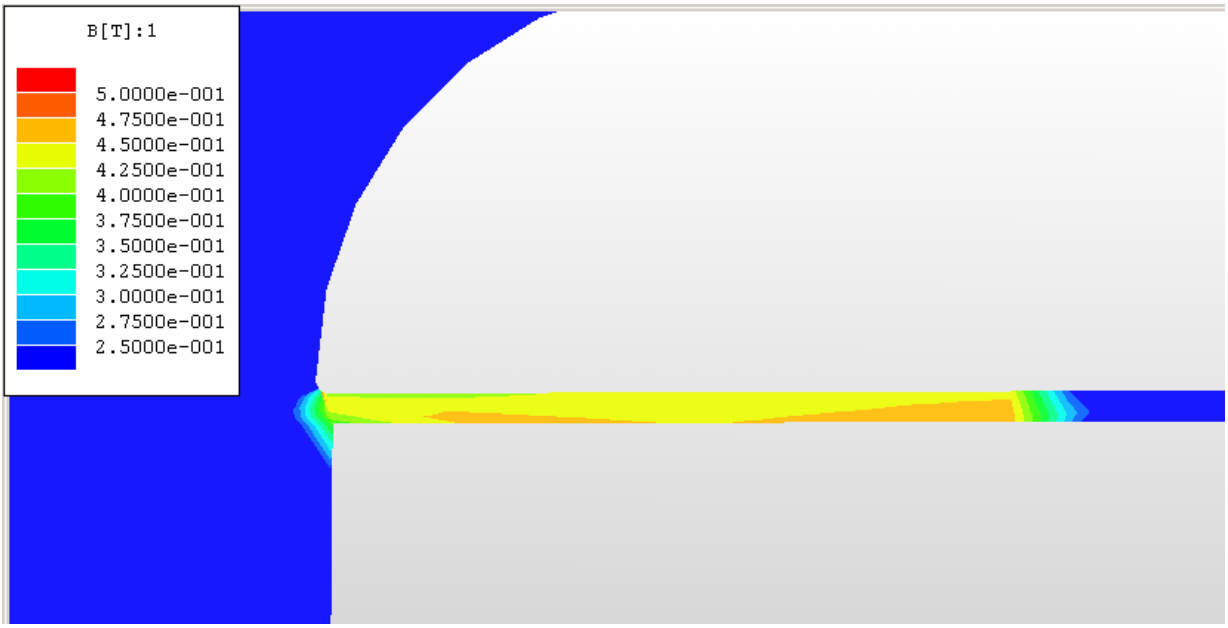

Figure 15. FEA results for second-generation MagneShock™: close-up showing magnetic flux density in annular gap

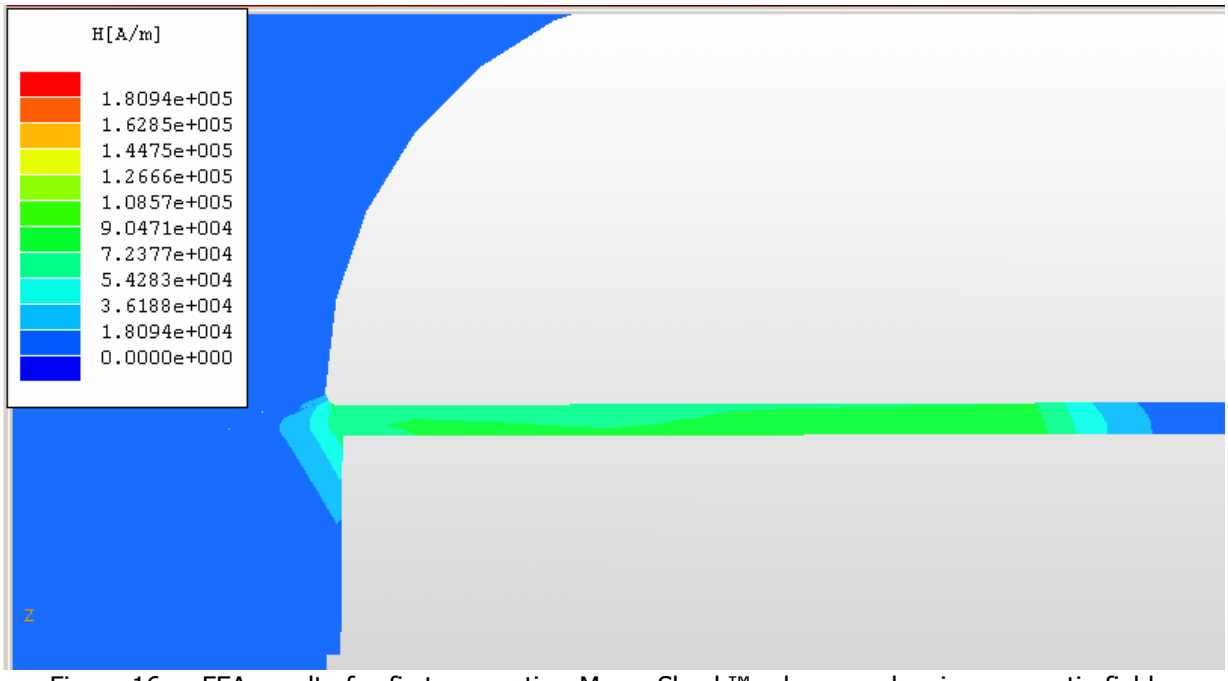

Figure 16. FEA results for first-generation MagneShock™: close-up showing magnetic field intensity in annular gap

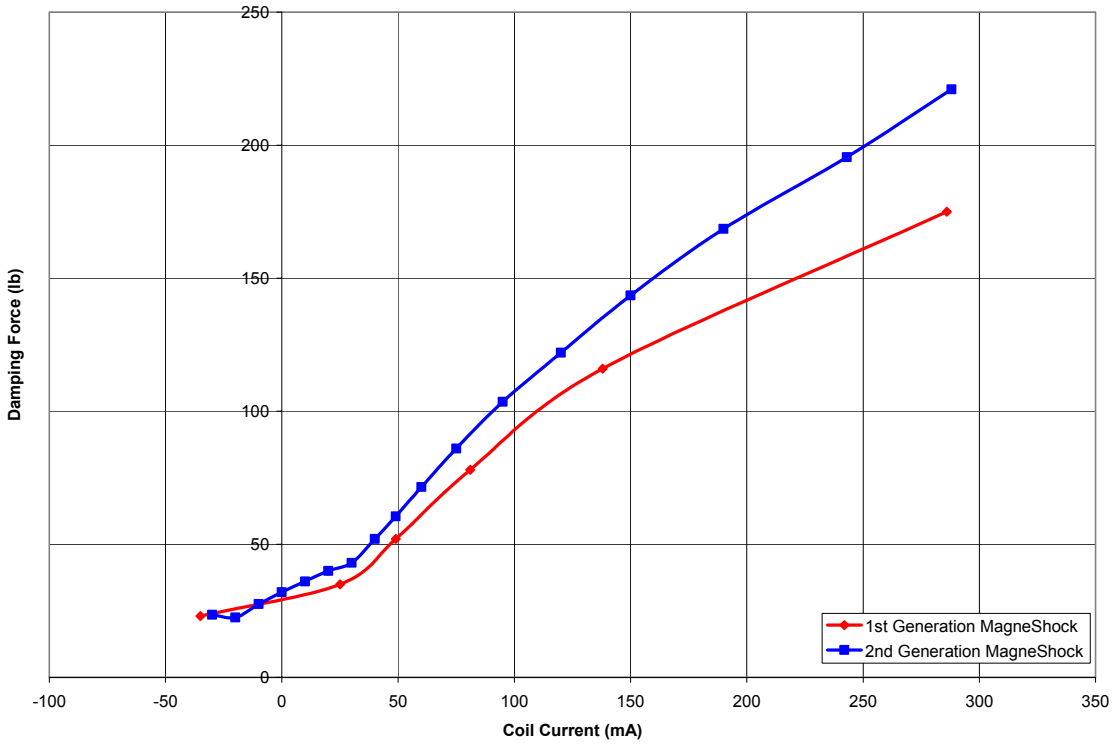

Figure 17. Experimental performance improvements in the second-generation MagneShock™: dynamometer measurements

2.4.3. Design optimization: "third generation" MagneShock™

Judging from the second-generation results, it became obvious that saturation could only be avoided (at 300mA) by continuing to increase the steel core volume. Since the through-hole for the coil wires could not be reduced in size, it became necessary to increase the inner diameter (ID) of the magnetic coil. Altering the shape of the electromagnetic coil would require costly retooling and component manufacture, but the performance benefits gained from this change were predicted to be significant. After several FEA design iterations using the Maxwell 3D software, one design resulted in consistent flux density throughout the piston, with no highly saturated sections (1.10T in electromagnet core). This allowed for even higher input current levels, and resulted in significantly higher flux densities in the annular gap (0.73). The coil ID was increased by approximately 40% while the coil cross-sectional area was retained (same number of windings), yet the overall piston height was

reduced, decreasing the "dead length" of the shock. This third-generation design will be incorporated in future MagneShock™ products, which require more efficient, dynamically extreme (very stiff to very soft) characteristics.

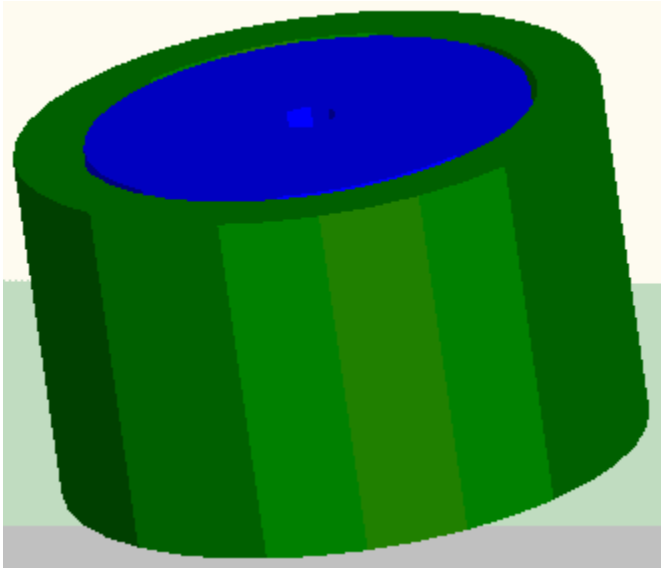

Figure 18. Prototype design with new coil.

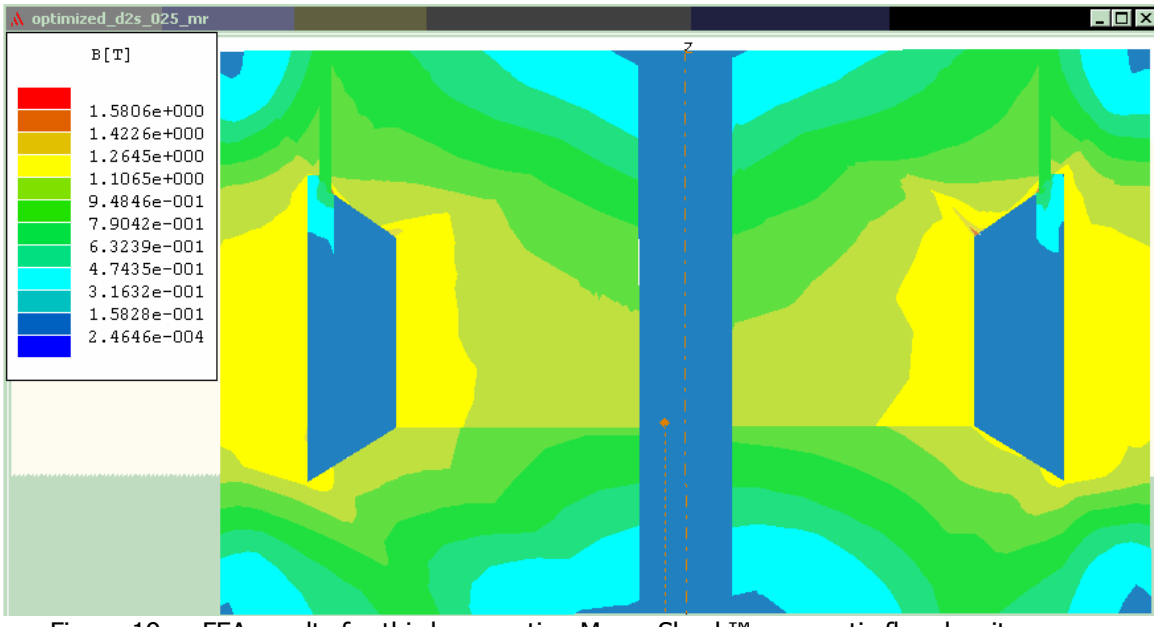

Figure 19. FEA results for third-generation MagneShock™: magnetic flux density

2.5. Comparison of FEA Results

As shown in the results of Table 2 and Figure 20, the second-generation design (retaining the original coil) accounted for an increase in MR fluid shear stress in the annular gap of approximately 47%. The third-generation design (incorporating a new, larger ID coil) provided tremendous improvements over the original design (160%). However, these performance gains come with the added cost of creating new tooling to manufacture the new coil. Unfortunately, neither of these proposed design changes was implemented on the test vehicle in time for testing. For that reason, all of the following simulations were performed without considering the advantages of the prototype designs.

Table 2. Comparison of results for magnetic circuit analysis

Ansoft Prototype Shock Modeling			
Description	Original "2nd generation" MagneShock™	Optimized piston with original coil	Optimized piston with a new coil shape
Coil current (assuming 525 turns) mA	300	300	300
Core Flux Density (T)	1.73	1.73	1.10
Annular Gap Flux Density (T)	0.36	0.45	0.73
Annular Gap Field Intensity (kA/m)	48	73	190
Shear Stress (kPa)	15	22	40

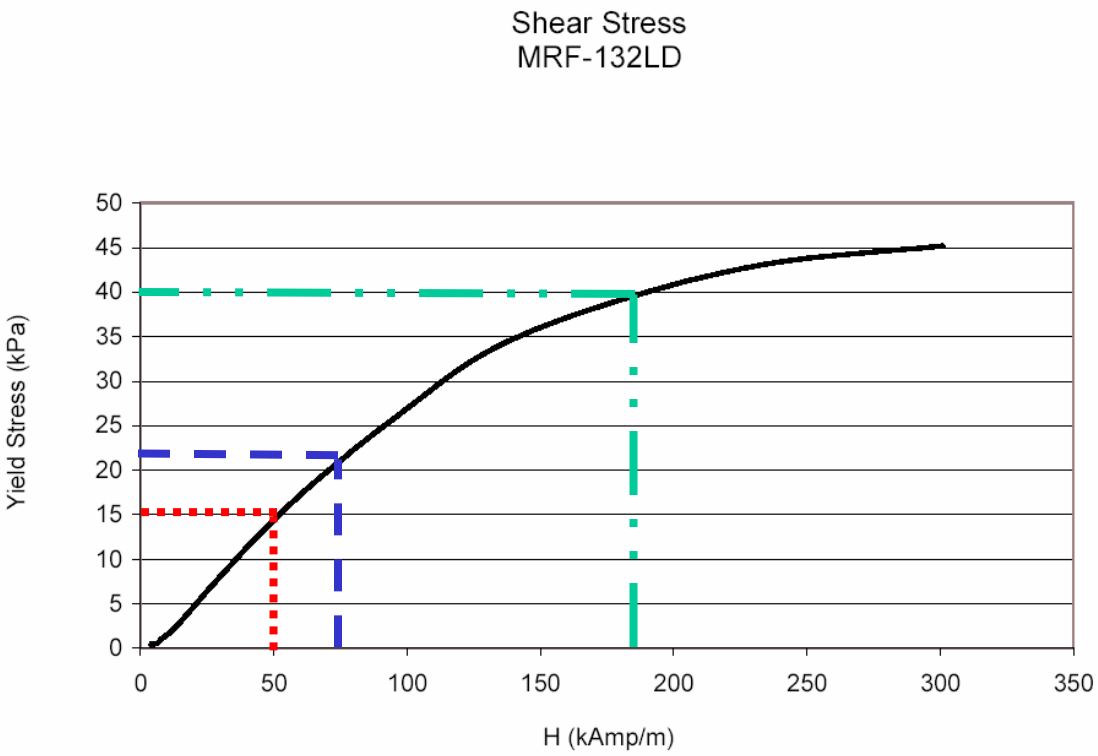

Figure 20. Graph illustrating realized improvements in efficiency

3. System Modeling

The controller synthesis and computer simulations were based on the popular quarter car model [1,2,3,13,16,1,20,28,20,39,40,43,43]. The model (Figure 21) takes into account the sprung and unsprung masses (m_b and m_w), tire stiffness and damping coefficients (k_t and b_t), and suspension stiffness and damping coefficients (k and b). Although this model neglects vehicle roll and pitch dynamics, it is known to accurately model the vertical dynamics [15] of primary interest to ride quality and handling performance. Using Newton's 2nd Law of Motion, the linear state equations can be readily derived:

$$\begin{aligned} k(y_w - y_b) + b(\dot{y}_w - \dot{y}_b) &= m_b \ddot{y}_b \\ k_t(y_g - y_w) + b_t(\dot{y}_g - \dot{y}_w) + k(y_b - y_w) + b(\dot{y}_b - \dot{y}_w) &= m_w \ddot{y}_w \end{aligned} \tag{1}$$

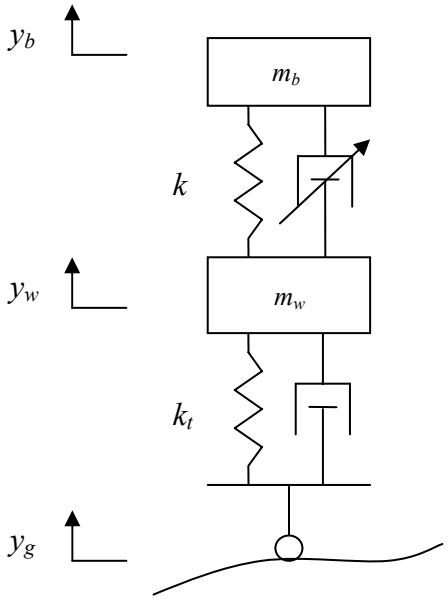

Figure 21. Quarter Car Suspension Model

Despite the popularity and simplicity of this linear model, passive and semi-active suspension components can exhibit nonlinear behavior that must be accounted for to accurately simulate

vehicle response. Specifically, damping values are significantly different in rebound and compression (rebound damping is usually higher than compression damping [16]). "Stiction" and bump-stops can also significantly alter suspension dynamics. To account for these nonlinearities, a more general state equation form is:

$$\begin{aligned} f_k(\Delta) + f_b &= m_b \ddot{y}_b \\ k_t\left(y_g - y_w\right) + b_t\left(\dot{y}_g - \dot{y}_w\right) - f_k(\Delta) - f_b &= m_w \ddot{y}_w \end{aligned} \tag{2}$$

where $\Delta = \left(y_w - y_b\right)$ represents suspension displacement, $f_k(\Delta)$ is a nonlinear spring force, and f_b is shock damping force.

For OE passive shocks, the damping force can be expressed:

$$f_b = f(\dot{\Delta}) \tag{3}$$

where $\dot{\Delta} = \left(\dot{y}_w - \dot{y}_b\right)$ and f are based on shock dynamometer data. Dynamic damping characteristics for MagneShock™ shock absorbers were experimentally measured in rebound and compression for a variety of speeds (1, 3, 6, and 12 inches per second). Damping values were interpolated between measurement points to estimate the complete behavior (Figure 22), and these characteristics were incorporated into the quarter car model, Equation (2).

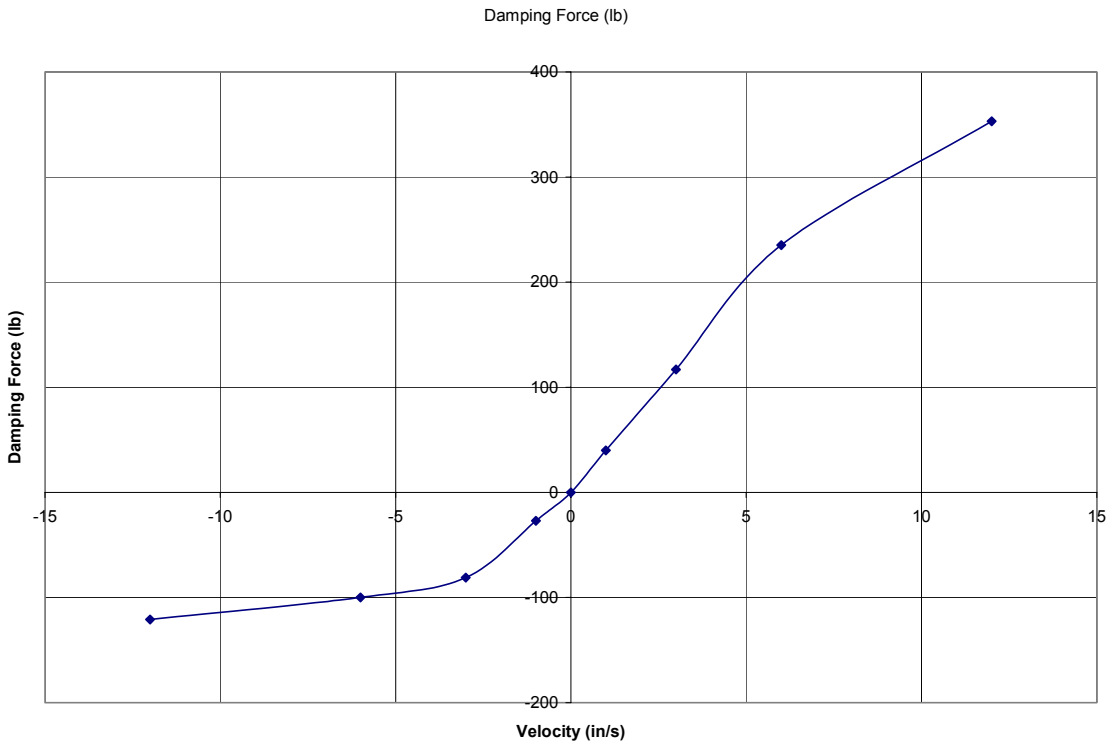

Figure 22. Passive shock damping characteristics (OE Shock)

The damping force characteristics for the MagneShock™ are dependent on velocity and control current:

$$f_b = f_b(\dot{\Delta}, i) \tag{4}$$

where i represents electromagnet coil current. Again, these nonlinear relationships were experimentally determined from shock dynamometer data, and incorporated into the state equations (2).

A parameter-driven Simulink™ model (9.2) was created to simulate the nonlinear quarter car dynamics (2). As previously mentioned, suspension bump-stops (rebound and compression) can limit vehicle suspension travel, and were included in the model. Other nonlinearities included possible loss of contact between the tire and road (which can occur at high wheel accelerations) and shock "stiction," which accounts for the high static seal frictions typical of MR shocks [13]. Spring and damping rates, vehicle masses, terrain inputs, and initial

conditions were easily adjustable to account for different vehicles and operating conditions. The vehicle parameters used for this simulation are listed in Table 3.

Table 3. Vehicle simulation parameters

Variable	Definition	Value (units)
m_b	Sprung Mass	1100 (lb)
m_w	Unsprung Mass	125 (lb)
k	Suspension Spring Rate	440 (lb/in)
k_t	Tire Spring Rate	2640 (lb/in)
b	Shock Damping Coefficient	Nonlinear
b_t	Tire Damping Coefficient	5 (lb·s/in)

3.1. Model Validations

To establish the accuracy of the quarter car model, computer simulation results were compared with experimental data collected from an instrumented vehicle equipped with passive OE shocks. A speed bump, modeled as a half sinusoid, was chosen as the terrain input for these evaluations. The speed bump measured 1.75" (44.45 mm) high and 38" (965.2 mm) long.

Suspension displacements were measured for several different vehicle speeds and compared to the simulated quarter car responses. Figure 23, Figure 24, Figure 25, and Figure 26 compare the measured and simulated suspension displacements (front left and front right corners) for vehicle speeds of 5 mph, 10 mph, 15 mph, and 25 mph, respectively.

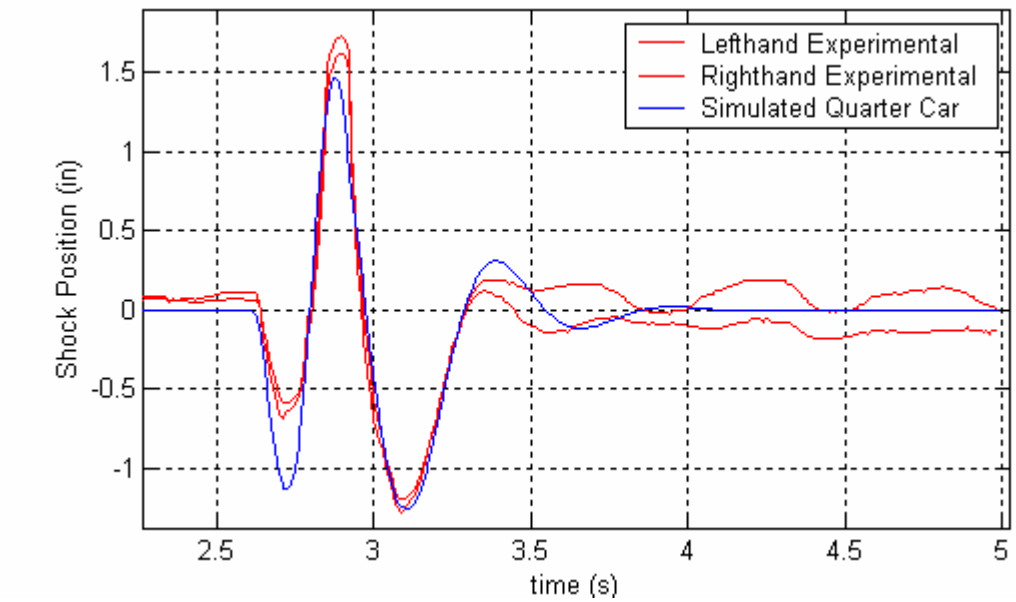

Figure 23. Quarter car model validations: measured and simulated speed bump responses at 5 mph

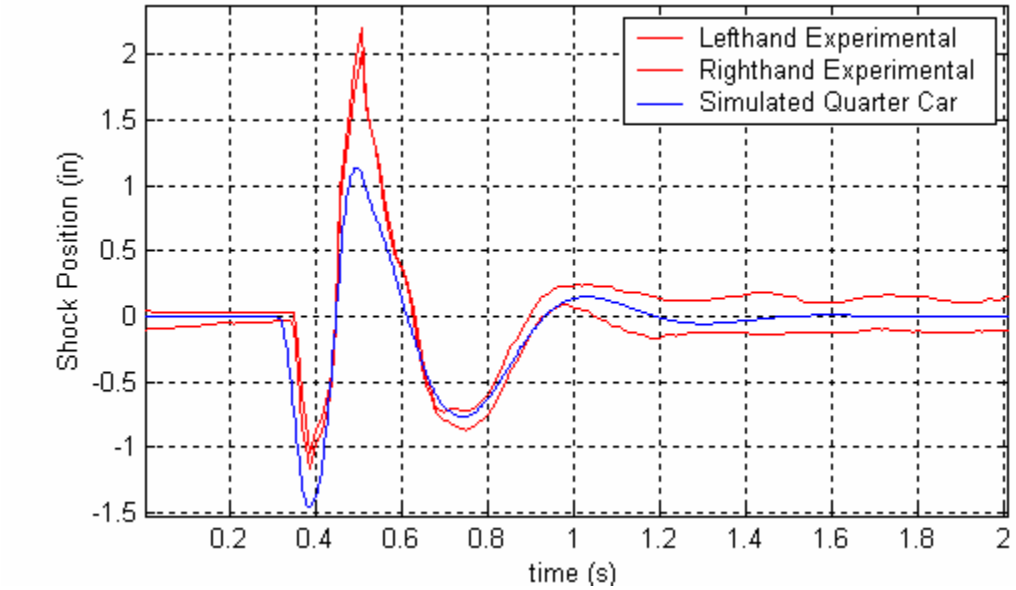

Figure 24. Quarter car model validations: measured and simulated speed bump responses at 10 mph

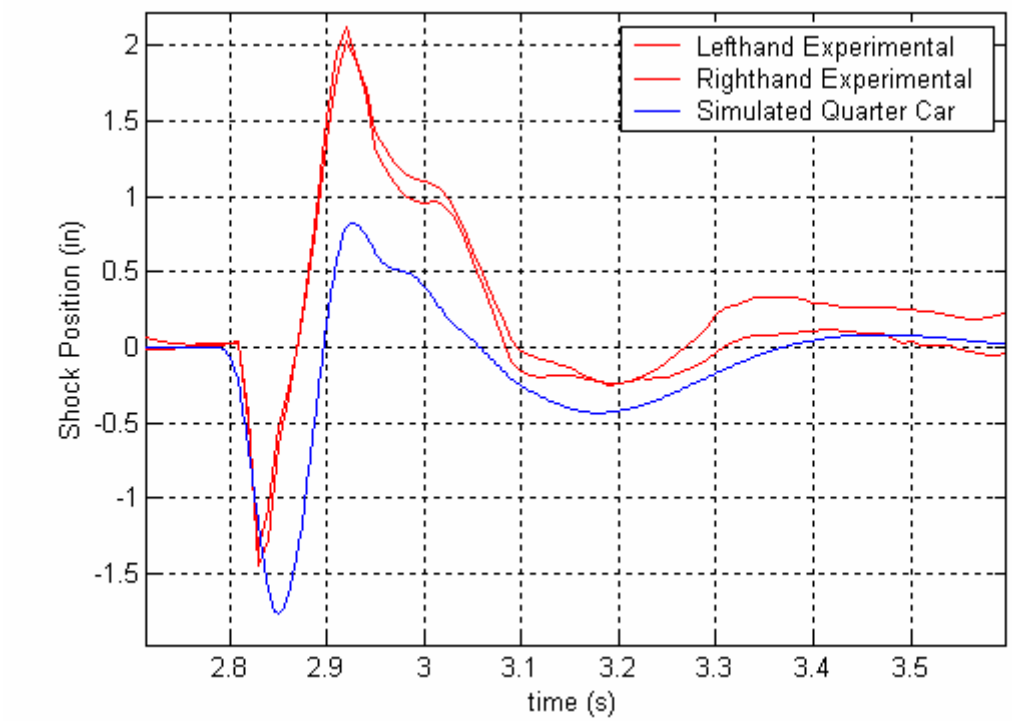

Figure 25. Quarter car model validations: measured and simulated speed bump responses at 15 mph

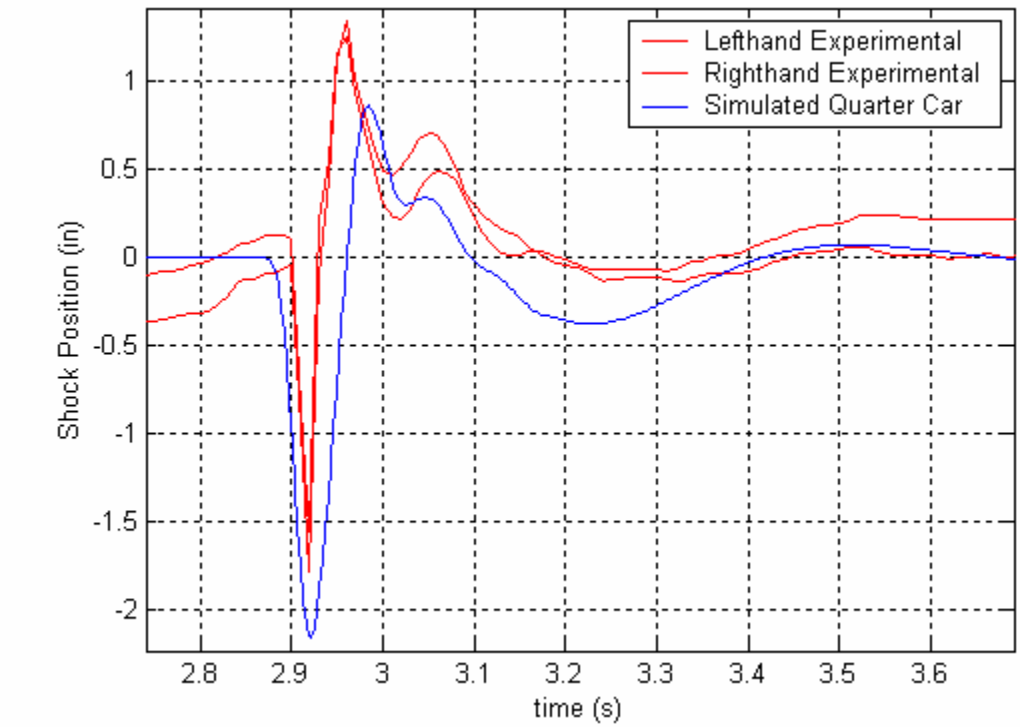

Figure 26. Quarter car model validations: measured and simulated speed bump responses at 25 mph

This data indicates that the simulated suspension dynamics closely correspond to the measured responses, and can be used effectively for controller design. Although some discrepancies between measured and modeled responses do exist, it should be recognized that the quarter vehicle model neglects pitch and roll dynamics, which play larger roles at higher vehicle speeds. Additionally, the driving surface was not completely smooth, and the speed bump profile deviated slightly from the modeled half sinusoid.

4. Fuzzy Logic Algorithm Development

Fuzzy logic controllers (FLCs) have been successfully applied to the control of semi-active vehicle suspensions, and have demonstrated improved ride quality and handling characteristics, sometimes more successfully than conventional control schemes [1,4,23,24,28,39,43]. Fuzzy logic can account for system nonlinearities [40], and benefits directly from expert control knowledge (rules). Because of its intuitive structure, fuzzy logic can greatly reduce development time, and has been demonstrated to reduce design-to-market cycle time [1,40]. Also, membership functions and rules can be easily adjusted after initial testing.

Developed in the 1960's by Lotfi Zadeh, fuzzy logic represents one way to incorporate human expertise into the control of a dynamic system [40]. Although its role in engineering was quite controversial for some time, fuzzy logic control has proven to be a reliable method for many industrial applications [40]. Similar to human reasoning, fuzzy logic takes in a number of environmental input variables, and based on a subset of rules concerning the inputs, delivers an output. Fuzzy logic was utilized for this research because it represents the only control algorithm that could effectively incorporate expert rules derived from Carrera's experience in the design, optimization, and operation of racing shocks.

The Fuzzy Logic Control Toolbox, provided with Matlab / Simulink™ software, allowed for the creation and alteration of fuzzy sets, membership functions, and rules (Figure 27). Starting with expert knowledge related to vehicle suspension control (in linguistic terms), the fuzzy sets, rules, and associated outputs were determined accordingly.

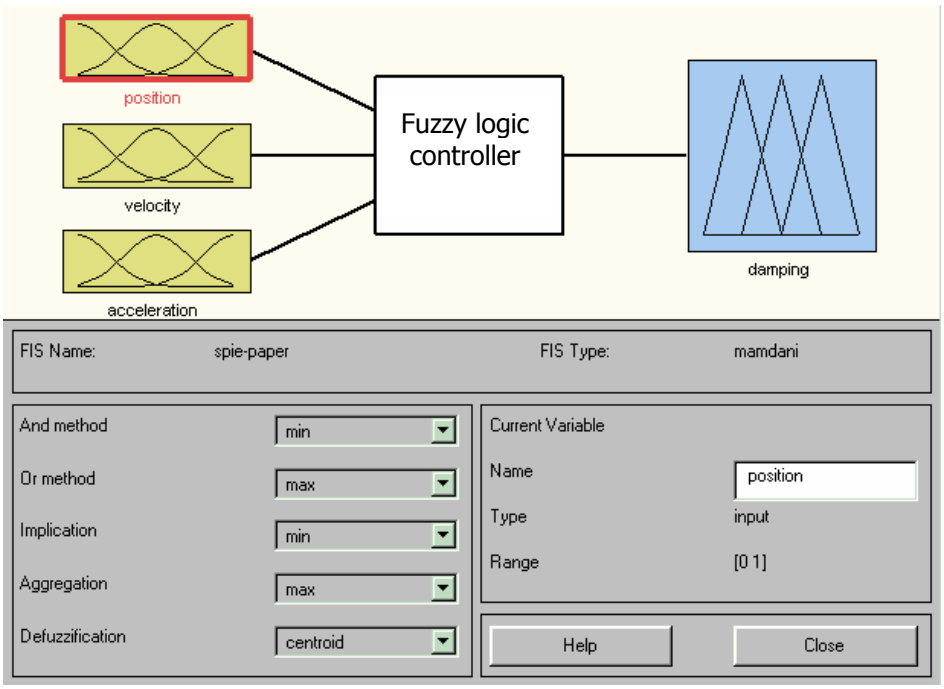

Figure 27. Matlab's Fuzzy Logic Control Toolbox interface

The FLC rules were based on suspension displacement, velocity, and acceleration. The number and distributions of membership functions for velocity were based on damping conventions established in the racing shock industry (Figure 28). The number and distributions of membership functions for position and acceleration were based on computer simulation results for various operating conditions. It should be noted that because damping properties differ in compression and rebound, the membership functions for suspension displacement are not symmetric around the static ride height.

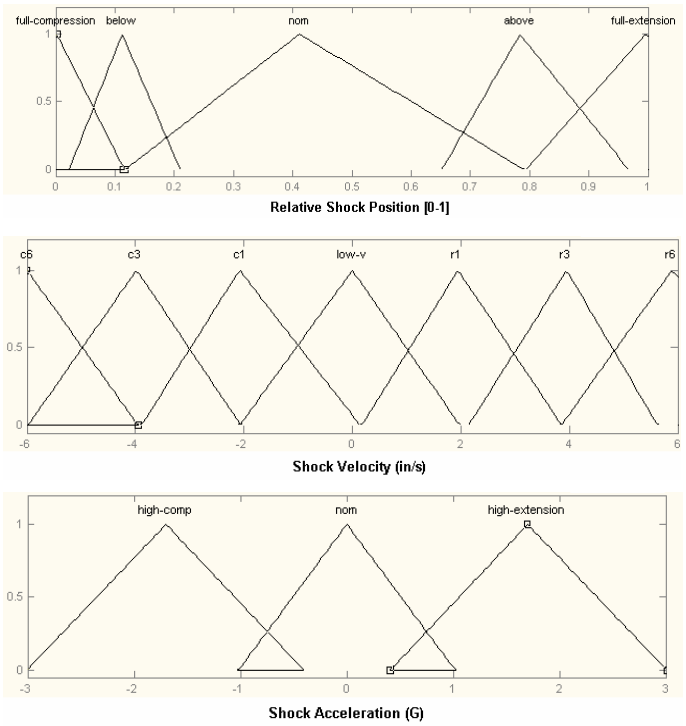

Figure 28. Representative FLC membership functions

A variety of different rule sets were evaluated in simulation and experimentation. Two of the most successful rule sets are shown in Table 4 and Table 5, labeled FLC A and FLC B, respectively. FLC A uses only position and velocity as input variables. FLC B uses position, velocity, and acceleration as input variables. Figure 29 shows a visual representation of the FLC B controlling output.

Table 4. Fuzzy logic rules for FLC A

Rule Number	Input Conditions		Desired Damping
	Position	Velocity	
1	---	Low	Low
2	---	Low compression	Low
3	---	Medium compression	Low
4	---	High compression	Low
5	---	Low rebound	Medium
6	---	Medium rebound	Medium
7	---	High rebound	High
8	Compressed	---	Low
9	Extended	---	Low
10	Fully Compressed	---	High
11	Fully Extended	---	High

Table 5. Fuzzy logic rules for FLC B

Rule Number	Input Conditions			Desired Damping
	Position	Velocity	Acceleration	
1	---	Low compression	High compression	Low
2	---	Medium compression	High compression	Low
3	---	High compression	High compression	Low
4	---	Low compression	High extension	Medium
5	---	Medium compression	High extension	Medium
6	---	High compression	High extension	Medium
7	---	Low rebound	High extension	High
8	---	Medium rebound	High extension	High
9	---	High rebound	High extension	High
10	---	Low rebound	High compression	Medium
11	---	Medium rebound	High compression	Medium
12	---	High rebound	High compression	Medium
13	Nearly Compressed	---	---	High
14	Extended	---	---	Low
15	Fully Extended	---	---	High
16	Fully Compressed	---	---	High
17	---	Low	---	Low
18	---	Low compression	Nominal Acceleration	Low
19	---	Medium compression	Nominal Acceleration	Low
20	---	High compression	Nominal Acceleration	Low
21	---	Low rebound	Nominal Acceleration	Medium
22	---	Medium rebound	Nominal Acceleration	Medium
23	---	High rebound	Nominal Acceleration	Medium

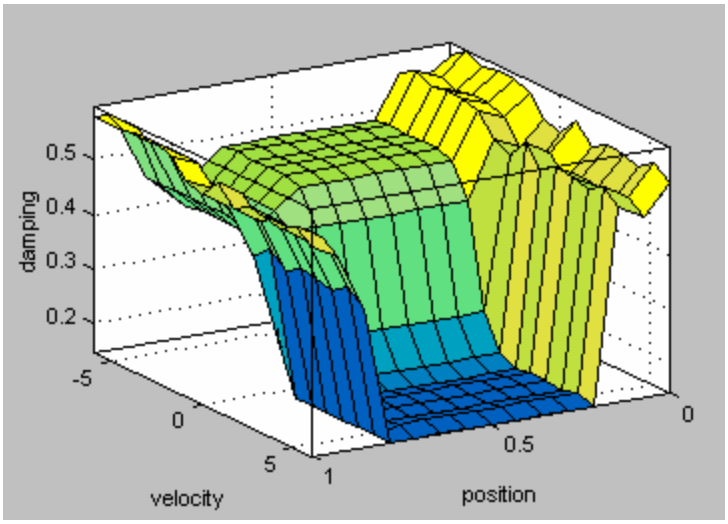

Figure 29. Fuzzy logic output with respect to position and velocity

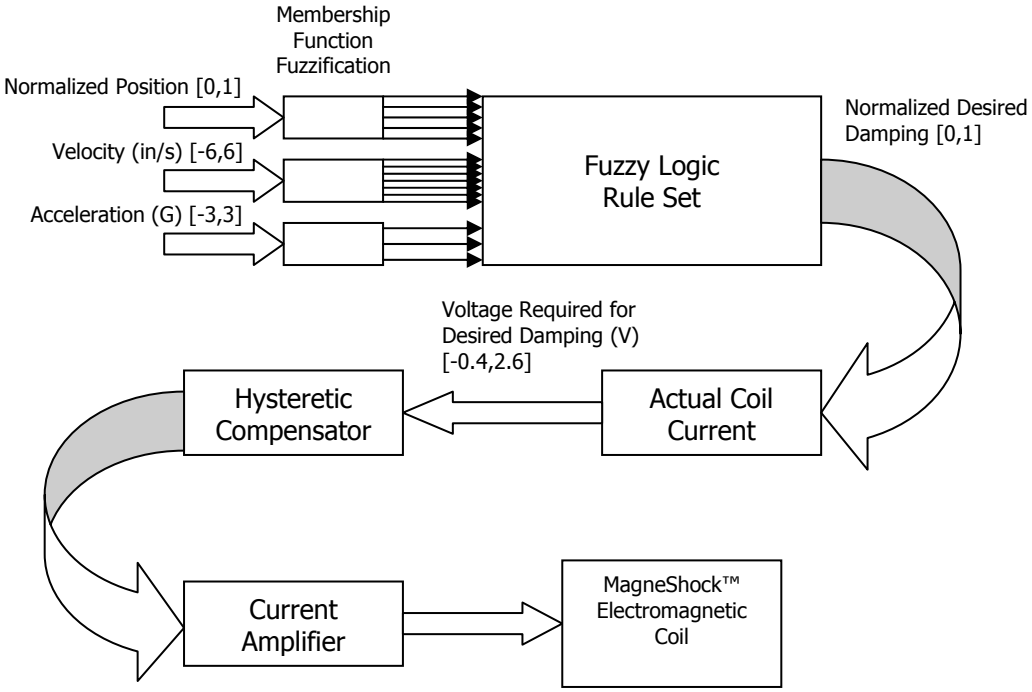

Figure 30. Block Diagram of Fuzzy Logic Control Algorithm B (FLC A lacks acceleration input)

Defuzzification resulted in a normalized damping value, where 1 represented the highest value of damping and 0 represented the lowest value of damping obtainable. This normalized value was then altered to represent a desired coil current value between -40 –

260mA. 260mA was chosen for the maximum current to avoid magnetic saturation. Additionally, an inversion algorithm was created to compensate for the hysteretic behavior and achieve the desired shock damping (algorithm schematic shown in Figure 30).

5. FLC Performance Evaluations: Simulation Results

To assist in the development and evaluate the effectiveness of FLC algorithms for the semi-active suspension system, computer simulations were conducted using Matlab/Simulink™ software. The nonlinear quarter car model (2) was excited using a variety of terrain inputs including sinusoids, swept sinusoids, speed bumps, step inputs, and actual road measurement data (taken from a Maryland highway in 1999 using an Automatic Road Analyzer (ARAN) device). Two of the FLC algorithms evaluated (FLC A & FLC B) are presented here, with ride quality and handling performance assessments based on absorbed power, RMS sprung mass acceleration, RMS suspension travel (RMS rattle space), and RMS normal force.

While RMS sprung mass acceleration is commonly used to quantify ride quality, this method does not account for the effects of excitation frequency and amplitude on the human body. Gillespie compiled a series of studies indexing the comfort level of an average person undergoing sinusoidal excitation [16,50]. These studies showed that frequency and displacement both have adverse effects on human comfort over an extended period of time. To account for these, the analysis of passenger absorbed power was developed [41]. This method, now used by the U.S. Army and NATO, establishes the maximum allowable speed for military vehicles traveling over rough terrains by limiting the absorbed power (calculated using frequency-weighted vertical acceleration measurements) of the occupants to 6 Watts [31,41,50]. Absorbed power is defined as the product of the mean squared acceleration and K_i:

$$\text{Average AP} = \sum_{i=0}^{\text{N}} K_i A_i^{\,2} RMS \tag{5}$$

The K_i parameter is function that is different depending on frequency, but constant for each frequency. The value of the parameter K_i was defined by Lee and Pradko [31].

Handling performance is frequently quantified using RMS tire/road normal forces. Theoretically, road holding ability is only related to the normal force between tire and road, without dependency on tire/road adhesion, tire slip angle, tire deflection, camber thrust, caster, tire temperature, or other suspension variables [16]. Reducing fluctuations in tire/road normal forces increases the predictably of vehicle behavior due to the consistency of tractive forces [16]. To maximize its effect on handling, the absolute value of this RMS normal force is subtracted from the normal force under static conditions.

Passive and semi-active control simulations were performed for identical road inputs and compared. Results of RMS sprung-mass acceleration, RMS suspension travel, and RMS normal force were computed and tabulated. Graphs and the maximum values of the absorbed power were generated. Additionally, the absolute body displacement was also found. The following sections highlight results from specific computer simulations.

5.1. Step Input Responses

The performance of fuzzy logic control vs. passive damping was compared for step changes in terrain. Figure 31 shows simulated sprung mass responses to a 1" step terrain input for controlled and passive damping cases. Figure 32 shows the resulting absorbed power calculations for these step responses, and Table 6 summarizes the performance statistics.

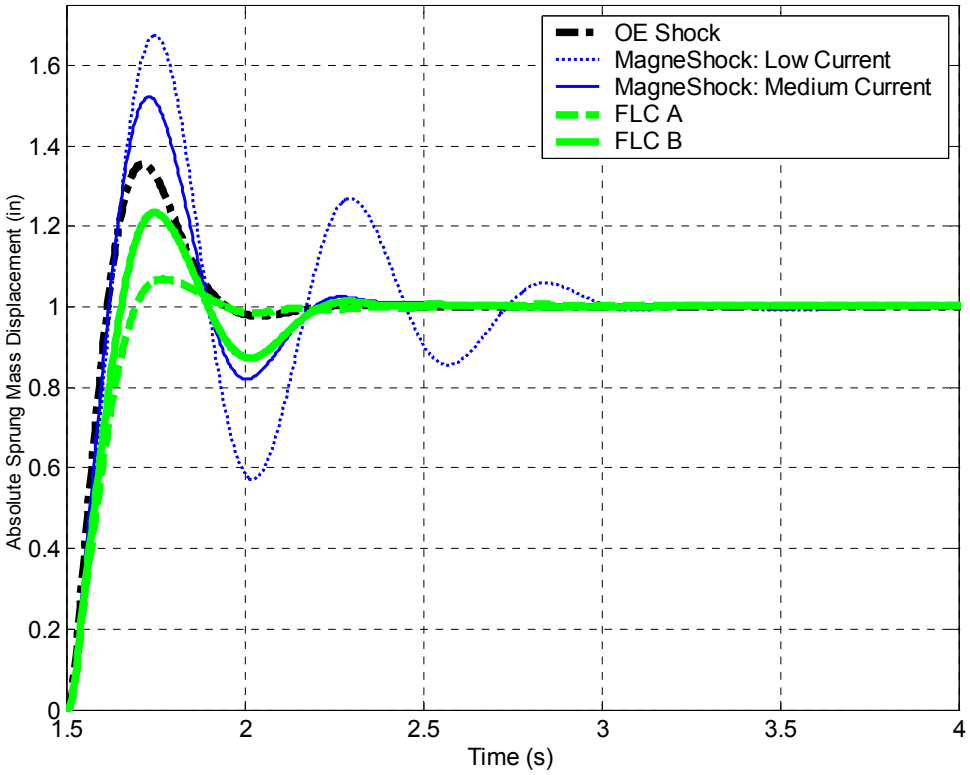

Figure 31. FLC performance evaluations: sprung mass responses to 1" step input

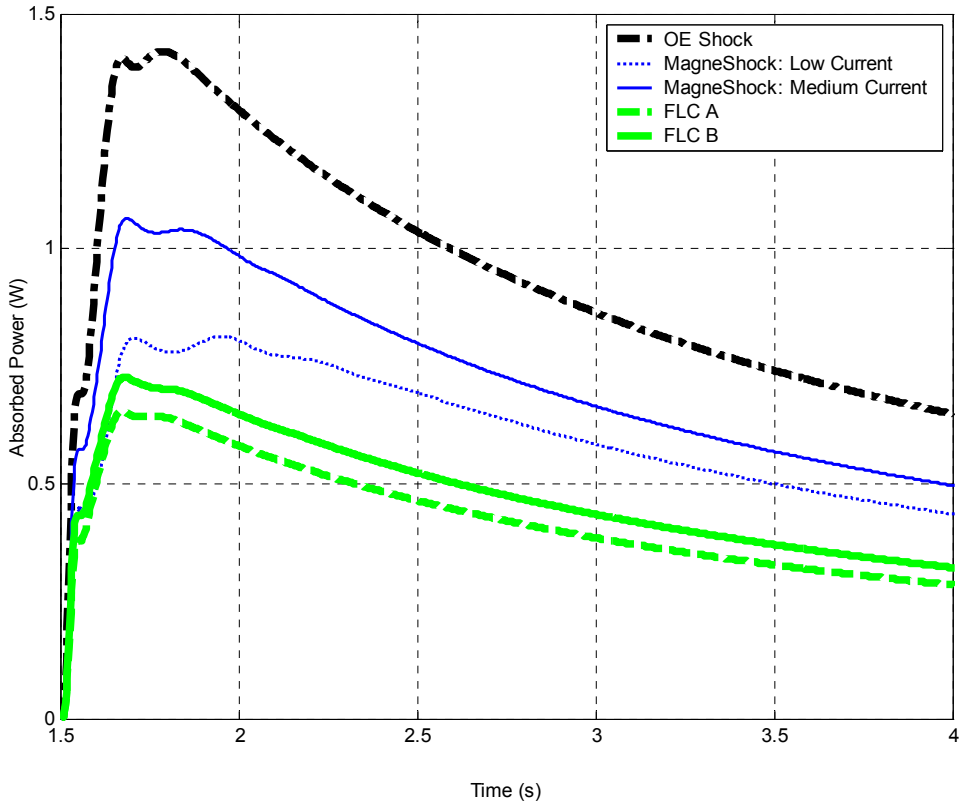

Figure 32. FLC performance evaluations: absorbed power for 1" step inputs

Table 6. FLC simulation results: 1" step input

	OE Passive Shock	MagneShock™ Passive A (Low-Damping)	MagneShock™ Passive B (Medium Damping)	FLC MagneShock ™ A	FLC MagneShock™ B
6 Watt Absorbed Power (W)*	1.42	0.81	1.06	0.66	0.72
RMS Sprung Mass Acceleration (G)	0.0142	0.0303	0.0220	0.0166	0.0187
RMS Suspension Travel (in)	0.0224	0.0608	0.0333	0.0218	0.0263
RMS Tire Normal Force (lb)	1226.37	1226.35	1226.36	1226.44	1226.41

*Approximate Maximum Value

Figure 33 shows simulated sprung mass responses to a 3" step terrain input for controlled and passive damping cases. Figure 34 shows the resulting absorbed power calculations for these step responses, and Table 7 summarizes the performance statistics.

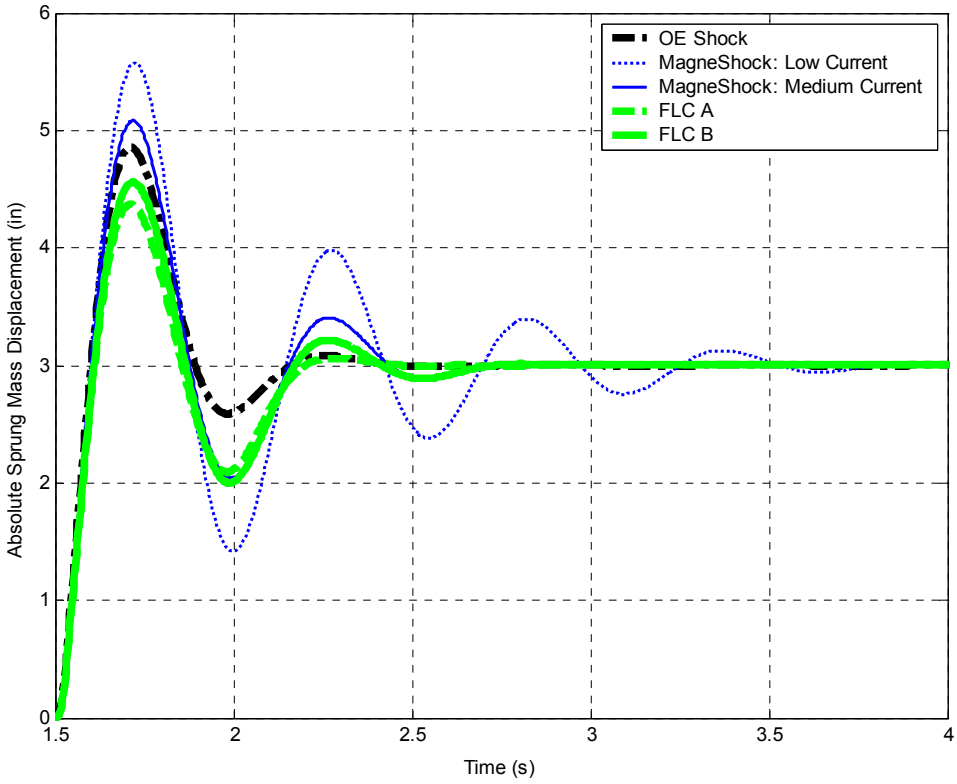

Figure 33. FLC performance evaluations: sprung mass responses to 3" step input

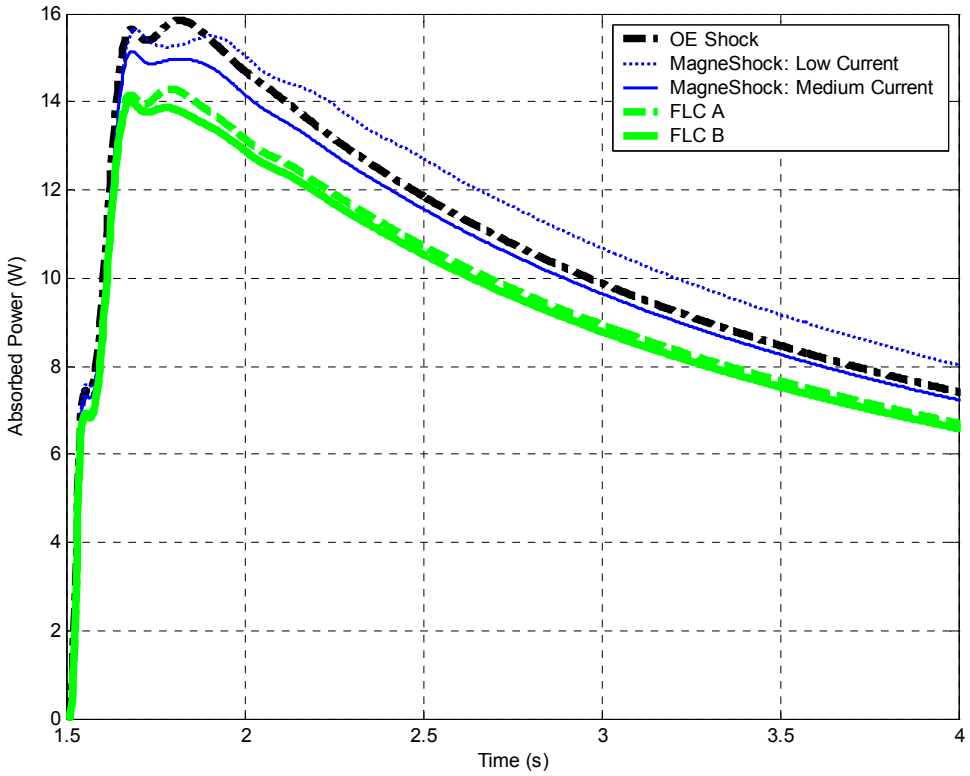

Figure 34. FLC performance evaluations: absorbed power for 3″ step inputs

Table 7. Quarter Car Simulation Results: 3″ Step input

	OE Passive Shock	MagneShock™ Passive A (Low-Damping)	MagneShock™ Passive B (Medium Damping)	FLC MagneShock™ A	FLC MagneShock™ B
6 Watt Absorbed Power (W)*	15.8	15.6	15.2	14.3	14.0
RMS Sprung Mass Acceleration (G)	0.0561	0.1072	0.0740	0.0635	0.0681
RMS Suspension Travel (in)	0.0974	0.2236	0.1335	0.1010	0.1159
RMS Tire Normal Force (lb)	1229.10	1229.11	1229.10	1229.15	1229.14

*Approximate Max Value

5.2. Sinusoidal Input

Figure 35 shows simulated sprung mass responses to a 2" amplitude, 100" long sinusoid bump at 2 mph for controlled and passive damping cases. Figure 36 shows the resulting absorbed power calculations for these step responses, and Table 8 summarizes the performance statistics.

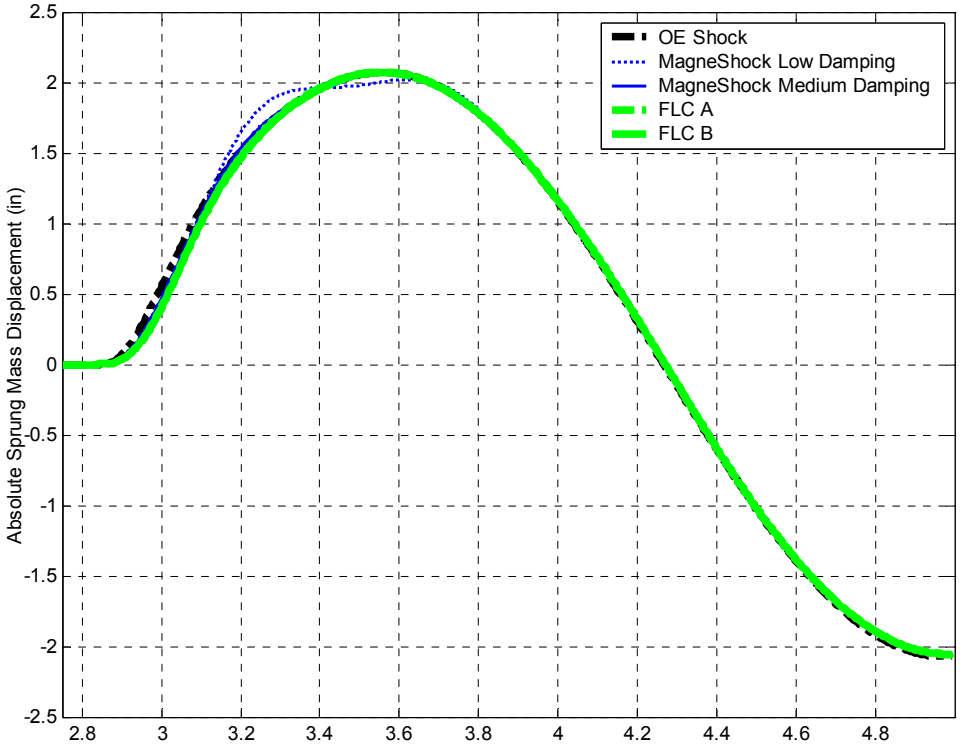

Figure 35. FLC performance evaluations: sprung mass response to a 2" amplitude sinusoid at 2 mph

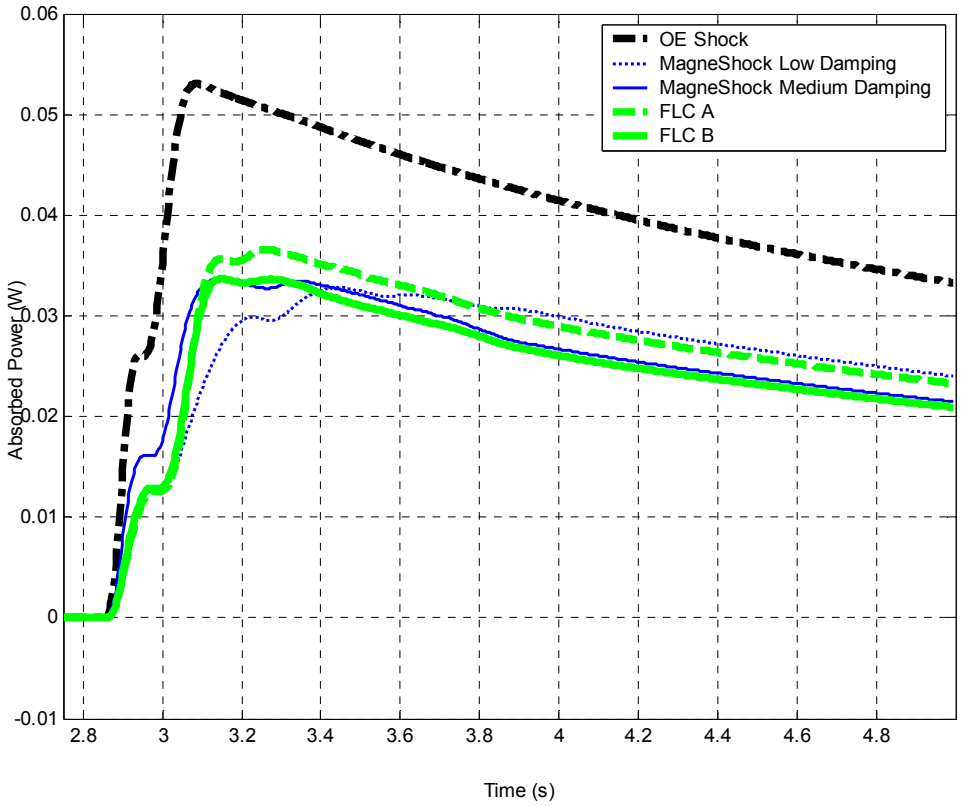

Figure 36. FLC performance evaluations: absorbed power for a 2" amplitude sinusoid at 2 mph

Table 8. Quarter Car Simulation Results: Sinusoidal Input, 2 mph, 100" wavelength, 2" amplitude

	OE Passive Shock	MagneShock™ Passive A (Low-Damping)	MagneShock™ Passive B (Medium Damping)	FLC MagneShock™ A	FLC MagneShock™ B
6 Watt Absorbed Power (W)*	0.053	0.0328	0.0334	0.0366	0.0337
RMS Sprung Mass Acceleration (G)	0.0108	0.0124	0.0114	0.0118	0.0121
RMS Suspension Travel (in)	0.0221	0.0288	0.0248	0.0257	0.0250
RMS Tire Normal Force (lb)	1225.11	1225.12	1225.11	1225.11	1225.11

*Approximate Maximum Value

Figure 37 shows simulated sprung mass responses to a 2" amplitude, 100" long sinusoid bump at 5 mph for controlled and passive damping cases. Figure 38 shows the resulting absorbed power calculations for these step responses, and Table 9 summarizes the performance statistics.

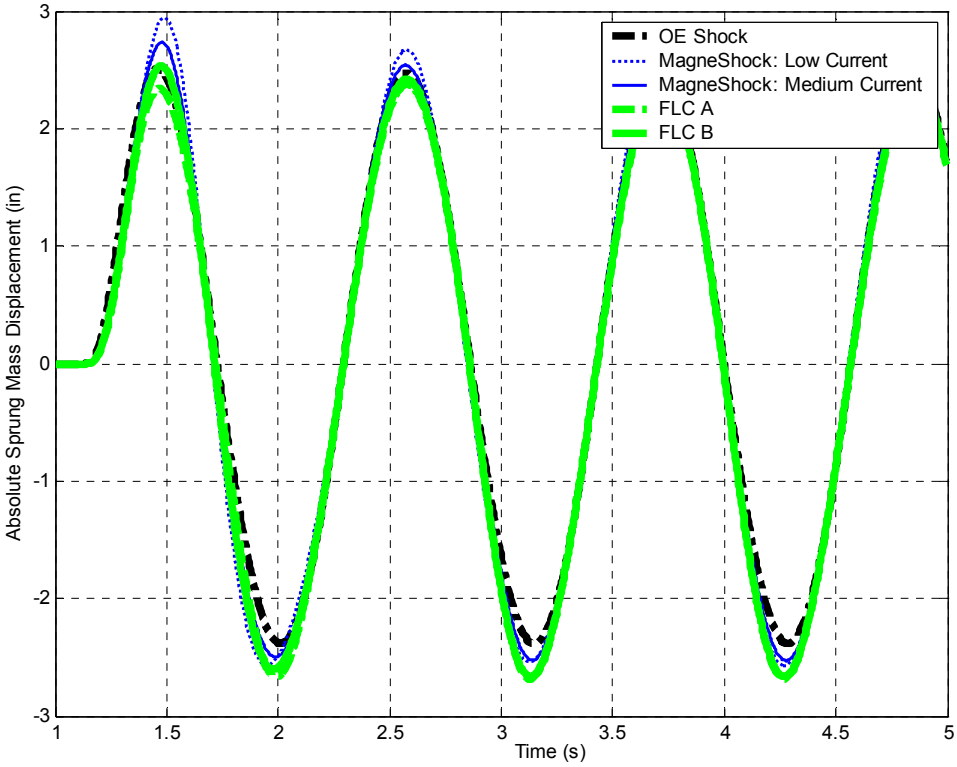

Figure 37. FLC performance evaluations: sprung mass response to a 2" amplitude sinusoid at 5 mph

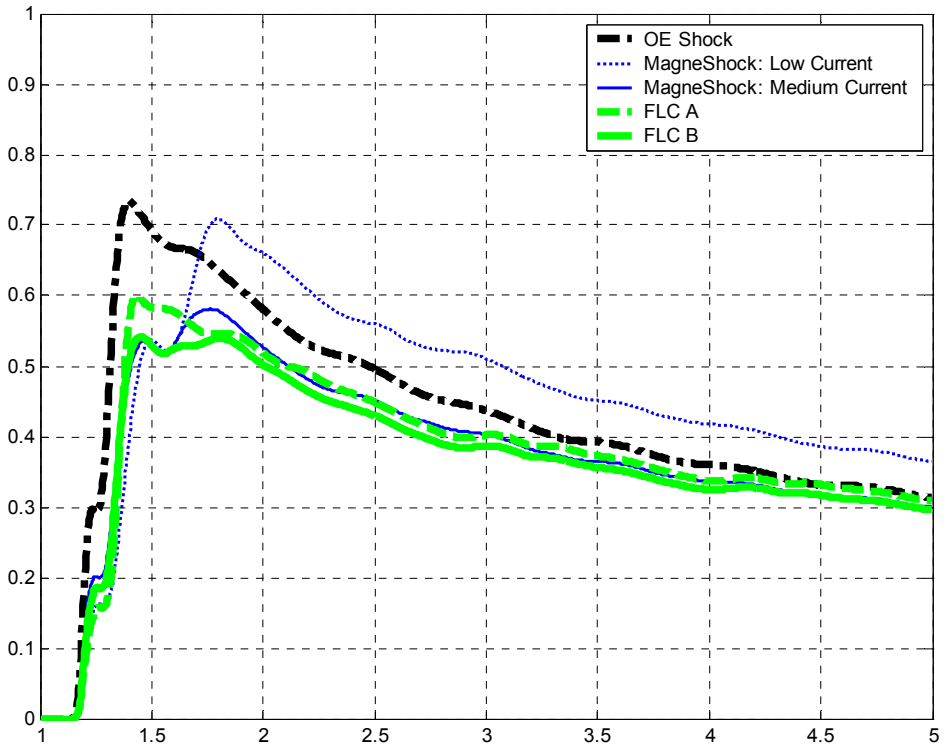

Figure 38. FLC performance evaluations: absorbed power for a 2" amplitude sinusoid at 5 mph

Table 9. Quarter Car Simulation Results: Sinusoidal Input, 5 mph, 100" wavelength, 2" amplitude

	OE Passive Shock	MagneShock™ Passive A (Low-Damping)	MagneShock™ Passive B (Medium Damping)	FLC MagneShock™ A	FLC MagneShock™ B
6 Watt Absorbed Power (W)*	0.73	0.71	0.57	0.60	0.54
RMS Sprung Mass Acceleration (G)	0.1024	0.1145	0.1080	0.1045	0.1062
RMS Suspension Travel (in)	0.2109	0.2812	0.2495	0.2395	0.2467
RMS Tire Normal Force (lb)	1218.78	1218.25	1218.69	1219.12	1218.98

*Approximate Maximum Value

Figure 39 shows simulated sprung mass responses to a 2" amplitude, 100" long sinusoid bump at 6 mph for controlled and passive damping cases. Figure 40 shows the resulting absorbed power calculations for these step responses, and Table 10 summarizes the performance statistics.

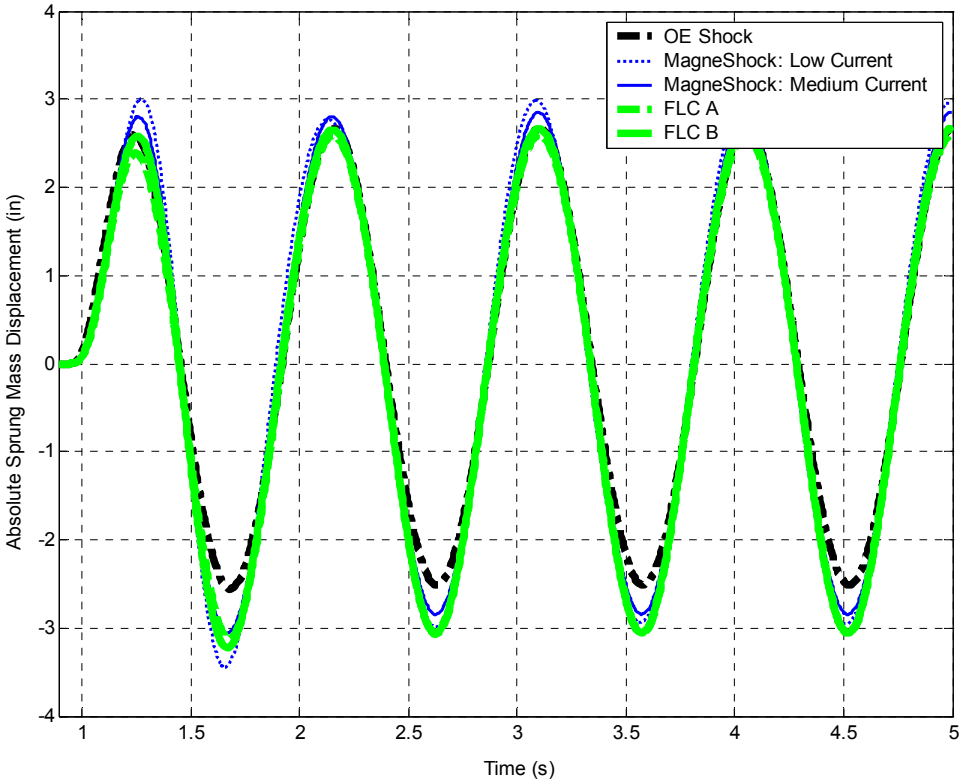

Figure 39. FLC performance evaluations: sprung mass response to a 2" amplitude sinusoid at 6 mph

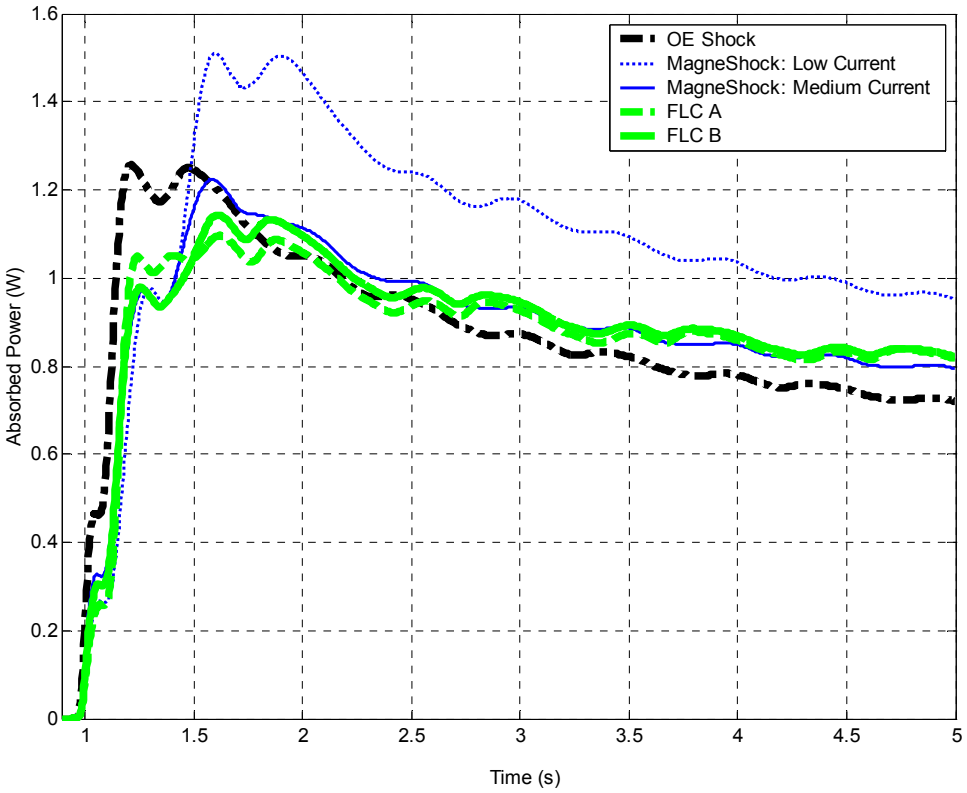

Figure 40. FLC performance evaluations: absorbed power for a 2" amplitude sinusoid at 6 mph

Table 10. Quarter Car Simulation Results: Sinusoidal Input, 6 mph, 100" wavelength, 2" amplitude

	OE Passive Shock	MagneShock™ Passive A (Low-Damping)	MagneShock™ Passive B (Medium Damping)	FLC MagneShock™ A	FLC MagneShock™ B
6 Watt Absorbed Power (W)*	1.25	1.5	1.22	1.09	1.14
RMS Sprung Mass Acceleration (G)	0.1578	0.1879	0.1746	0.1690	0.1735
RMS Suspension Travel (in)	0.3100	0.4545	0.4022	0.3876	0.4041
RMS Tire Normal Force (lb)	1225.17	1224.03	1224.63	1224.88	1224.80

*Approximate Maximum Value

Figure 41 shows simulated sprung mass responses to a 2" amplitude, 100" long sinusoid bump at 8 mph for controlled and passive damping cases. Figure 42 shows the resulting

absorbed power calculations for these step responses, and Table 11 summarizes the performance statistics.

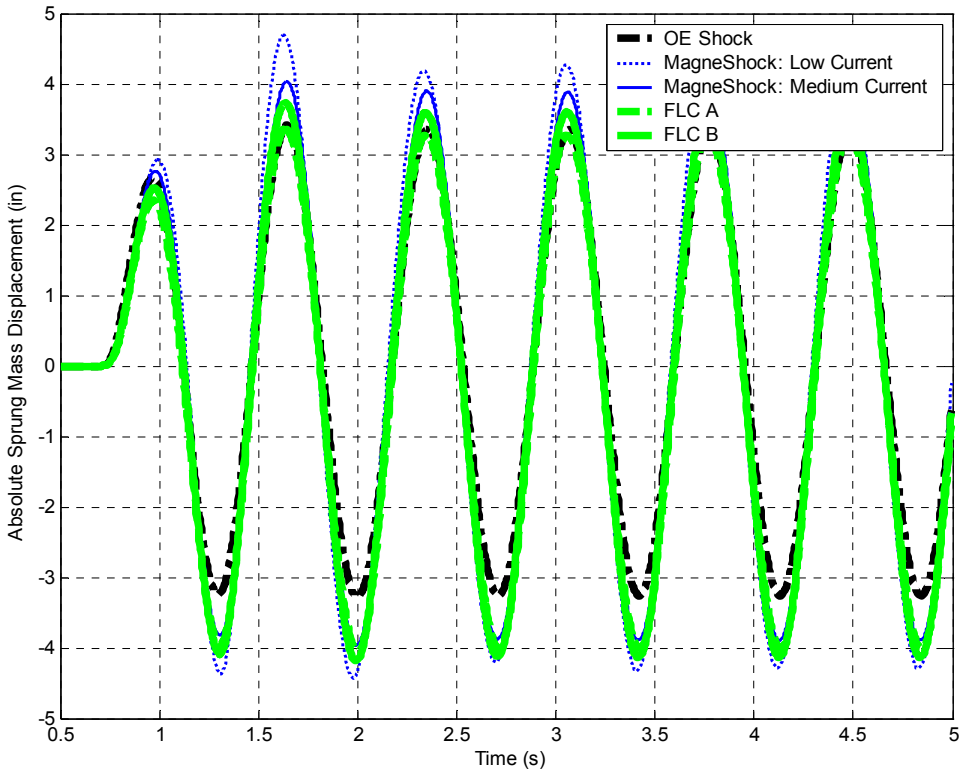

Figure 41. FLC performance evaluations: sprung mass response to a 2" amplitude sinusoid at 8 mph

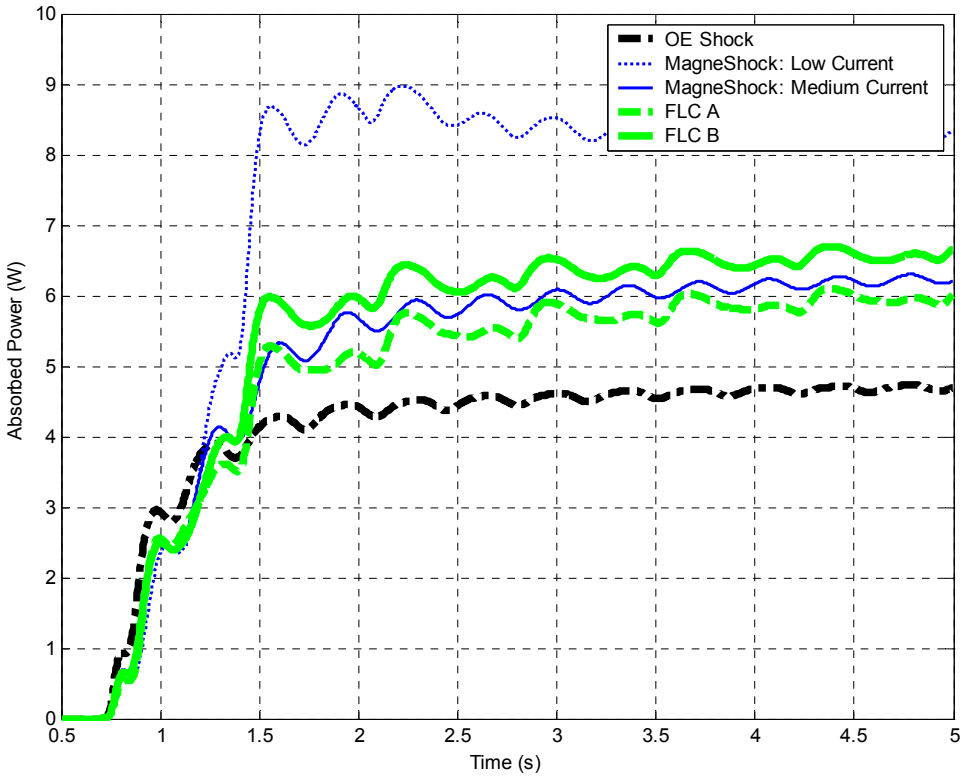

Figure 42. FLC performance evaluations: absorbed power for a 2" amplitude sinusoid at 8 mph

Table 11. Quarter Car Simulation Results: Sinusoidal Input, 8 mph, 100" wavelength, 2" amplitude

	OE Passive Shock	MagneShock™ Passive A (Low-Damping)	MagneShock™ Passive B (Medium Damping)	FLC MagneShock™ A	FLC MagneShock™ B
6 Watt Absorbed Power (W)*	4.7	9.0	6.3	6.1	6.7
RMS Sprung Mass Acceleration (G)	0.3583	0.4730	0.4280	0.3952	0.4205
RMS Suspension Travel (in)	0.7442	1.0955	0.9751	0.8723	0.9423
RMS Tire Normal Force (lb)	1242.20	1247.78	1245.60	1244.89	1245.67

*Approximate Maximum Value

5.3. Swept Sine Input

Figure 43 shows simulated sprung mass responses to a 1" amplitude, swept sine wave, from 0-20Hz for controlled and passive damping cases. Figure 44 shows the resulting absorbed power calculations for these step responses, and Table 12 summarizes the performance statistics.

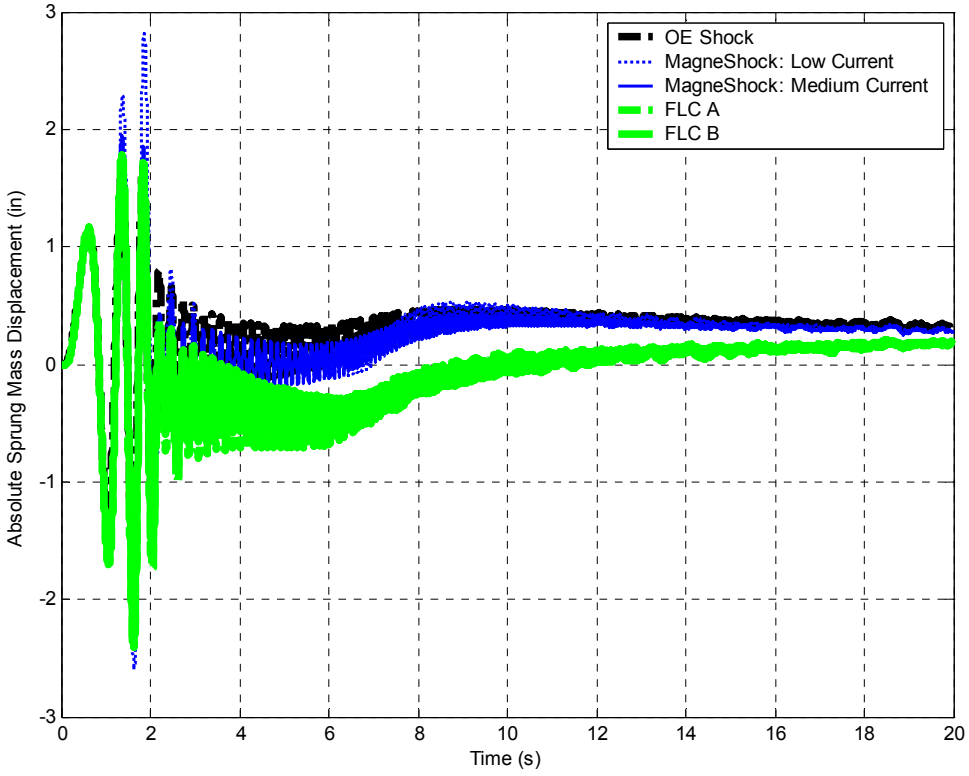

Figure 43. FLC performance evaluations: sprung mass response to a 1" swept sinusoid from 0-20Hz

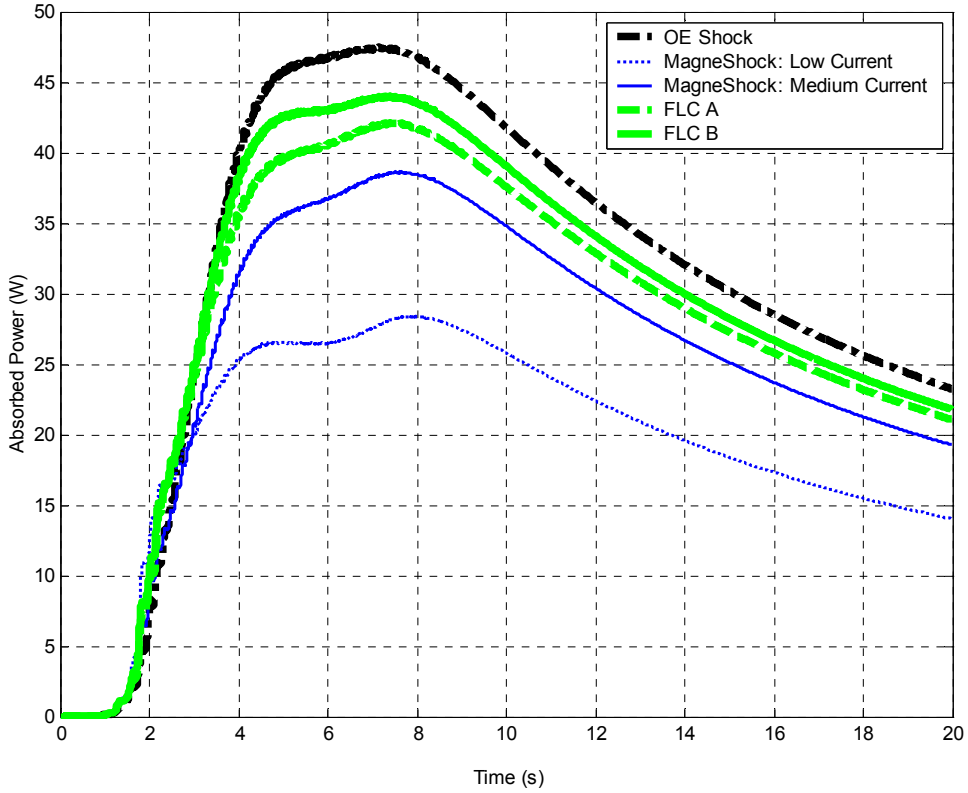

Figure 44. FLC performance evaluations: absorbed power for a 1" swept sinusoid from 0-20Hz

Table 12. Quarter Car Simulation Results: 0.001-15 Hz 2" Amplitude 20 Second Sine Sweep

	OE Passive Shock	MagneShock™ Passive A (Low-Damping)	MagneShock™ Passive B (Medium Damping)	FLC MagneShock™ A	FLC MagneShock™ B
6 Watt Absorbed Power (W)*	48	27	38	42	44
RMS Sprung Mass Acceleration (G)	0.6145	0.4516	0.5513	0.5975	0.5985
RMS Suspension Travel (in)	0.3794	0.4649	0.4120	0.4494	0.4583
RMS Tire Normal Force (lb)	1250.72	1251.30	1250.90	1250.55	1250.55

*Approximate Maximum Value

5.4. Speed Bump Excitation

Figure 45 shows simulated sprung mass responses to a speed bump terrain at 5 mph for controlled and passive damping cases. Figure 46 shows the resulting absorbed power calculations for these step responses, and Table 13 summarizes the performance statistics.

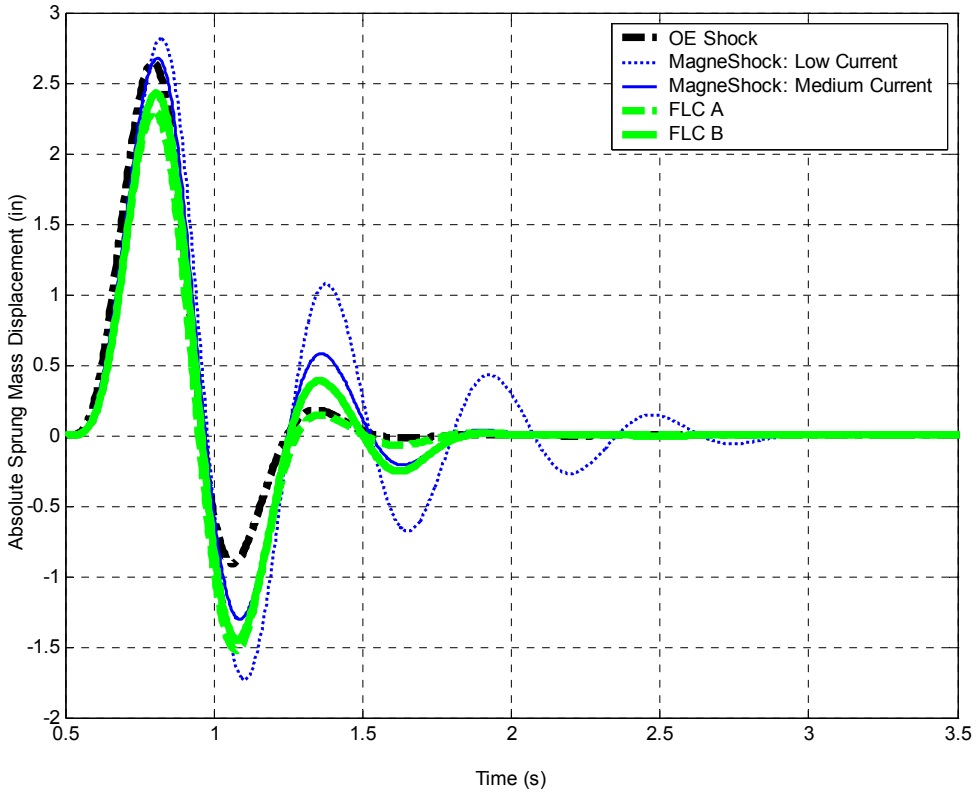

Figure 45. FLC performance evaluations: sprung mass response to 5 mph speed bump

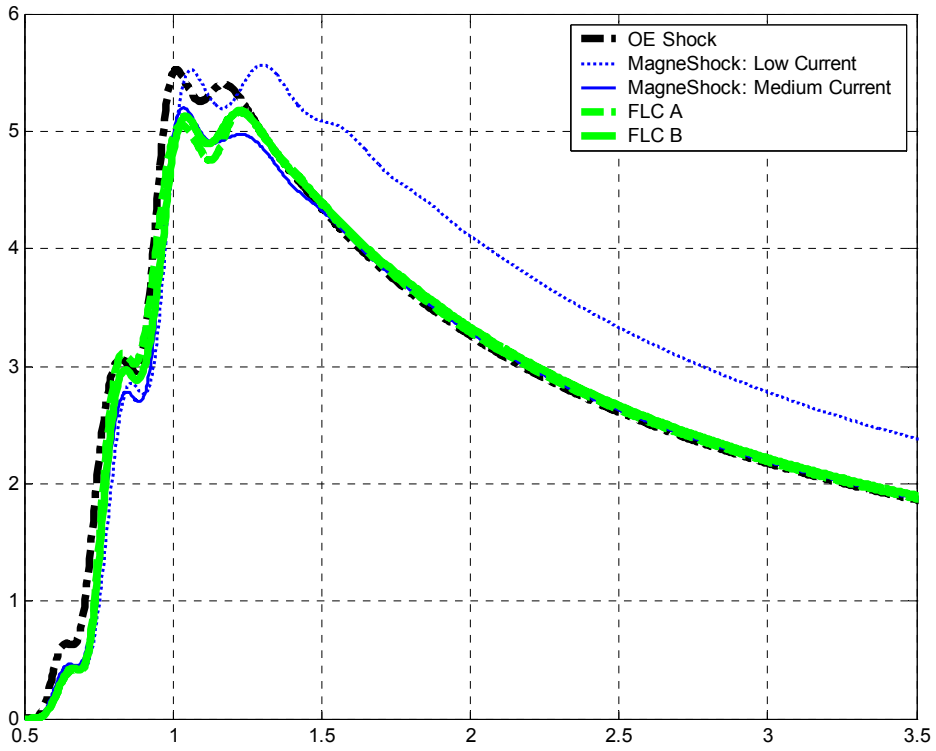

Figure 46. FLC performance evaluations: absorbed power for a 5 mph speed bump

Table 13. Quarter Car Simulation Results: Speed bump @ 5 mph

	OE Passive Shock	MagneShock™ Passive A (Low-Damping)	MagneShock™ Passive B (Medium Damping)	FLC MagneShock™ A	FLC MagneShock™ B
6 Watt Absorbed Power (W)*	5.52	5.56	5.20	5.18	5.17
RMS Sprung Mass Acceleration (G)	0.0603	0.1121	0.0796	0.0712	0.0774
RMS Suspension Travel (in)	0.1070	0.2564	0.1587	0.1369	0.1523
RMS Tire Normal Force (lb)	1225.00	1224.50	1225.00	1225.07	1225.04

*Approximate Maximum Value

Figure 47 shows simulated sprung mass responses to a speed bump terrain at 10 mph for controlled and passive damping cases. Figure 48 shows the resulting absorbed power calculations for these step responses, and Table 14 summarizes the performance statistics.

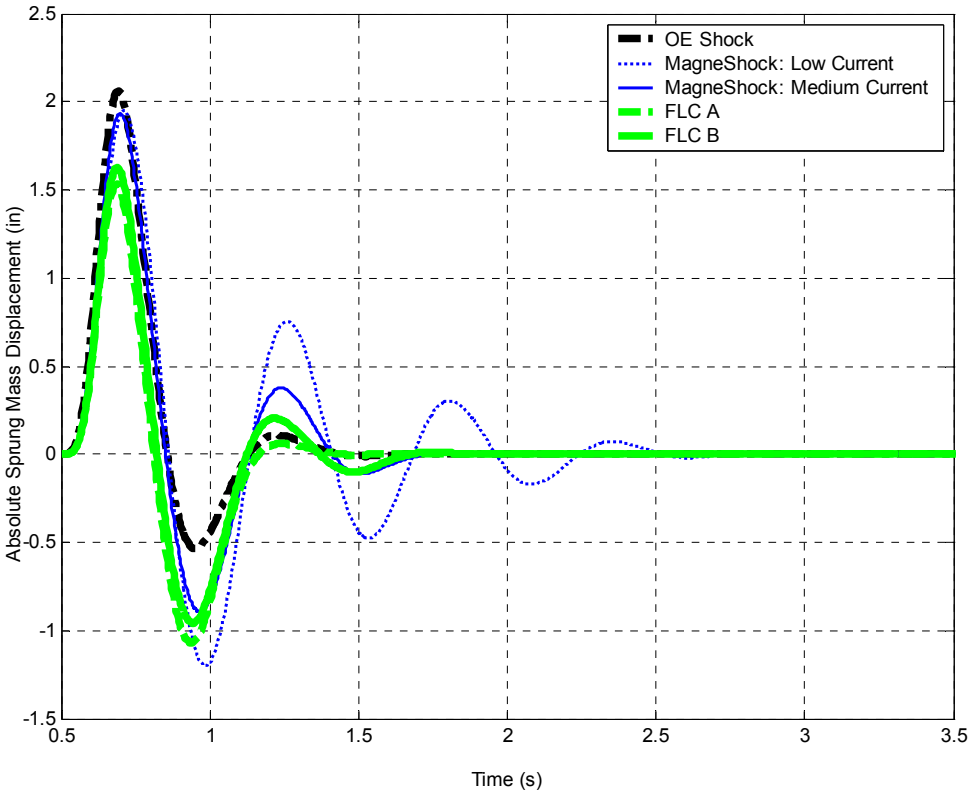

Figure 47. FLC performance evaluations: sprung mass response to 10 mph speed bump

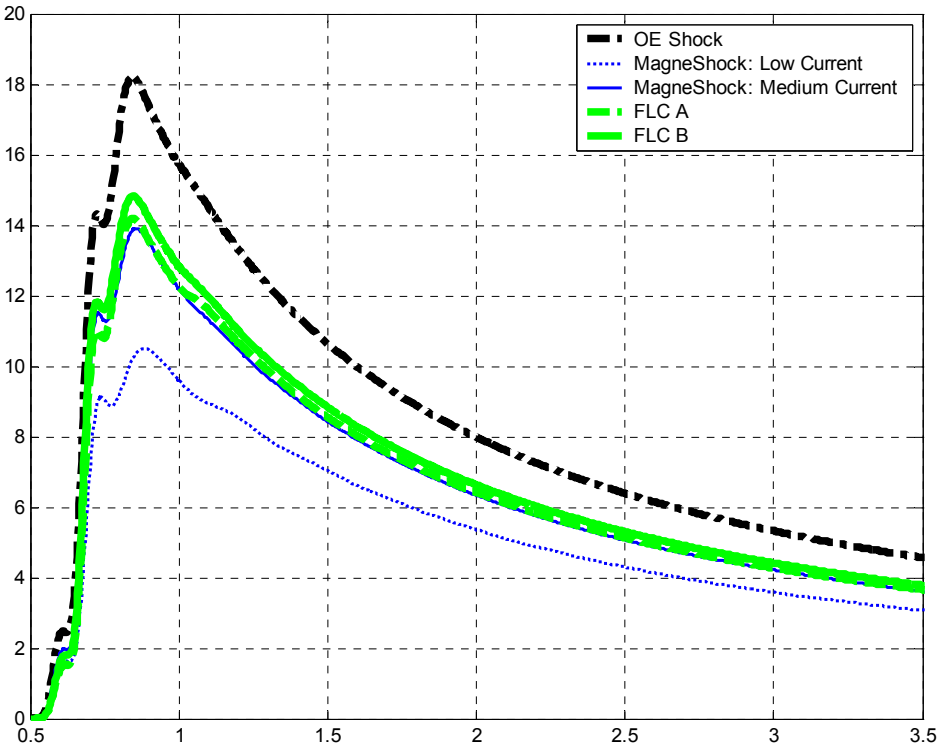

Figure 48. FLC performance evaluations: absorbed power for a 10 mph speed bump

Table 14. Quarter Car Simulation Results: Speed bump @ 10 mph

	OE Passive Shock	MagneShock™ Passive A (Low-Damping)	MagneShock™ Passive B (Medium Damping)	FLC MagneShock™ A	FLC MagneShock™ B
6 Watt Absorbed Power (W)*	18.2	10.4	13.9	14.2	14.9
RMS Sprung Mass Acceleration (G)	0.0533	0.0868	0.0665	0.0589	0.0624
RMS Suspension Travel (in)	0.0949	0.1918	0.1232	0.1045	0.1086
RMS Tire Normal Force (lb)	1226.54	1224.99	1225.47	1226.40	1226.66

*Approximate Maximum Value

Figure 49 shows simulated sprung mass responses to a speed bump terrain at 15 mph for controlled and passive damping cases. Figure 50 shows the resulting absorbed power calculations for these step responses, and Table 15 summarizes the performance statistics.

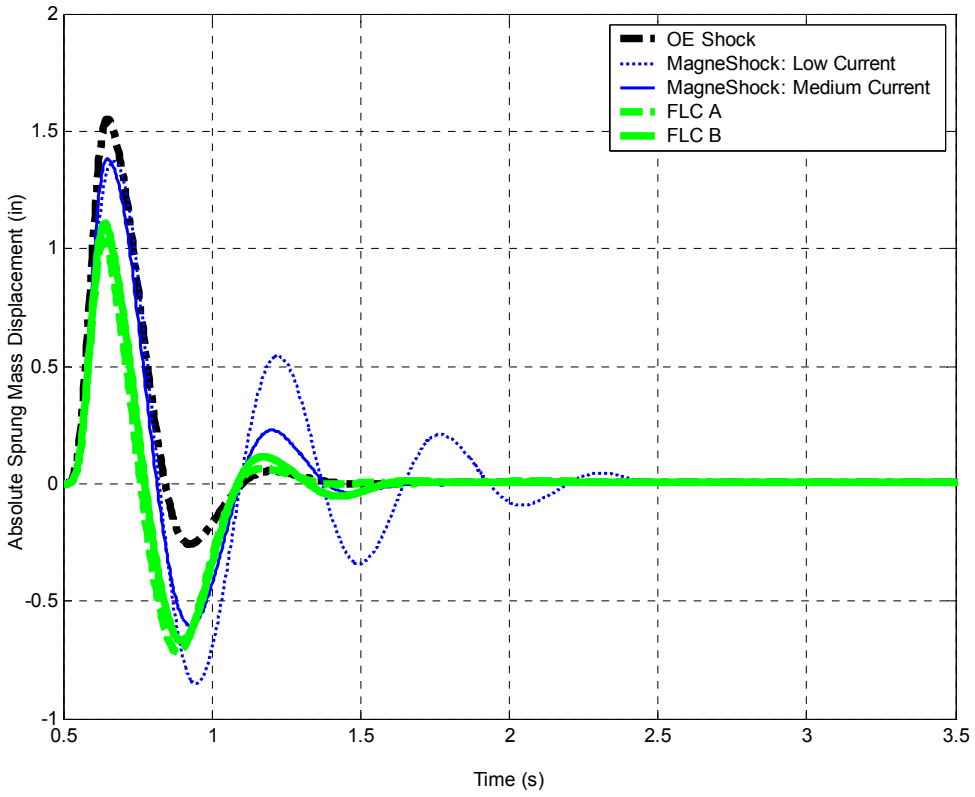

Figure 49. FLC performance evaluations: sprung mass response to 15 mph speed bump

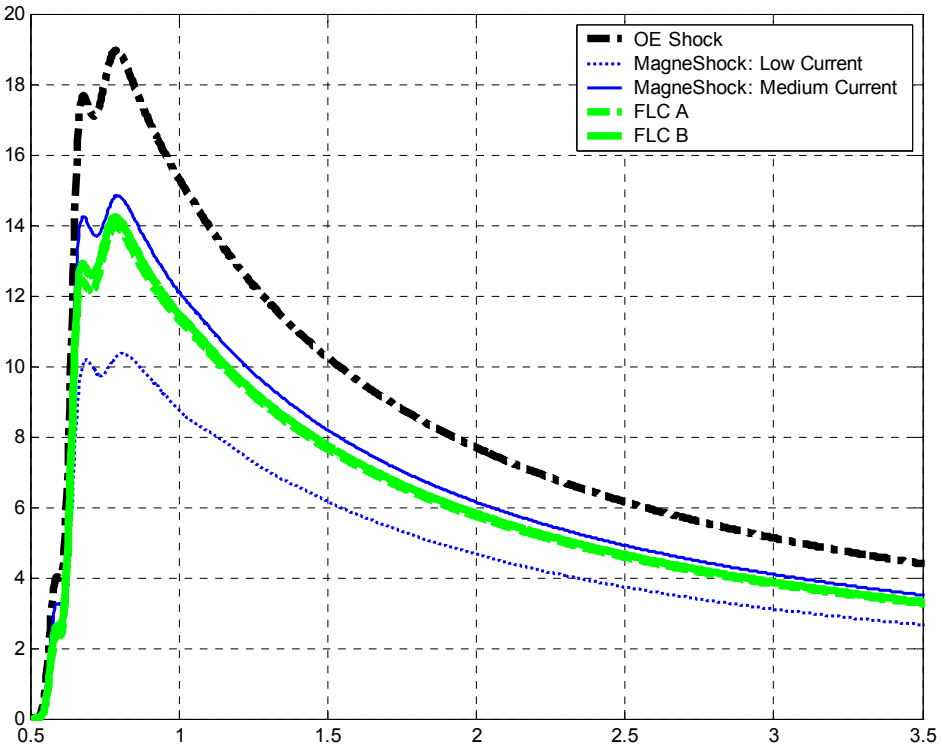

Figure 50. FLC performance evaluations: absorbed power for a 15 mph speed bump

Table 15. Quarter Car Simulation Results: Speed bump @ 15 mph

	OE Passive Shock	MagneShock™ Passive A (Low-Damping)	MagneShock™ Passive B (Medium Damping)	FLC MagneShock™ A	FLC MagneShock™ B
6 Watt Absorbed Power (W)*	19.0	10.3	14.9	14.0	14.2
RMS Sprung Mass Acceleration (G)	0.0437	0.0683	0.0545	0.0488	0.0500
RMS Suspension Travel (in)	0.0757	0.1427	0.0920	0.0768	0.0793
RMS Tire Normal Force (lb)	1228.20	1225.01	1227.34	1227.94	1228.00

*Approximate Maximum Value

Figure 51 shows simulated sprung mass responses to a speed bump terrain at 25 mph for controlled and passive damping cases. Figure 52 shows the resulting absorbed power calculations for these step responses, and Table 16 summarizes the performance statistics.

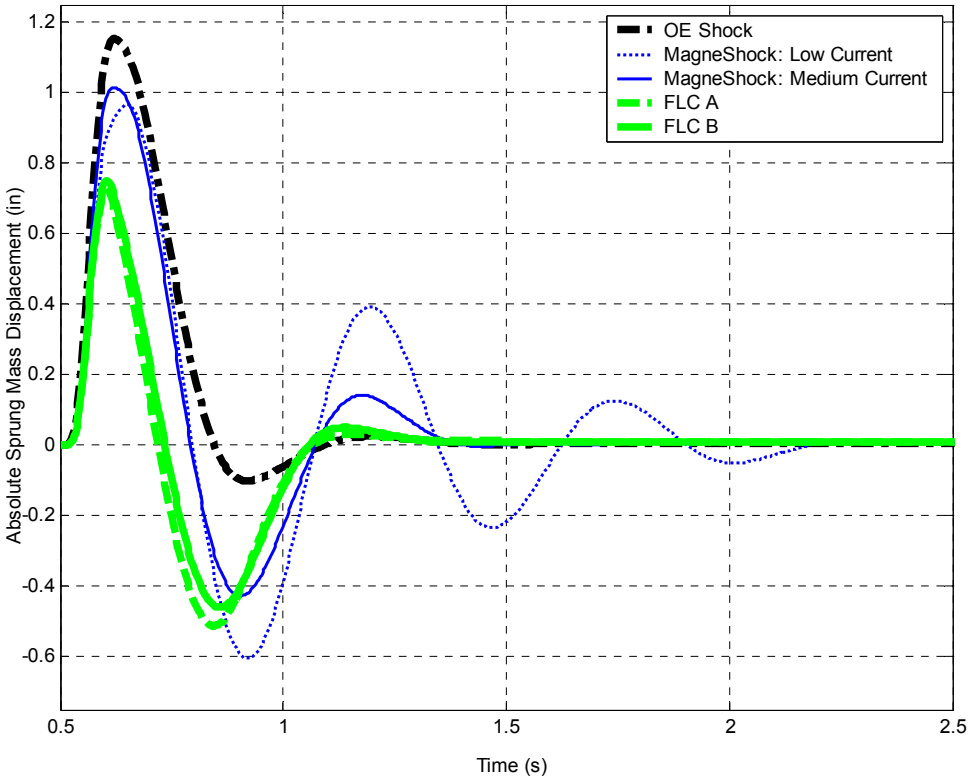

Figure 51. FLC performance evaluations: sprung mass response to 25 mph speed bump

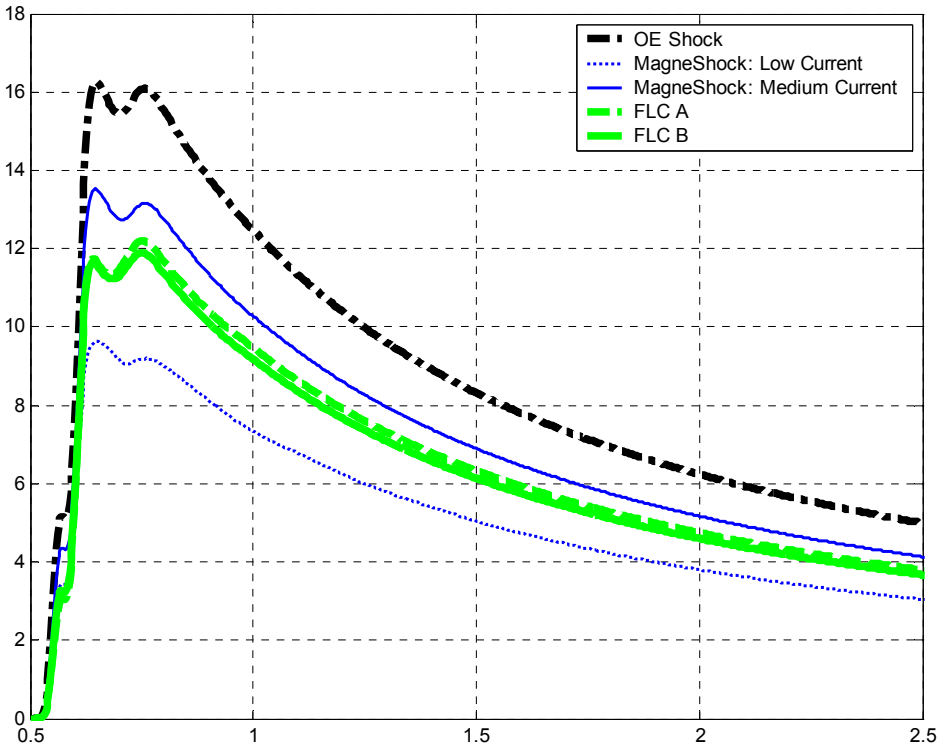

Figure 52. FLC performance evaluations: absorbed power for a 25 mph speed bump

Table 16. Quarter Car Simulation Results: Speed bump @ 25 mph

	OE Passive Shock	MagneShock™ Passive A (Low-Damping)	MagneShock™ Passive B (Medium Damping)	FLC MagneShock™ A	FLC MagneShock™ B
6 Watt Absorbed Power (W)*	16.2	9.6	13.5	12.2	11.9
RMS Sprung Mass Acceleration (G)	0.0366	0.0550	0.0471	0.0430	0.0420
RMS Suspension Travel (in)	0.0600	0.1050	0.0693	0.0584	0.0569
RMS Tire Normal Force (lb)	1228.51	1228.90	1228.64	1228.94	1228.87

*Approximate Maximum Value

5.5. Road Data Excitation

5.5.1. 30mph Evaluation

Figure 53 shows simulated sprung mass responses to measured road data at a speed of 30 mph for controlled and passive damping cases. Figure 54 shows the resulting absorbed power calculations for these step responses, and Table 17 summarizes the performance statistics.

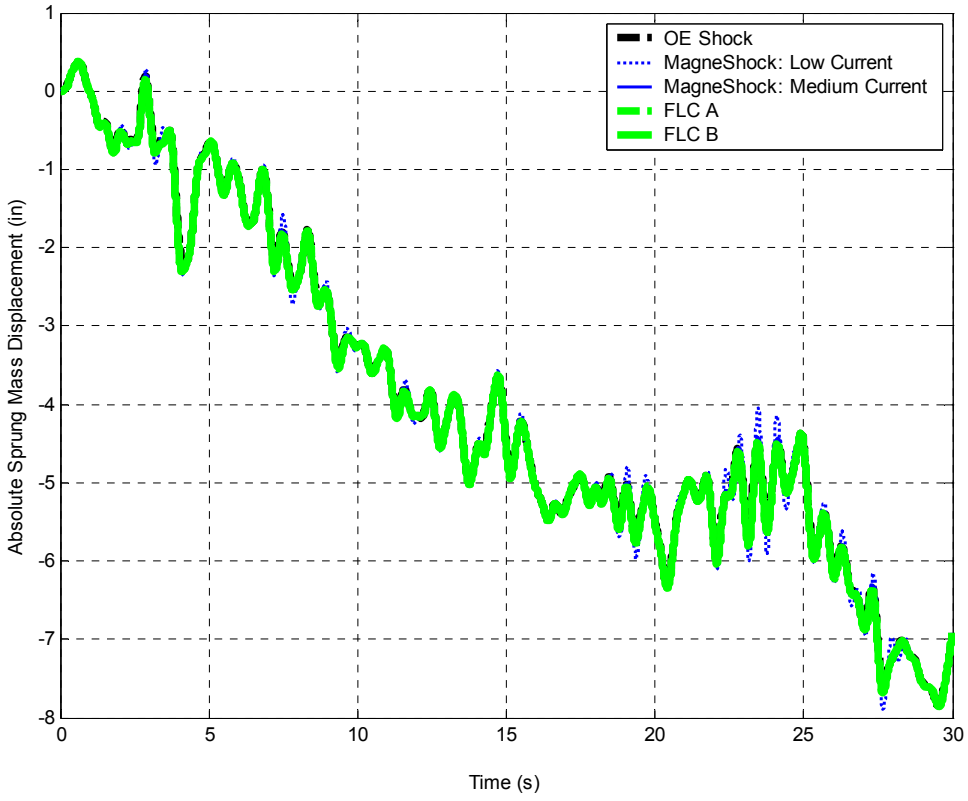

Figure 53. FLC performance evaluations: sprung mass response to road data at 30 mph

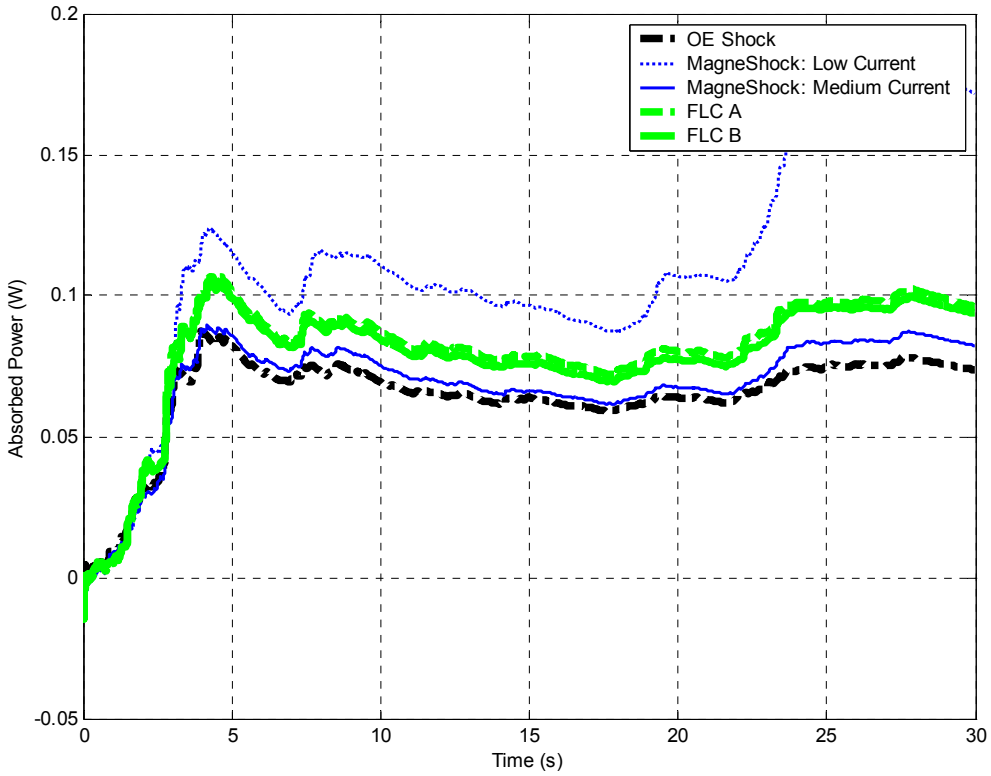

Figure 54. FLC performance evaluations: absorbed power for road data at 30 mph

Table 17. Quarter Car Simulation Results: 30 mph, Highway Road Data for 30 seconds

	OE Passive Shock	MagneShock™ Passive A (Low-Damping)	MagneShock™ Passive B (Medium Damping)	FLC MagneShock™ A	FLC MagneShock™ B
6 Watt Absorbed Power (W)*	0.075	0.173	0.084	0.097	0.095
RMS Sprung Mass Acceleration (G)	0.0349	0.0524	0.0366	0.0384	0.0383
RMS Suspension Travel (in)	0.0607	0.1227	0.0685	0.0797	0.0790
RMS Tire Normal Force (lb)	1223.38	1223.35	1223.39	1223.35	1223.37

*Approximate Final Value at 30 seconds

5.5.2. 60mph Evaluation

Figure 55 shows simulated sprung mass responses to measured road data at a speed of 60 mph for controlled and passive damping cases. Figure 56 shows the resulting absorbed power calculations for these step responses, and Table 18 summarizes the performance statistics.

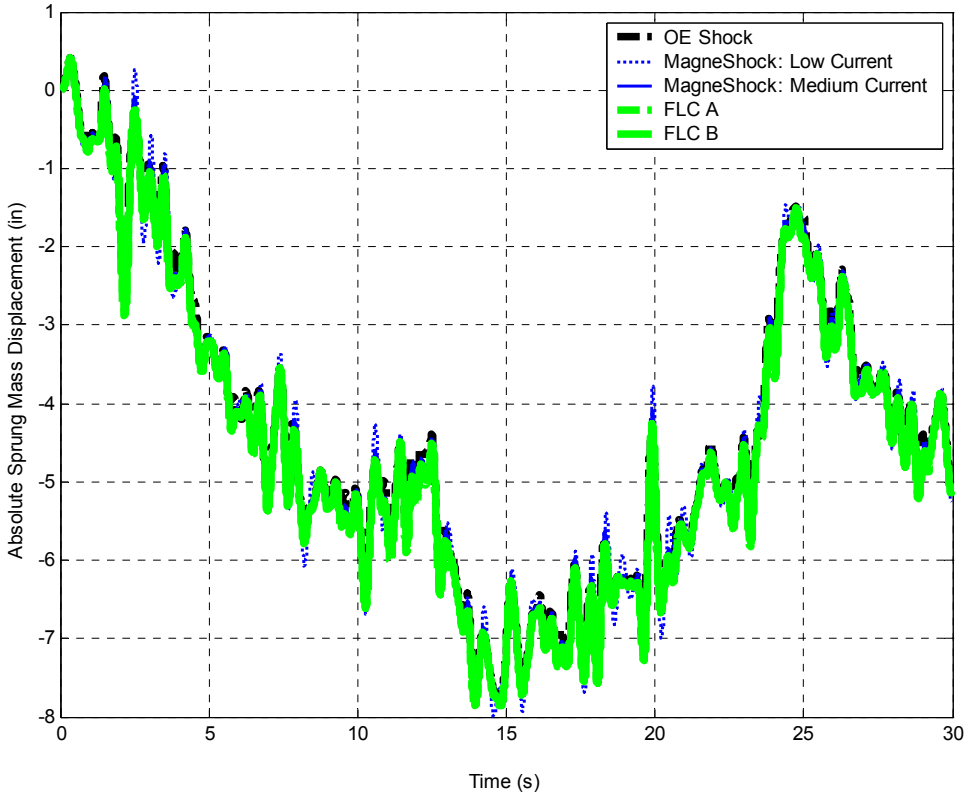

Figure 55. FLC performance evaluations: sprung mass response to road data at 60 mph

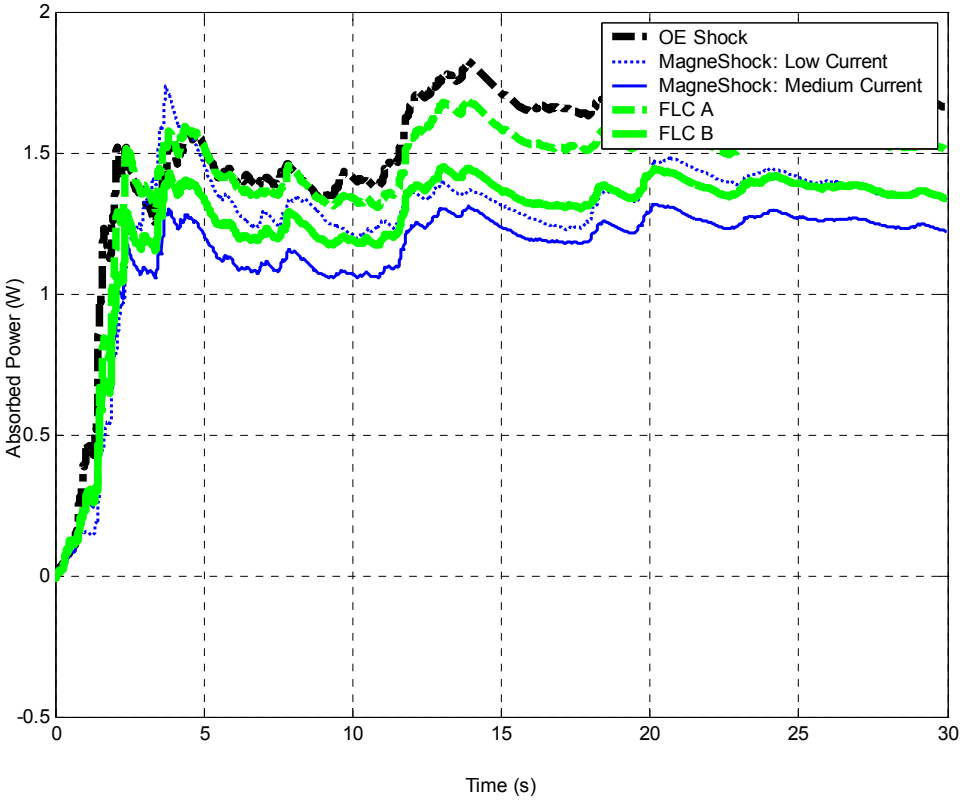

Figure 56. FLC performance evaluations: absorbed power for road data at 60 mph

Table 18. Quarter Car Simulation Results: 60 mph, Highway Road Data for 30 seconds

	OE Passive Shock	MagneShock™ Passive A (Low-Damping)	MagneShock™ Passive B (Medium Damping)	FLC MagneShock™ A	FLC MagneShock™ B
6 Watt Absorbed Power (W)*	1.82	1.40	1.30	1.69	1.44
RMS Sprung Mass Acceleration (G)	0.1027	0.1188	0.1009	0.1034	0.1038
RMS Suspension Travel (in)	0.1372	0.2755	0.1956	0.1952	0.2063
RMS Tire Normal Force (lb)	1223.70	1223.74	1223.72	1223.75	1223.76

*Approximate Value at 14 seconds

5.5.3. 90mph Evaluation

Figure 57 shows simulated sprung mass responses to measured road data at a speed of 90 mph for controlled and passive damping cases. Figure 58 shows the resulting absorbed power calculations for these step responses, and Table 19 summarizes the performance statistics.

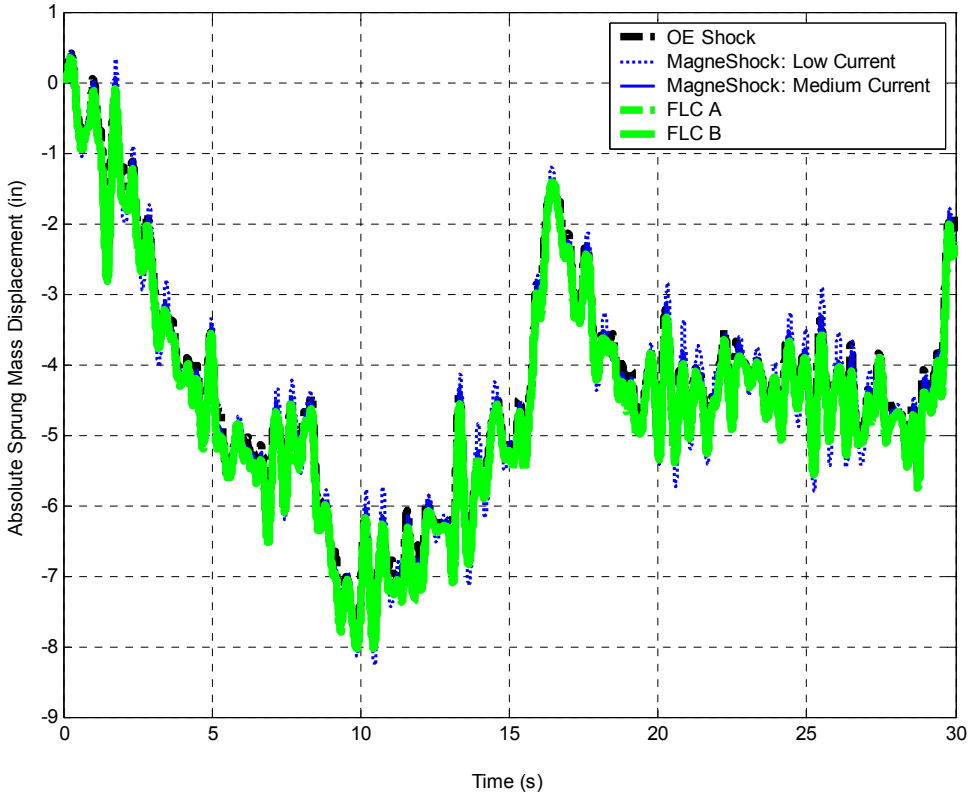

Figure 57. FLC performance evaluations: sprung mass response to road data at 90 mph

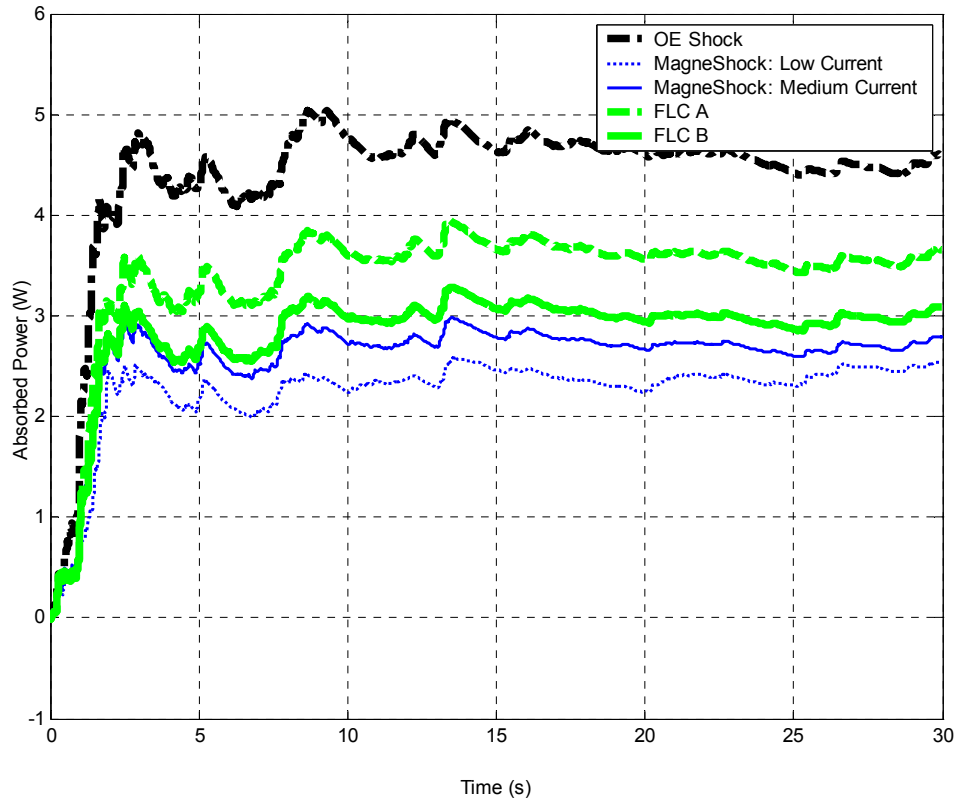

Figure 58. FLC performance evaluations: absorbed power for road data at 90 mph

Table 19. Quarter Car Simulation Results: 90 mph, Highway Road Data for 23 seconds

	OE Passive Shock	MagneShock™ Passive A (Low-Damping)	MagneShock™ Passive B (Medium Damping)	FLC MagneShock™ A	FLC MagneShock™ B
6 Watt Absorbed Power (W)*	5.0	2.4	2.9	3.8	3.2
RMS Sprung Mass Acceleration (G)	0.1517	0.1545	0.1370	0.1426	0.1392
RMS Suspension Travel (in)	0.1988	0.3527	0.2627	0.2620	0.2690
RMS Tire Normal Force (lb)	1225.34	1224.85	1225.10	1225.27	1225.10

*Approximatel Value at 8.6 seconds

5.6. Summary of Simulated System

Passive and semi-active control simulations were performed for identical road inputs and compared. As shown in the previous figures, the use of fuzzy logic usually resulted in a vast improvement of ride quality (6 Watt Absorbed Power Criterion) over the OE shocks (26% reduction), but performed comparably with the fixed-current MagneShock™ on its lowest current level. However, the fixed-current MagneShock™ required much higher suspension deflection to achieve similar ride quality (40% greater than the FLC B). Additionally, the FLC B also revealed the lowest average RMS sprung-mass acceleration of the inputs tested.

6. FLC Performance Evaluations: Experimental Results

To experimentally validate the ride quality benefits of fuzzy logic controlled MagneShocks™ over passive shocks, a vehicle was equipped and instrumented for field testing. Due to budgetary limitations, test vehicle choices were limited to those that were available for modifications and hardware installation. The vehicle of choice was a 1973 Toyota Land Cruiser FJ-55 model, to which the semi-active suspension system was installed on the front end only (Figure 59). Although quite old, the suspension technology utilized on the Land Cruiser is still used for the rear suspensions on most domestic SUVs and light trucks. Also, the sprung and unsprung masses are similar to those seen in modern SUVs and light trucks.

6.1. Vehicle Implementation

The front suspension of the test vehicle required no major modifications for the implementation of the semi-active control. The suspension utilizes a solid axle mounted on top of a 7-leaf spring-pack, with the hanger shackle located at the front of the spring (also known as a Hotchkiss suspension [16]). The shocks (both OE and MagneShocks™) were mounted in line with the wheel motion, and were considered as a 1:1 spring position/shock position ratio, in the stock, unmodified location. New polyurethane bushings were installed at all spring mounts. No front sway bar was used, although the rear suspension does incorporate a sway bar for roll control.

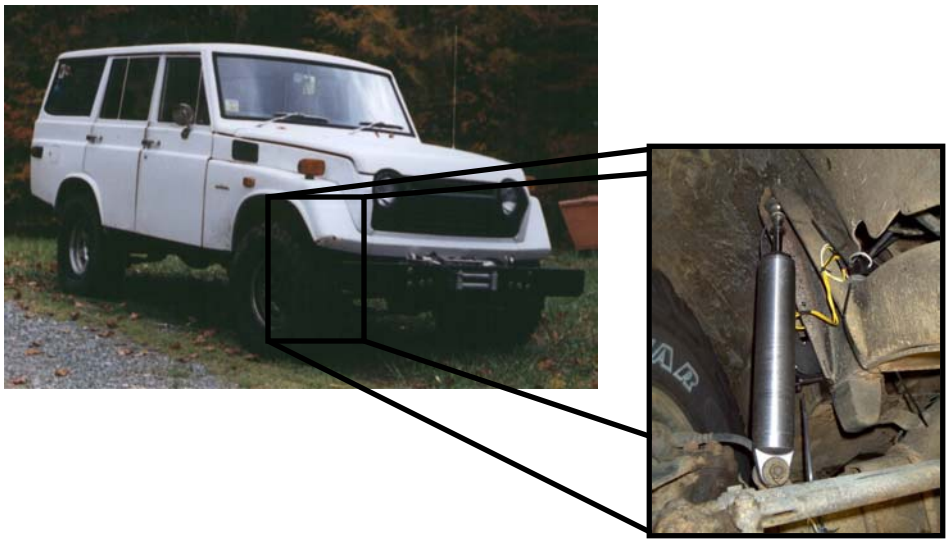

Figure 59. Experimental test vehicle and suspension setup

The Carrera MagneShocks™ were easy to install in place of the OE shocks due to their similarities. Carrera's products are generally manufactured for racing applications, so they come equipped with spherical bearings. However, in this application, the bearings were replaced with OE style stud mounts for the upper attachments and bushings for the lower attachments. With these modifications, the shocks bolted directly to the vehicle. Next, the shocks were wired for electromagnetic excitation. A manually adjustable control box was installed so that the driver could select fixed (passive) damping values for each shock. For real-time control, a dSPACE™ 1102 control board was installed. Additionally, a custom 2-channel, 8000 Hz pulse width modulating (PWM) amplifier was installed to power the electromagnets.

Figure 60. Unsprung mass accelerometer (note leaf-spring pack in background)

For this research, linear potentiometers were used to measure the suspension travel. From these displacement sensors, suspension velocity and acceleration were calculated. Unimeasure JX-PA models were mounted on the vehicle frame very close to the shocks, such that relative displacements in the suspension and sensor would be equivalent. Magnostrictive sensors are contained within newer versions of MagneShocks™, but were not available at the time of this testing. These sensors have superior performance capabilities and are internal to the shock, making for very straightforward installation and providing protection from the elements (rain, road debris, ice, etc.).

Vehicle ride quality was assessed using four Crossbow™ LP Series capacitive accelerometers. Two accelerometers were mounted on each side of the vehicle. +/- 10G accelerometers were mounted to the unsprung mass (on each side of the axle, directly below the shock mounts). +/- 4G accelerometers were mounted to the vehicle frame (beside each upper shock mount). These accelerometers can be seen in Figure 59 and Figure 60.

The dSPACE™ 1102 control system enabled real-time control at 1000 Hz. Raw data from the potentiometers and accelerometers was sampled at 1000 Hz, the FLC control law was updated, and control voltages were output to the current amplifier.

6.2. Experimental Results

Testing was conducted for a variety of terrains and operating conditions. The results reported here were taken on a public city street, chosen for its exceptionally poor road condition (Figure 61). Vehicle speed was maintained at 45 mph, the posted speed limit. The street contained many asphalt patches, bridge abutments, expansion joints, raised manhole covers, and potholes. Multiple trials were conducted under these conditions to ensure repeatability of the test results.

Figure 61. Typical examples of the test road

Ride quality (quantified using the 6 Watt Absorbed Power and RMS sprung-mass acceleration) associated with an OE passive shock was compared to that of MagneShocks™ with low to moderate fixed coil currents. As expected from computer simulations, the OE shocks yielded the worst ride quality of all passive shocks tested (Figure 63, Figure 65, Figure 67, and Figure 69). The ride quality associated with fixed-current MagneShocks™ depended significantly on the current level selected and road conditions. For low damping levels, the MagneShocks™ provided a 26% reduction in absorbed power compared to OE passive shocks (Table 20 and Figure 63). Data collected at high current levels (not shown) revealed significant declines in ride quality, as unsprung mass accelerations decreased at the expense

of the sprung mass accelerations. With the shock damping set to extremely high levels, the tire dynamics dominated the response, resulting in a highly underdamped system.

Vehicle ride quality was significantly improved with the fuzzy logic controlled semi-active suspension (Figure 63, Figure 65, Figure 67, and Figure 69). Contrary to computer simulation results, the FLC B algorithm outperformed the passive MagneShock™ for absorbed power, albeit marginally (see Section 4 for control algorithm descriptions). Additionally, the RMS sprung mass acceleration decreased by approximately 8% for the FLC B algorithm as compared with either the OE shock or fixed-current MagneShock™ (but at the expense of greater suspension deflection, as shown in Table 20, Table 21, Table 22, and Table 23).

Figure 62 shows the left front suspension position for the Road A input (Capital Blvd North) at a vehicle speed of 45 mph. Absorbed power was also calculated and presented in Figure 63. Finally, the tabulated results of vehicle ride are presented in Table 20.

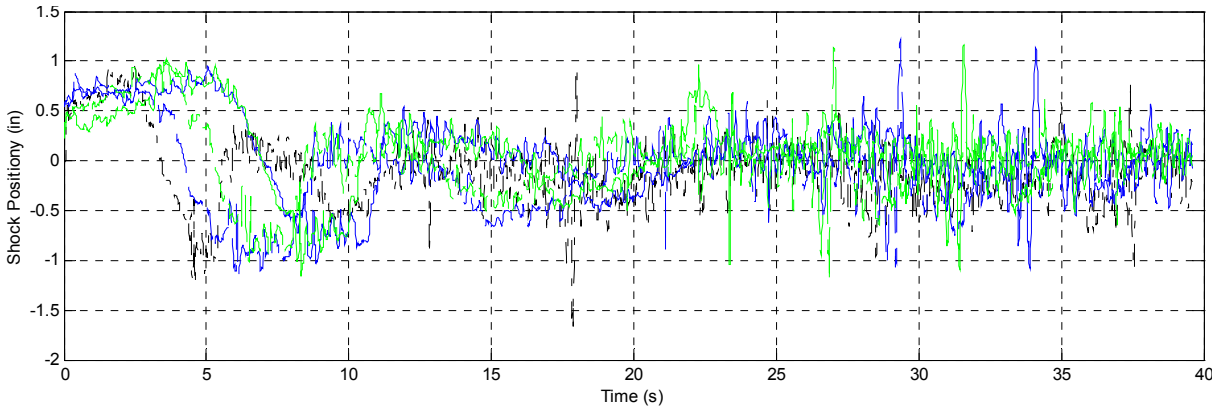

Figure 62. Suspension Position, Road A: 45 mph, 35 seconds (Left Front Suspension)

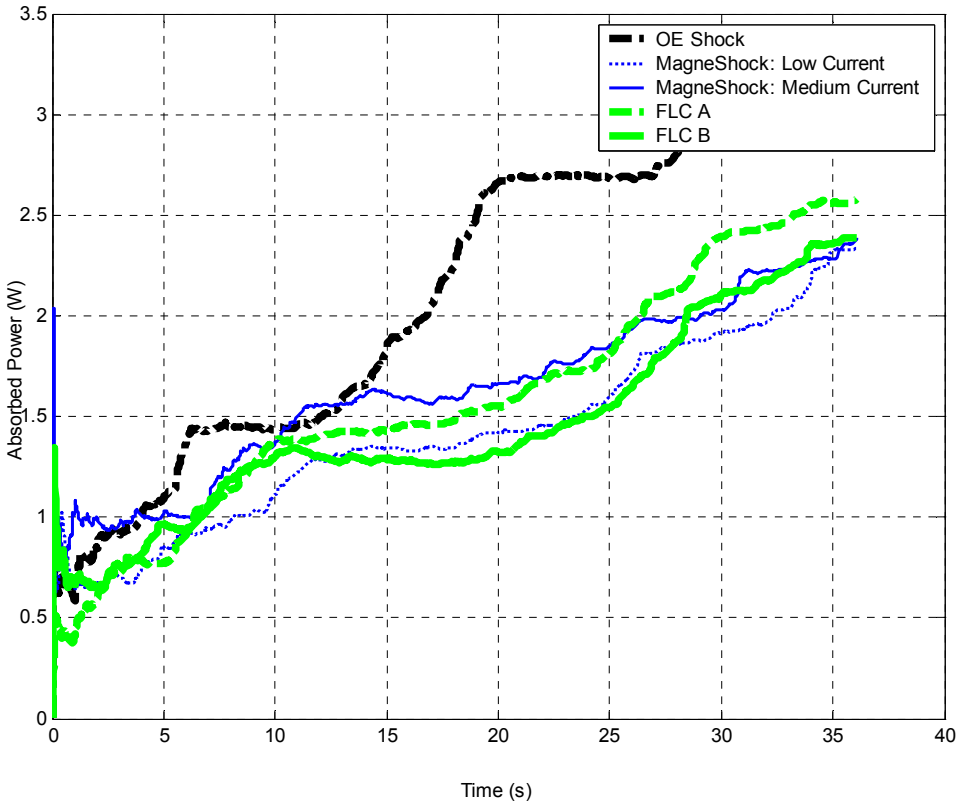

Figure 63. Absorbed Power, Road A: 45 mph, 35 seconds (Left Front Suspension)

Table 20. Experimental Results, Road A: 45 mph, 40 seconds (Left Front Suspension).

	OEM Passive Shock	MagneShock™ Passive A (Low-Damping)	MagneShock™ Passive B (Medium Damping)	FLC MagneShock™ A	FLC MagneShock™ B
6 Watt Absorbed Power (W) *	3.10	2.32	2.36	2.39	2.57
RMS Sprung Mass Acceleration (G)	0.1925	0.1910	0.1929	0.1883	0.1813
RMS Suspension Travel (in)	1.7540	1.9399	1.9881	1.9233	2.0001

*Approximate Final Value at 36 seconds

Figure 64 shows the right front suspension position for the Road A input (Capital Blvd North) at a vehicle speed of 45 mph. Again, absorbed power was also calculated and presented in Figure 65. Finally, the tabulated results of vehicle ride are presented in Table 21.

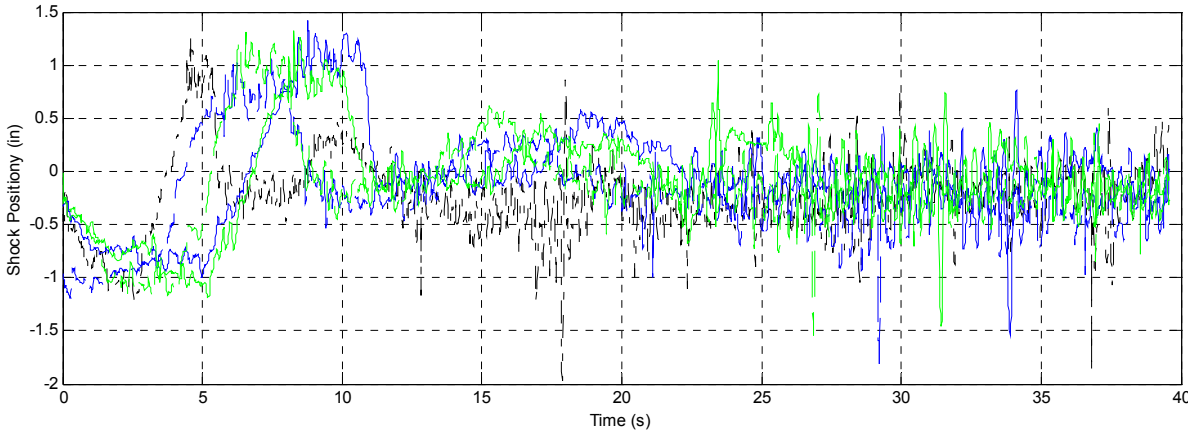

Figure 64. Suspension Position, Road A: 45 mph, 35 seconds (Right Front Suspension)

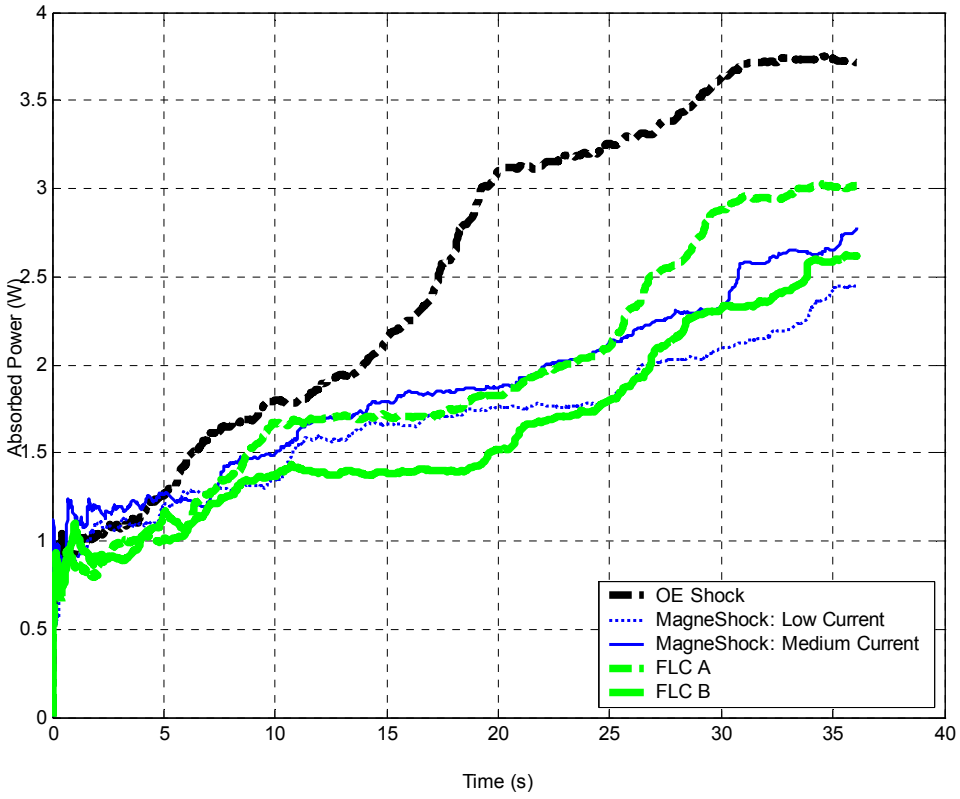

Figure 65. Absorbed Power, Road A: 45 mph, 35 seconds (Right Front Suspension)

Table 21. Experimental Results, Road A: 45 mph, 40 seconds (Right Front Suspension).

	OEM Passive Shock	MagneShock™ Passive A (Low-Damping)	MagneShock™ Passive B (Medium Damping)	FLC MagneShock™ A	FLC MagneShock™ B

6 Watt Absorbed Power (W) *	3.51	2.45	2.76	3.00	2.62
RMS Sprung Mass Acceleration (G)	0.2110	0.1786	0.1816	0.1819	0.1942
RMS Suspension Travel (in)	1.9305	2.0115	2.0723	2.0185	2.0920

*Approximate Value at 36 seconds

Figure 66 shows the left front suspension position for the Road B input (Capital Blvd Southbound) at a vehicle speed of 45 mph. Again, absorbed power was also calculated and presented in Figure 67. Finally, the tabulated results of vehicle ride are presented in Table 22.

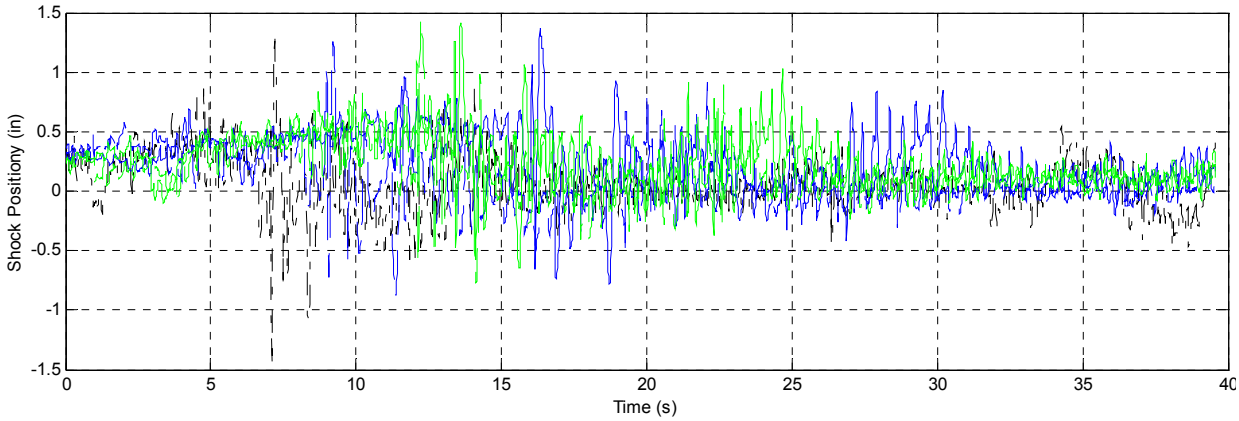

Figure 66. Suspension Position, Road B: 45 mph, 35 seconds (Left Front Suspension)

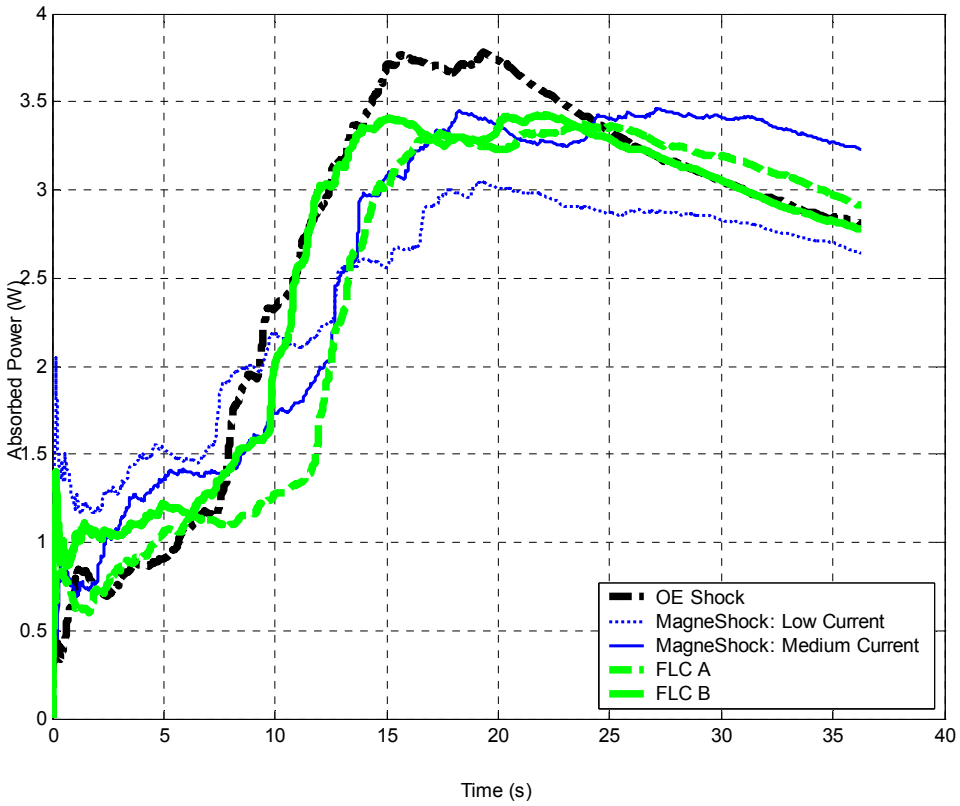

Figure 67. Absorbed Power, Road B: 45 mph, 35 seconds (Left Front Suspension)

Table 22. Table 20. Experiment Results, Road B: 45 mph for 35 seconds (Left Front Suspension)

	OEM Passive Shock	MagneShock™ Passive A (Low-Damping)	MagneShock™ Passive B (Medium Damping)	FLC MagneShock™ A	FLC MagneShock™ B
6 Watt Absorbed Power (W)*	3.68	3.00	3.33	3.31	3.27
RMS Sprung Mass Acceleration (G)	0.1785	0.1905	0.2025	0.1861	0.1851
RMS Suspension Travel (in)	1.9619	2.0844	2.1507	2.0702	2.1434

*Value at 17.5 seconds

Again, Figure 68 shows the right front suspension position for the Road B input (Capital Blvd Southbound) at a vehicle speed of 45 mph. Again, absorbed power was also calculated and

presented in Figure 69. Finally, the tabulated results of vehicle ride are presented in Table 23.

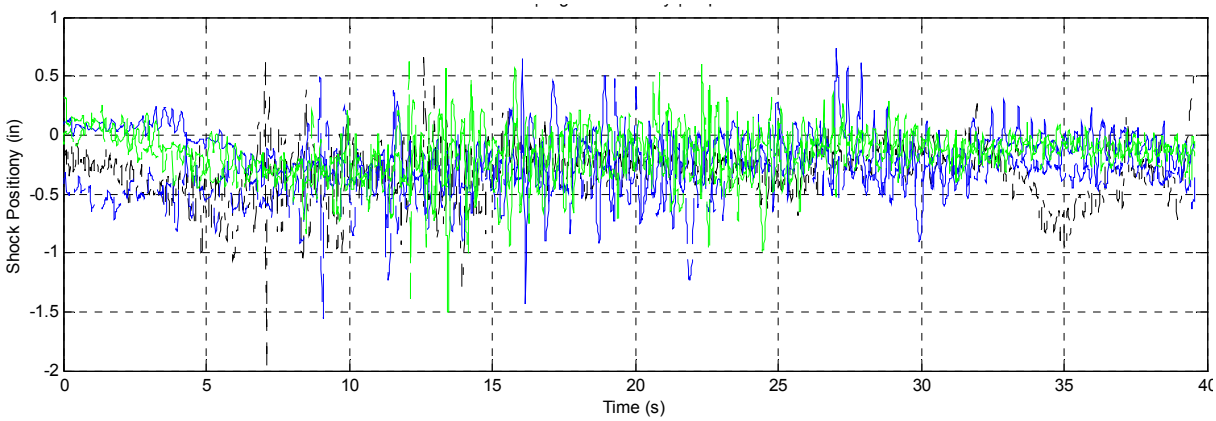

Figure 68. Suspension Position, Road B: 45 mph, 35 seconds (Right Front Suspension)

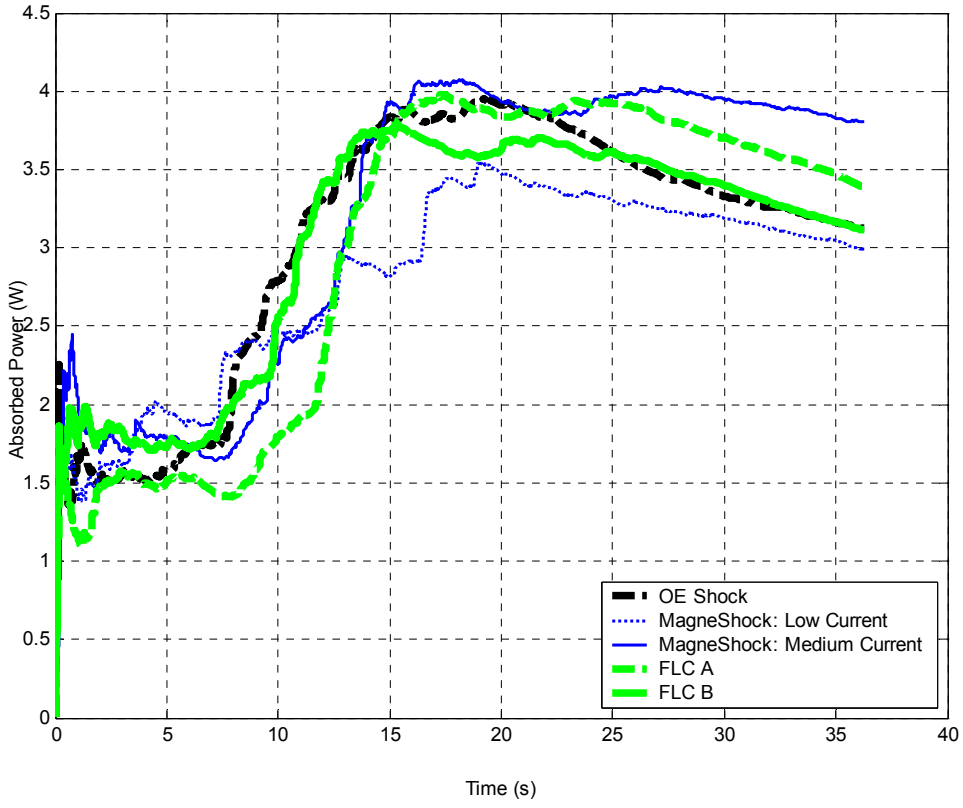

Figure 69. Absorbed Power, Road B: 45 mph, 35 seconds (Right Front Suspension)

Table 23. Experiment Results, Road B: 45 mph for 35 seconds (Right Front Suspension)

	OEM Passive Shock	MagneShock™ Passive A (Low-Damping)	MagneShock™ Passive B (Medium Damping)	FLC MagneShock™ A	FLC MagneShock™ B
6 Watt Absorbed Power (W)*	3.87	3.40	4.07	3.98	3.64
RMS Sprung Mass Acceleration (G)	0.2087	0.1908	0.2054	0.1900	0.1950
RMS Suspension Travel (in)	1.8473	1.8910	1.9763	1.9616	2.0074

* Value at 17.5 seconds

Despite the improvements in ride quality and handling performance achieved through fuzzy logic control, these algorithms did not significantly affect the excitation power requirements. Figure 70 shows typical power usage during one of the experimental FLC evaluations. Over the terrain tested, each MagneShock™ required an average of 0.0784 watts, which corresponds to an average current usage of less than 54 mA per shock (17.6% of the maximum rated power).

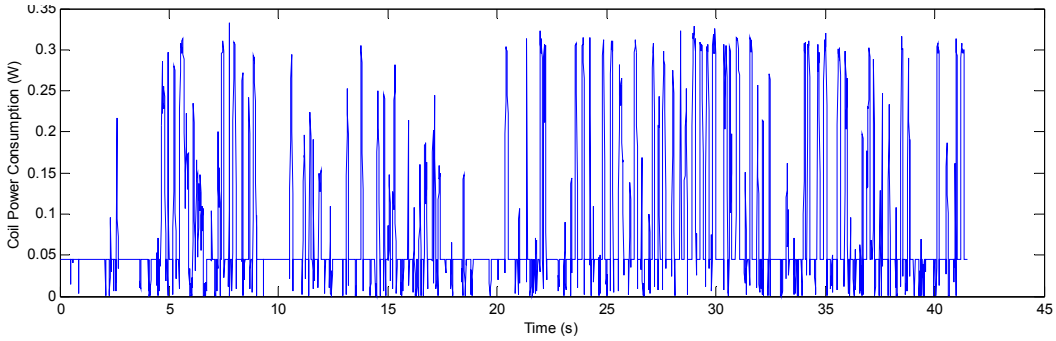

Figure 70. Electromagnetic coil power requirements for experimentally tested input

7. Conclusions

This paper outlines the benefits of implementing real-time, fuzzy logic control (FLC) to a commercially available magnetorheological (MR) shock absorber, the Carrera MagneShock™. The MagneShock™ utilizes an electromagnet to change the viscosity of MR fluid, enabling real-time control of the shock's damping characteristics. Using a fuzzy logic control algorithm, designed using the expertise of shock designers from the racing industry, significant gains were made in vehicle performance, most notably ride quality. Experimental and simulation results include 25% reductions in sprung mass absorbed power (U.S. Army 6 Watt Absorbed Power Criterion) as compared with typical passive shock absorbers over urban terrains. RMS sprung mass accelerations were also reduced by as much as 9%. Suspension travel typically increased with the use of the fuzzy logic control, as is generally the case with active and semi-active control algorithms. Additionally, a slight degradation in RMS tire normal force was documented with most computer simulations, though this degradation was typically no more than 0.5%. Although FLC absorbed power was comparable to that of passive (fixed low-current) MagneShock™ damping, the FLC still yielded additional 2-9% reductions in RMS sprung mass accelerations.

Experimental and simulation results indicate that the FLC B algorithm, which incorporated three membership functions (suspension displacement, velocity, and acceleration), out-performed the FLC A algorithm that used only two membership functions (suspension displacement and velocity). Possible means for improving the performance of this semi-active suspension include reducing the suspension spring stiffness, increasing the dynamic damping range of the MagneShock™, accounting for pitch and roll dynamics, and altering damping based on excitation frequency.

8. References

1. AL-Holou, N., S. J. Dae, and A. Shaout, "The Development of Fuzzy Logic Based Controller for Semi-Active Suspension System," Proc. of the 37th Midwest Symposium on Circuits and Systems, Vol. 2, p. 1373-1376, 1994.
2. Barak, P. and D. Hrovat, "Application of the LQG approach to design of an automotive suspension for three-dimensional vehicle models," in Advanced Suspensions, Proc. of Institution of Mechanical Engineers, pp. 11-26, Mechanical Engineering Publications Limited, London, 1988.
3. Barr, A.J. and J.L. Ray, "Control of an Active Suspension Using Fuzzy Logic," Proc. of 5th IEEE Intl Conference on Fuzzy Systems, Vol. 1, pp.42-48, IEEE, 1996.
4. Beale, M. and H. Demuth. Fuzzy Systems Toolbox: For Use With MATLAB: PWS Publishing Co. Boston, 1994.
5. Buckner, Greg D. Design of Electromechanical Systems (lecture). MAE 589N, North Carolina State University. Fall 2001.
6. Buckner, Greg D., K. T. Schuetze, and J. H. Beno, "Active Vehicle Suspension Control Using Intelligent Feedback Linearization," in Proc. of American Control Conference, pp. 4014-4018, Chicago, June 2000.
7. Busshardt, J. and R. Isermann. "Adaptive and semi-active shock absorbers based on real-time parameter estimation." Technical Papers: Total Vehicle Dynamics Vol. 2. XXIV FISITA Congress. Mechanical Engineering Publications Limited for the Institution of Mechanical Engineers. London, 1992. pp129-135
8. J.D.Carlson, D.N.Catanzarite and K.A.St Clair, "Commercial Magneto-Rheological Fluid Devices," Proceedings 5th Int. Conf. on ER Fluids, MR Suspensions and Associated Technology, W. Bullough, Ed., World Scientific, Singapore (1996) 20-28.
9. Carlson et al, United States Patent #5277281, Magnetorheological Fluid Devices, Jan. 11, 1994.
10. Carlson, J. D., "What Makes a Good MR Fluid?," 8th International Conference on ER Fluids and MR Fluids Suspensions, Nice, July 9 - 13, 2001.
11. Chandrupatla, Tirupathi R. and Ashok D. Belegundu. Introduction to Finite Element Engineering (3rd Ed.). Prentice Hall. Upper Saddle River, New Jersey, 2002.
12. Crolla, D.A., R.H. Pitcher, and J.A. Lines, "Active suspension control for an off-road vehicle," Proceedings of the Inst. of Mechanical Eng, Part D, Transport Engineering, 1987, Vol 201, No. D1, Ed. Dr. T.P. Newcomb, Mechanical Engineering Publications Ltd, London, pp1-9.
13. Dixit, R., "Sliding Mode Control and Observation for Semiactive Vehicle Suspensions," MS Thesis, NC State University, 2001.
14. Dreyer, A., J. Graber, M. Hoffman, P Rieth, S Schmitt. "Structure and function of the Brake and Suspension Control System, BSCS." Technical Papers: Total Vehicle Dynamics Vol. 2. XXIV FISITA Congress. Mechanical Engineering Publications Limited for the Institution of Mechanical Engineers. London, 1992. pp7-17.
15. Genta, Giancarlo. Motor Vehicle Dynamics: Modeling and Simulation. World Scientific. Singapore, 1997.
16. Gillespie, T.D., Fundamentals of Vehicle Dynamics, Society of Automotive Engineers, Warrendale, PA, 1992.
17. Goran, M. B., B. I. Bachrach, and R. E. Smith. "The design and development of a broad bandwidth active suspension concept car." Technical Papers: Total Vehicle Dynamics Vol. 2. XXIV FISITA Congress. Mechanical Engineering Publications Limited for the Institution of Mechanical Engineers. London, 1992. pp231-252
18. Hall, B. B., and K.F. Gill, "Performance evaluation of motor vehicle active suspension systems," Proceedings of the Inst. of Mechanical Eng, Part D, Transport Engineering,

1987, Vol 201, No. D2, Ed. Dr. T.P. Newcomb, Mechanical Engineering Publications Ltd, London, pp135-148.
19. Hedrick, J. K. and T. Butsen, "Invariant properties of automotive suspensions," in Advanced Suspensions, Proc. of the Institution of Mechanical Engineers, pp. 35-42, Mechanical Engineering Publications Limited, London, 1988.
20. Hennecke, D. and F.J. Zieglmeier, "Frequency dependent variable suspension damping – theoretical background and practical success," in Advanced Suspensions, Proc. of Institution of Mechanical Engineers, pp. 101-111, Mechanical Engineering Publications Limited, London, 1988.
21. Hillebrecht, P., D. Konik, D. Peril, H. Wallentowitz, F. Zieglmeier. "The active suspension between customer benefit and technological competition." Technical Papers: Total Vehicle Dynamics Vol. 2. XXIV FISITA Congress. Mechanical Engineering Publications Limited for the Institution of Mechanical Engineers. London, 1992. pp221-230
22. Hrovat, D., "Applications of Optimal Control to Advanced Automotive Suspension Design," Journal of Dynamic Systems, Measurement, and Control, Transactions of the ASME, Vol 115, Num 2(B), Tech. Ed. M. Tomizuka, ASME, NY, June 1993.
23. Hyun, C.S., S.H. Keum, and J.K. Hedrick, "Semi-Active Control of the Macpherson Suspension System: Hardware-in-the-Loop Simulations," Proc. of Intl Conf on Control Applications, pp.982-987, 2000.
24. Ikeda, K. "Semi-Active Suspension for a Quarter Car Model Using Fuzzy Logic." MS Thesis, NC State University, 2001.
25. Jolly, M. R., Jonathan W. Bender, and J. David Carlson, "Properties and Applications of Commercial Magnetorheological Fluids," SPIE 5th Annual Int Symposium on Smart Structures and Materials, San Diego, CA, March 15, 1998.
26. Karnopp, D.C. and A.K. Trikha, "Comparative Study of Optimization Techniques for Shock and Vibration Isolation," Journal of Engineering for Industry, Series B, vol91 no4, Transactions of the ASME, pp1128-1132, Nov.1969
27. Karnopp, D.C. , M.J. Crosby, and R.A. Harwood, "Vibration Control Using Semi-Active Force Generators," Journal of Engineering for Industry, Transactions of the ASME, Vol 96, Series B, Number 2, Editor J.J. Jaklitsch, Jr., May 1974, NY, pp618-626.
28. Kazuoka, K. "Development of high performance shock absorbers." Technical Papers: Total Vehicle Dynamics Vol. 2. XXIV FISITA Congress. Mechanical Engineering Publications Limited for the Institution of Mechanical Engineers. London, 1992. pp117-120.
29. Koch, C. DE. "Development of a new continuously variable damper for semi-active suspensions." Technical Papers: Total Vehicle Dynamics Vol. 2. XXIV FISITA Congress. Mechanical Engineering Publications Limited for the Institution of Mechanical Engineers. London, 1992. pp141-151
30. Lee, R.A. and F. Pradko. "Analytical Analysis of Human Vibration." SAE Technical Paper Series. Publication 680091. 1968.
31. Lizell, M., "Semi-active damping," in Advanced Suspensions, Proc. of Institution of Mechanical Engineers, pp. 83-91, Mechanical Engineering Publications Limited, London, 1988.
32. Lord Materials Division, "Magnetic Circuit Design," Engineering Note, November, 1999.
33. Lord Materials Division, "Designing with MR Fluids," Engineering Note, December, 1999.
34. Lord Materials Division, "MR Valve Configurations," Engineering Note, June, 2001.
35. "Lord Product Bulletin: MRF Damping Properties." www.rheonetic.com/pdf/MRF_132AD_2002_15_0.pdf
36. Lord Materials Division, "Permanent - Electromagnet System," Engineering Note, March 2002.

37. Lord Materials Division, "What is the Difference between MR and ER Fluid?" Presentation, May 2002.
38. Miller, L.R., "Tuning Passive, Semi-Active, and Fully Active Suspension Systems," in Proc. of the 27th Conference on Decision and Control, IEEE, pp.2047-2053, 1988.
39. Nicolas, C.F., J.Landaluze, E. Castrillo, M. Gaston, and R. Reyero, "Application of Fuzzy Logic Control to the Design of Semi-Active Suspension Systems," Proc. to the Sixth IEEE Intl. Conf. on Fuzzy Systems, Vol. 3, pp. 987-993, IEEE, 1997.
40. Nguyen, H. T. and M. Sugeno, Ed. Fuzzy Systems: Modeling and Control. Kluwer Academic Publishers. Boston, 1998.
41. Park, W.H., J.C. Wambold, and R.G. Vashlishan, "Prediction of Objective Passenger Comfort From Road Profile," Journal of Engineering for Industry, Transactions of the ASME, Vol 96, Series B, Number 2, Editor J.J. Jaklitsch, Jr., May 1974, NY, pp503-508.
42. Parker, G.A., "A novel valve for semi-active vehicle suspension systems," in Advanced Suspensions, Proc. of Institution of Mechanical Engineers, pp. 69-74, Mechanical Engineering Publications Limited, London, 1988.
43. Passaquay, D., M. Bross, R. Babuska, S. Boverie, and A. Titli, "Performance Evaluation of a Fuzzy Rule Base for Control Purpose," Proc. of the Ninth IEEE Intl Conf on Fuzzy Systems, Vol. 1, pp.423-428, IEEE, 2000.
44. Rashid, M.M., M.A. Hussain, and N. Abd. Rahim, "Semi-Active Car Suspension Controller Design Using Fuzzy Logic Technique," 2002 Student Conference on Research and Development Proceedings, pp.149-152, IEEE, 2002.
45. Roukieh S. and A. Titli. "On the model-based design of semi-active and active suspension for private cars." Technical Papers: Total Vehicle Dynamics Vol. 2. XXIV FISITA Congress. Mechanical Engineering Publications Limited for the Institution of Mechanical Engineers. London, 1992. pp305-318.
46. Ryba, D., "Semi-Active Damping with an Electromagnetic Force Generator," International Journal of Vehicle Mechanics and Mobility, Vehicle System Dynamics, No 1, Vol 22, Ed. P. Lugner and JK Hedrick, Swets and Zeitlinger BV – Lisse, the Netherlands, 1993, pp79-95.
47. Sadiku, Matthew N. O. Elements of Electromagnetics (3rd Ed.) Oxford University Press. New York, 2001
48. Sharp, R.S. and Hassan, "Performance and design considerations for dissipative semi-active suspension systems for automobiles," Proceedings of the Inst. of Mechanical Eng, Part D, Transport Engineering, 1987, Vol 201, No. D2, Ed. Dr. T.P. Newcomb, Mechanical Engineering Publications Ltd, London, pp149-153.
49. Venhovens, P.J.TH., A.C.M. Van Der Knaap, and H.B. Pacejka, "Semi-Active Attitude and Vibration Control," International Journal of Vehicle Mechanics and Mobility, Vehicle System Dynamics, No 1, Vol 22, Ed. P. Lugner and JK Hedrick, Swets and Zeitlinger BV – Lisse, the Netherlands, 1993, pp359-381.
50. Wong, J.Y. Theory of Ground Vehicles. Second Edition. John Wiley & Sons. New York, 1993.
51. Yamaguchi, H., S.-I. Doi, N. Iwama, and Y. Hayashi, "Experimental Study of System Optimization for Suppression of Vehicle Vibration," International Journal of Vehicle Mechanics and Mobility, Vehicle System Dynamics, No 1, Vol 22, Ed. P. Lugner and JK Hedrick, Swets and Zeitlinger BV – Lisse, the Netherlands, 1993, pp299-308.
52. Yeh, E.C. and Y. J. Tsao. "Fuzzy Control for Active Suspension Design." Fuzzy Logic Technology and Applications. IEEE Technology Update Series. Ed. R. J. Marks, II. IEEE. Newyork, 1994. pp109-114.
53. Zhang Yiming and Zeng Zhihua. "Microprocessor adaptive control for vehicle semi-active suspension damping." Technical Papers: Total Vehicle Dynamics Vol. 2. XXIV FISITA Congress. Mechanical Engineering Publications Limited for the Institution of Mechanical Engineers. London, 1992. pp.299-304

9. Appendices

9.1. FEA Model Validation

When FEA models are used as part of the design process, it is important that these models be validated using analytical and/or experimental methods. FEA results for the original MagneShock™ MR damper, obtained using Ansoft Maxwell 3D, were closely scrutinized to correlate experimental and simulated results, and also to understand the relevance of manufacturing and testing variables. By carefully incorporating the critical dimensions, machining tolerances, and testing practices, FEA results were found to correlate very well with experimental data, with flux density errors no larger than 9%.

9.1.1. Simulated and Experimental Testing Procedures

In normal operation, the piston assembly of the MagneShock™ is immersed completely in MR fluid. MR fluid has a fairly high magnetic permeability (up to seven times higher than air) and thus allows for higher flux densities in the shock's annular gap. Ideally, these flux densities could be measured using a Gaussmeter probe within the annular gap. However, experimental test procedures must be performed in open-air environments. For this reason, FEA validation was performed by simulating an air-immersed piston, rather than the environment seen in normal operation (MR-immersed piston).

9.1.2. Initial Model Results:

The initial (unrefined) FEA model exhibited error (between simulated and experimental annular gap flux density) of 20% or more. This high discrepancy was attributed to several reasons:

1. Inconsistent experimental Gaussmeter probe placement
2. Variation of annular gap geometries due to assembly procedures
3. Added reluctance due to surface finish between mated components

Once known, the impact of each of these issues was addressed, resulting in more consistent and accurate results.

9.1.3. Model Improvements:

9.1.3.1. Testing procedures:

To obtain accurate flux density results, experimental and simulation data gathering was standardized. Most notably, the flux density in a particular region within the annular gap was consistently measured experimentally, as was the case with the simulation. Previously, the magnetic flux density was measured experimentally at no particular area within the annular gap, leading to values that could vary widely (due to the flat geometry needed for manufacturing purposes).

9.1.3.2. Piston Assembly Geometry Variations

Experimental test data showed that when the annular gap was eccentric (0.020" +/- 0.003"), little performance difference was measured (5%) in the damping characteristics as compared with a concentric model. This type of variation in an air environment would make a substantial difference in the flux density of the annular gap, but the lack of damping performance change seemed to suggest that the complete MR model was not greatly affected.

To confirm this, a simulation with MR Fluid as the medium around the piston and in annular gap was used to serve as a baseline performance model (control model). The result of this simulation was then compared with a model characterized by offsetting the piston nut by 0.003", narrowing the gap at one side of the piston and increasing it at the other side. All other variables remained constant.

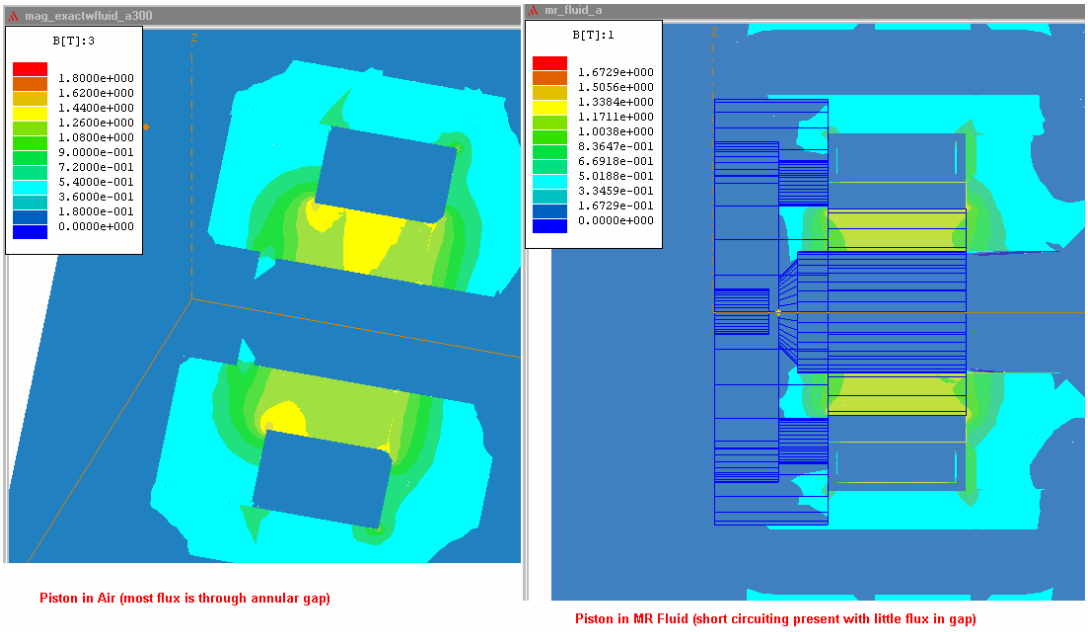

Figure 71. Comparing the Magnetic Circuits of Air and MR Models

As expected, the addition of the MR fluid greatly reduced circuit reluctance as compared with an air-immersed model. In the annular gap, a flux density of approximately 0.5 Tesla was seen for the control group simulation (no eccentricity). However, the flux density in the gap for the eccentric model actually varied very little (Table 24).

Table 24. Simulation results: annular gap flux density

Model Description	Flux Density (Tesla)
Control Model	0.54
Non-Concentric Model: Largest Annular Gap	0.5
Non-Concentric Model: Smallest Annular Gap	0.6
Non-Concentric Model: Side Annular Gap	0.5

These results verify that even a significant difference in the annular gap geometry only minimally affects the flux density of the MR fluid in the annular gap. These results agree with dynamic shock testing of these components, due to there small performance variation. However, due to the low permeability of air, open-air experimental flux density testing must be performed with concentric components and at consistent locations corresponding with simulations.

9.1.3.3. Circuit Reluctance Due To Surface Finish

The introduction of a very small gap between the piston nut and piston (simulating a reluctance at that interface created by an uneven surface finish) caused the simulated flux density to fall within 5% of the experimental flux density. This modification was made after measuring the surface finish with a Talysurf stylus profilometer and finding a high spot of 0.0015" on the turned surface. An uneven surface finish prevents good contact between these parts and increases the reluctance of the magnetic circuit. However, even though this change brought the model results closer to experimental, this finding is significant because it shows the variation of results possible with only small model changes (i.e.: small manufacturing changes).

The surface finish of the piston made the greatest impact on the simulation results with air as the fluid in the "reluctance gap." However, this phenomenon seems to have little effect on the completed piston assemblies (as experimental damping performance range falls within a region of +/- 2%). This inconsistency for assembled shocks using the MR fluid may be attributed to the highly permeable characteristics of the fluid, which in turn leads to little difference of the effective viscosity.

Since the importance of the surface finish or piston nut/piston interface has become apparent, alternative methods of assembly became a focus of study. A press fit method would most likely decrease the reluctance of the circuit, or the introduction of a highly permeable interface assembly lube or epoxy.

Table 25. Magnetic field density in annular gap

		Piston and Nut Interface Reluctance: Interface Gap Distance					
		No Gap		*0.0015"*		*0.002"*	
mA	*Experimental*	*B (Tesla)*	*% Difference From Experimental*	*B (Tesla)*	*% Difference*	*B (Tesla)*	*% Difference*
100	***0.0840***	0.123	46.43	0.096	14.29	***0.08***	***4.76***
300	***0.2283***	0.300	31.41	0.270	18.27	***0.2475***	***8.41***

The most accurate model was found to be the one with a 0.002" gap between the piston and piston nut. This setup provided similar annular gap flux density readings to those found by experimentation within a 9 percent difference.

Following this initial study into the surface finish "reluctance gap," a study of the importance of the material properties of that gap was performed. In the air-immersed models, the air-filled reluctance gap resulted in a significant reduction in the flux density at the annular gap. As seen in Table 2, the MR-immersed models again saw a reduction in the flux density in conjunction with the existence of an air-filled reluctance gap. When filling the reluctance gap with MR fluid, however, essentially no difference was seen from the "no reluctance gap" results (Table 3). This was expected due to the highly permeable nature of the MR fluid compared with air. In practice, this reluctance gap area becomes saturated with fluid, negating its negative effects and thus the results found with a MR fluid-filled reluctance gap could be predicted with a model with ideally mated components (i.e. no reluctance gap).

Table 26. Simulated Annular Gap Flux Density Results (300 mA)

Model	*Flux Density (Tesla)*
Control Model	0.48
Air-Filled Reluctance Gap	0.375
MR Fluid-Filled Reluctance Gap	0.5

Table 27. Effect of reluctance gap on core saturation for MR-immersed piston (300 mA)

Model	*B (Tesla)*	*% of Max (~1.75T)*
Control Model	~1.6	91.43
Air-Filled Reluctance Gap	~1.15	65.71
MR-Filled Reluctance Gap	~1.62	92.57

From the previous results, it is clear that the MR Fluid reluctance gap model closely correlates with that of the control model. For this reason, it was concluded that one of two changes be made to ensure accurate testing and modeling results:

1. Physical open-air flux density testing (with Gaussmeter) should be performed with MR fluid applied to the interface between the piston and piston nut prior to assembly. This would allow for simulations to neglect the reluctance gap for open-air models.

2. Simulation could include the reluctance gap for open-air models. Testing would continue as before. However, the inclusion of an air-filled reluctance gap (rather than an MR-filled gap) resulted in a computer operation time increase from 22 minutes to over 4 hours.

9.1.4. Results of FEA

In conclusion, simulation and experimental analyses were performed and compared to quantify the validity of simulation results. With the consideration of variables (such as machining and manufacturing tolerances) and proper testing techniques (outlined above), simulation results correlated well with experimental finding; percent error did not exceed 9%. In conjunction with model validation and tradition model analysis techniques, FEA is a useful tool for the study and development of electromechanical systems.

9.2. Simulink Model: Comparison of Quarter Car Systems

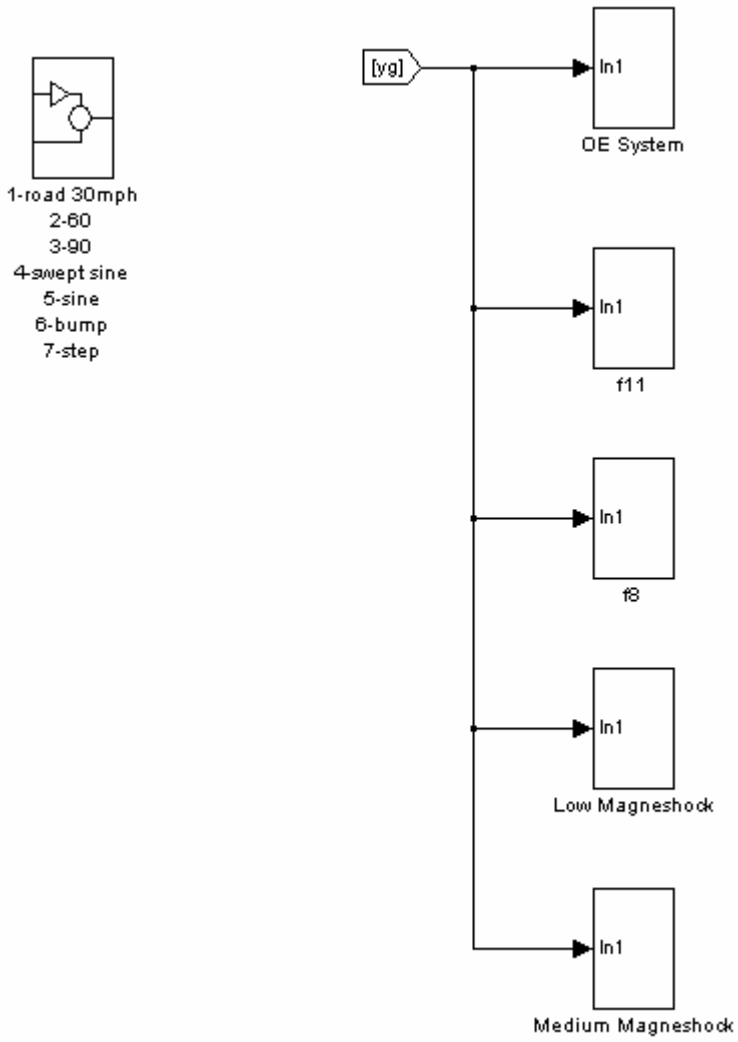

9.3. Simulink Model: Model Setup

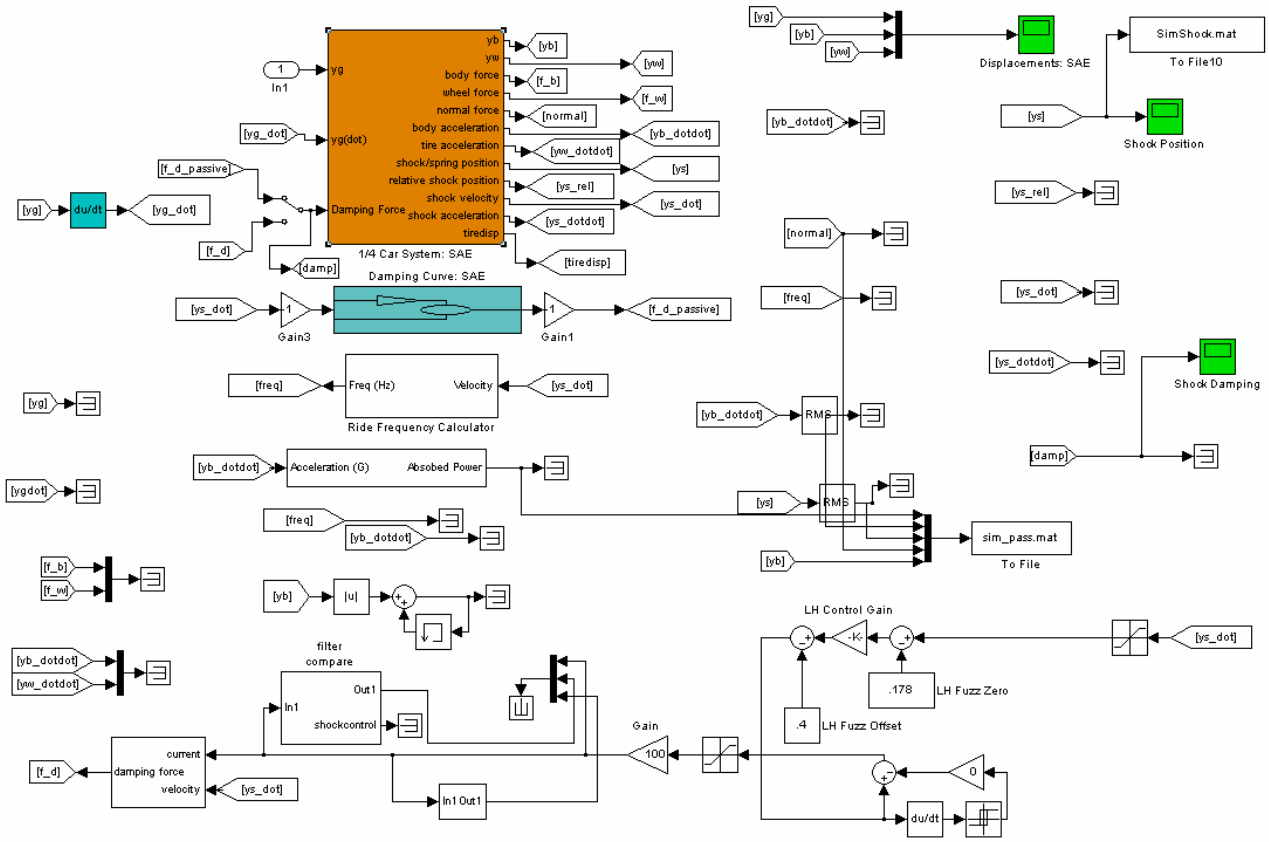

9.4. Simulink Model: Quarter Car Model

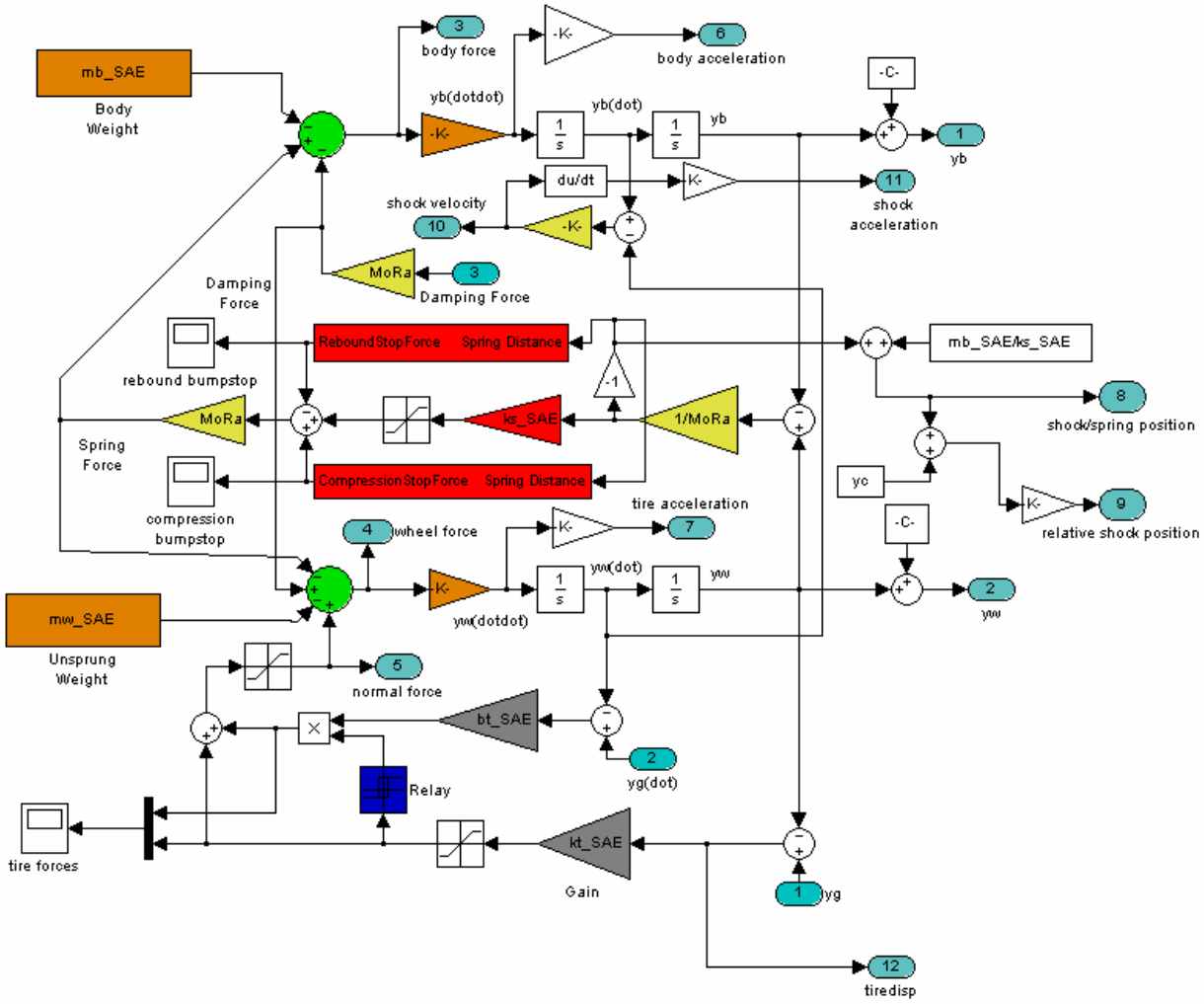

9.5. Damping Force Query Box

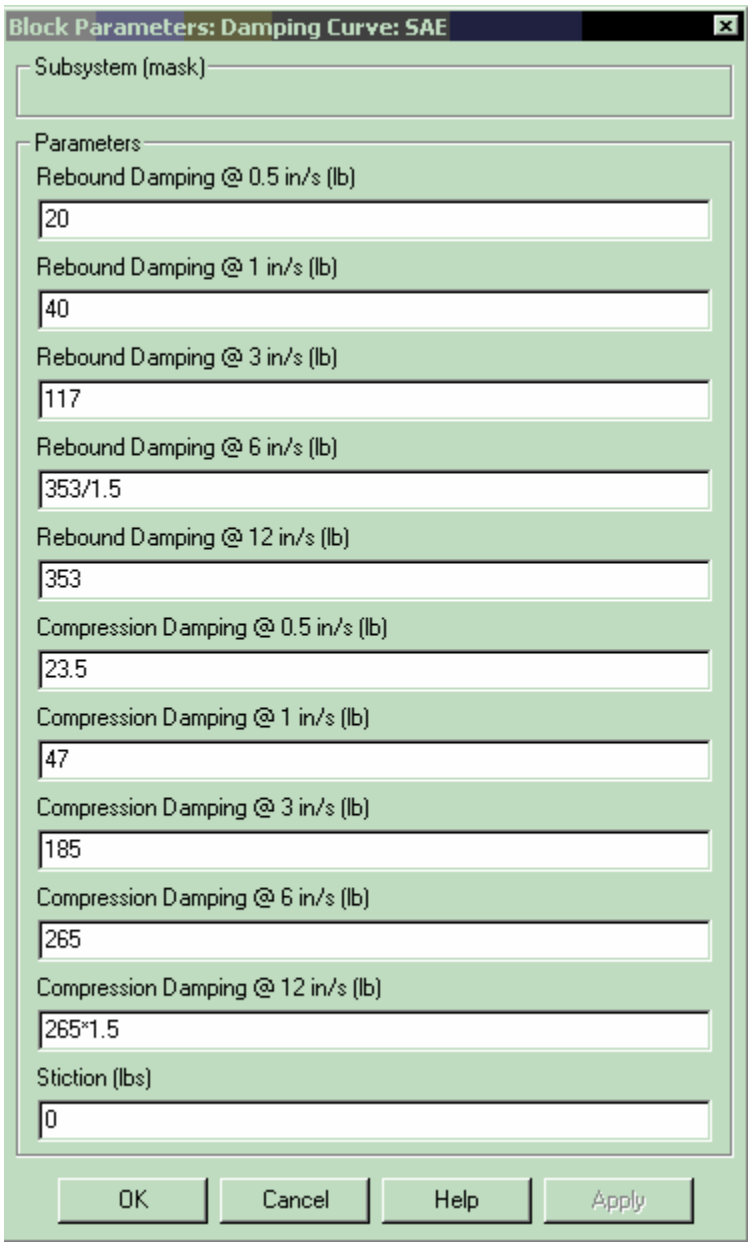

9.6. Simulation Results Comparison Matlab File

```
tendsim=5/.003 %Int(input('Specify ending time: ')/0.003);

load sim_pass

t=pass(1,1:tendsim)
d1=pass(2,1:tendsim)
d2=pass(3,1:tendsim)
d3=pass(4,1:tendsim)
d4=pass(5,1:tendsim)
d5=pass(6,1:tendsim)
%d6=pass(7,1:tendsim)
%d7=pass(8,1:tendsim)
%d8=pass(9,1:tendsim)

avgaccel=mean(d2)
avgtravel=mean(d3)
avgforce=mean(d4)

load sim_pass2

t=pass2(1,1:tendsim)
d12=pass2(2,1:tendsim)
d22=pass2(3,1:tendsim)
d32=pass2(4,1:tendsim)
d42=pass2(5,1:tendsim)
d52=pass2(6,1:tendsim)
%d6=pass(7,1:tendsim)
%d7=pass(8,1:tendsim)
%d8=pass(9,1:tendsim)

avgaccel2=mean(d22)
avgtravel2=mean(d32)
avgforce2=mean(d42)

load sim_pass2b

t=pass2b(1,1:tendsim)
d12b=pass2b(2,1:tendsim)
d22b=pass2b(3,1:tendsim)
d32b=pass2b(4,1:tendsim)
d42b=pass2b(5,1:tendsim)
d52b=pass2b(6,1:tendsim)
%d6=pass(7,1:tendsim)
%d7=pass(8,1:tendsim)
%d8=pass(9,1:tendsim)

avgaccel2b=mean(d22b)
avgtravel2b=mean(d32b)
avgforce2b=mean(d42b)
```

```
%avgpasspass=(d1+d2)/2
%avgpasspass2=(d3+d4)/2
%avgactpass=(d5+d6)/2
%avgactpass2=(d7+d8)/2
%plot(t,d1,'red',t,d2,'red',t,d3,'green',t,d4,'green',t,d5,'blue',t,d6,'blue',t,d7,'c',t,d8,'c',t,avgpasspa
ss,'r--', t, avgactpass,'b--',t, avgpasspass2,'g--', t, avgactpass2,'c--')
%title('Absorbed Energy | Left Hand Body | Capital Boulevard N')
%ylabel('Absorbed Energy (J)')
%xlabel('time (s)')
%GRID ON

load sim_f8
tfzy=f8(1,1:tendsim)
d1fzy=f8(2,1:tendsim)
d2fzy=f8(3,1:tendsim)
d3fzy=f8(4,1:tendsim)
d4fzy=f8(5,1:tendsim)
d5fzy=f8(6,1:tendsim)

avgaccelfzy=mean(d2fzy)
avgtravelfzy=mean(d3fzy)
avgforcefzy=mean(d4fzy)

load sim_f11
tfzy2=f11(1,1:tendsim)
d1fzy2=f11(2,1:tendsim)
d2fzy2=f11(3,1:tendsim)
d3fzy2=f11(4,1:tendsim)
d4fzy2=f11(5,1:tendsim)
d5fzy2=f11(6,1:tendsim)

avgaccelfzy2=mean(d2fzy2)
avgtravelfzy2=mean(d3fzy2)
avgforcefzy2=mean(d4fzy2)

figure(1)
plot(t,d1,'k-.',t,d12,'b--',t,d12b,'b',t,d1fzy,'g--',t,d1fzy2,'g')
title('Absorbed Power | 1/4 Car Simulation ')
ylabel('Absorbed Power (W)')
xlabel('Time (s)')
GRID ON
%HOLD

figure(2)
plot(t,d5,'k-.',t,d52,'b--',t,d52b,'b',t,d5fzy,'g--',t,d5fzy2,'g')
title('Absolute Body Displacement | 1/4 Car Simulation ')
ylabel('Body Displacement (in)')
xlabel('Time (s)')
GRID ON
%HOLD
avgaccel,avgaccel2,avgaccel2b,avgaccelfzy,avgaccelfzy2
avgtravel,avgtravel2,avgtravel2b,avgtravelfzy,avgtravelfzy2
avgforce,avgforce2,avgforce2b,avgforcefzy,avgforcefzy2
```